NASA Contractor Report 3582

Coupled Rotor/Airframe Vibration Analysis

Robert Sopher, R. E. Studwell,
S. Cassarino, and S. B. R. Kottapalli

CONTRACT NAS1-16058
NOVEMBER 1982

NASA

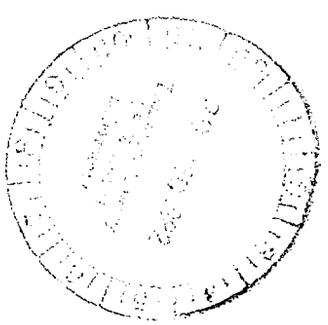

NASA Contractor Report 3582

Coupled Rotor/Airframe Vibration Analysis

Robert Sopher, R. E. Studwell,
S. Cassarino, and S. B. R. Kottapalli
United Technologies Corporation
Stratford, Connecticut

Prepared for Structures Laboratory
AVRADCOM Research and Technology Laboratories
and NASA Langley Research Center
under Contract NAS1-16058

National Aeronautics
and Space Administration

**Scientific and Technical
Information Branch**

1982

FOREWORD

This report describes work performed by the Sikorsky Division of the United Technologies Corporation under Contract NAS1-16058 for the Structures Laboratory of the U.S. Army Research and Technology Laboratories (AVRADCOM).

The Technical Monitor was Mr. R.L. Tomaine.

TABLE OF CONTENTS

LIST OF ILLUSTRATIONS

LIST OF ILLUSTRATIONS (CONTINUED)

LIST OF ILLUSTRATIONS (CONTINUED)

LIST OF ILLUSTRATIONS (CONTINUED)

LIST OF TABLES

SUMMARY

This report describes a Coupled Rotor/Airframe Vibration Analysis which was developed as a design tool for predicting helicopter vibrations, and a research tool to quantify the effects of structural properties, aerodynamic interactions and vibration reduction devices on vehicle vibration levels. The analysis consists of a Base Program utilizing an impedance matching technique to represent the coupled rotor/airframe dynamics of the system supported by inputs from several External Programs supplying sophisticated rotor and airframe aerodynamic and structural dynamic representation. The Base Program has a stand-alone capability to provide assessment of the effects of changes in airframe dynamics and vibration reduction devices on vehicle vibration levels. The Base Program is not restricted in input support from any particular programs and can be executed interactively for many pertinent applications. The theoretical background, computer program capabilities and limited correlation results are presented in this report. Correlation results using scale model wind tunnel results show that the analysis can adequately predict trends of vibration variations with airspeed and higher harmonic control effects. Predictions of absolute values of vibration levels were found to be very sensitive to modal characteristics and results were not representative of measured values.

INTRODUCTION

The reduction of helicopter vibrations has become increasingly important in recent years. Motivations are improvements in reliability and maintainability, passenger and crew comfort, visual acuity and increased equipment protection. The need to reduce vibration levels has influenced the improvement of vibration analysis methodology. In order to provide an analysis capable of accurate vibration prediction, the physical, mathematical and software attributes listed in Table 1 must be included. A review of the literature (see References 1 to 3) showed that published analyses do not possess a complete set of these desired attributes.

From a physical standpoint, the adequate representation of the vibration model requires an adequate simulation of the sources of vibration, an elastic fuselage, and the elements used to control the vibration. Sources of vibration are the air forces acting on the rotor, fuselage, and fixed surfaces of the helicopter. Vibration control methods include reduction of vibratory loads at the sources, modification of response dynamics, and isolation of vibration. Limitations occur in one or more of these categories and a complete physical model does not appear to be available with the scope desired for design studies.

Regarding the mathematical methodology, the majority of methods are limited in their flexibility to represent configurations and in their expandability to new configurations since they are based on hand-derived equations for the coupled dynamical system, in contrast to automated coupling.

From a software standpoint, there are deficiencies in organization, and internal documentation. Comprehensive modeling capability and efficiency require good software to facilitate the

TABLE 1 - ATTRIBUTES OF TARGET VIBRATION ANALYSIS

* Physical
  - Comprehensive rotor model
  - Articulated, hingeless, teetering
  - Fixed system
    - Modal
    - Stick
    - Hybrid
    - Drive Train
    - Test Data
  - Vibration Control Devices
    - Absorbers (hub, blade, airframe)
    - Isolators
  - Higher harmonic control
  - Other vibration sources
    - Tail rotor
    - Empennage
  - Aerodynamic
    - Rotor induced flow field
    - Stall
  - Flight modes
    - Hover, forward flight, transition

* Mathematical
  - General Configuration modeling ability
  - Steady state forced response, eigensolution, time history
  - Parameter variation

* Software
  - Efficiency
  - User-oriented features - input, plotting
  - Clear Architecture
  - Code clarity

addition of new components, and the latitude to exercise and improve solution modes and algorithms. The majority of programs reviewed were designed before it was recognized that the accomplishment of good software is important for flexibility and ease of growth.

In order to provide the desired attributes a substructure assembly method was utilized to simultaneously provide an efficient computer code while retaining the required high level of aerodynamic and dynamical representations. The substructure assembly method incorporates a stand-alone Base Program representing the coupled rotor/airframe system supported by External Programs which provide the necessary aerodynamic sophistication.

This report describes the basis of the coupled rotor/airframe analysis, the capabilities and limitations of the analysis, and theoretical and practical applications.

LIST OF SYMBOLS

A	Matrix in complex eigensolution equation (see equation (36)), 2N x 2N
	Inverse of system impedance matrix (see equation (86)), 2N x 2N
B	Matrix in complex eigensolution equation (see equation (37)), 2N x 2N
	Matrix in Newmark-Beta method (see equation (53)), N x N
c	Cosine
C	Independent coordinate system damping matrix, N x N
C_D	Dependent coordinate system damping matrix, N_D x N_D
$[c]^{(i)}$	Damping matrix for i-th substructure
D	Matrix in Newmark-Beta method (see equation (48)), N x N
[E]	Rotation matrix of direction cosines (see Figure 4), 3 x 3
$\{f\}^{(i)}$	Vector of external forces for i-th sub-structure, representing forces and moments.

f_{x1} f_{y1} f_{z1}	Components of force applied to a substructure connection node in x_1, y_1, and z_1 directions, respectively (see figure (2)), N (lb).
F	Independent coordinate system force vector, N x 1
F'	Matrix in Newmark-Beta method (see equation (54)), N x N
F_D	Dependent coordinate system force vector, N_D x 1
F_n	Independent coordinate system force vector at time t_n in Newmark-Beta method, N x 1
g	Acceleration of gravity, m/s^2 (ft/s^2)
h	Time interval in Newmark-Beta method (see equation (43)), s
h_H	Matrix relating rotor hub reaction forces to HHC control perturbations (see equation (80)), 12 x 6
$h_{11H'}$ $h_{12H'}$ $h_{21H'}$ h_{22H}	Submatrices of matrix H (see equation (81)), N x 3
H	Independent coordinate system matrix introducing effects of HHC control perturbations on system vibrations (see equations (84) and (87)), 2N x 6
H_{11}, H_{12}, H_{21}, H_{22}	Submatrices of matrix H (see equation (89)), N x 3

H_{11D}, H_{12D}, H_{21D}, H_{22D}	Dependent coordinate system submatrices introducing effects of HHC control perturbations on dependent coordinate system reaction loads (see equations (82) and (83)), N_D x 3
I	Identity matrix
J	Performance index for vibration minimization (see equation (90))
K	Independent coordinate system stiffness matrix, N x N
K_D	Dependent coordinate system stiffness matrix, N_D x N_D
$[k]^{(i)}$	Stiffness matrix for i-th substructure
M	Independent coordinate system mass matrix, N x N
	Number of normal modes in a substructure modal representation
M_D	Dependent coordinate system mass matrix, N_D x N_D
m_{x1}, m_{y1}, m_{z1}	Components of moment applied to a substructure connection node in x_1, y_1, and z_1 directions respectively, N-m (lb-ft)
$[m]^{(i)}$	Mass matrix for the i-the substructure
n	integer step numbers in time-history solution (see equation (43))

	Index denoting n-th bifilar mass
N	Total number of independent coordinates in the assembled system
	Number of bifilar arms
	Number or rotor blades
N_D	Total number of coordinates in the dependent coordinate vector (obtained by summing the coordinates for all substructures)
P	Matrix in Newmark-Beta method (see equation (49)), N x N
q	Modal coordinate
Q	Matrix in Newmark-Beta method (see equation (50)), N x N
$\{r\}^{(i)}$	Vector of reaction forces for i-th sub-structure, representing force and moment reactions
r_{x1} r_{y1} r_{z1}	Components of reaction force applied to a sub substructure connection node in x_1, y_1, and z_1 directions, respectively (see Figure (2)), N (lb).
r_{mx1} r_{my1} r_{mz1}	Components of reaction moment applied to a substructure connection node in x_1, y_1, and z_1 directions, respectively (see Figure (2)), N-m (lb-ft)

R	Matrix in Newmark-Beta method (see equation (51)), N x N
R_D	Dependent coordinate system reaction load vector, N_D x 1
s	Sine
S_n	Scalar coefficient of n-th harmonic of stress or pushrod load on a rotor blade, N/m^2 (lb/in^2)
$(S_n)_o$	Scalar coefficient of n-th harmonic of stress or push rod load on a rotor blade for no hub motion and no HHC control input (see equation (94)), N/m^2 (lb/in^2)
$[S_{nH}]$	Matrix introducing the effects of hub displacement on n-th harmonic coefficient of blade stress or push rod load (see equation (94)), 1 x 12
$[S_{n\theta}]$	Matrix introducing the effects of HHC perturbations on n-th harmonic coefficient of stress or push rod load (see equation (94))
t_n	time at n-th integration step (see equation (43)), s
T	Transfer matrix relating HHC inputs to vibratory response of the system, (see equations (84) and (87)), 2N x 6
u	x_1 displacement of a connection node (see Figure (2)), m (ft)

U_T, U_P	Components of airflow relative to a point on a rotor blade, parallel and perpendicular to the rotor rotation plane, respectively, m/s (ft/s)
v	y_1 displacement of a connection node (see Figure 2), m (ft)
w	z_1 displacement of a connection node (see Figure 2), m (ft)
w_1	Component of airflow normal to the median surface of the rotor blade excluding the rotor induced flow (see equation (102)), m/s (ft/s)
W_z	Response vector weighting matrix in expression for vibration reduction performance index (see equation (90)), N_D x N_D
W_θ	HHC control angle weighting matrix in scalar performance index expression (see equation (90)), 3 x 3
$\{x\}^{(i)}$	Vector of coordinates for i-th substructure
X	Vector of independent coordinates for the assembled system (=X_I), N x 1
X_c	Coefficient vector of cosine harmonic term in harmonic expansion of X_I vector (see equation (24)), N x 1
X_{co}	Coefficient vector of cosine harmonic term in harmonic expansion of X_I vector for no HHC control input (see equations (85) and (86)), N x 1

X_D	Vector of coordinates for the dependent coordinate system, N_D x 1
$(X_D)_c$	Coefficient vector of cosine harmonic term in harmonic expansion of X_D vector, N_D x 1
$(X_D)_S$	Coefficient vector of sine harmonic term in harmonic expansion of X_D vector, N_D x 1
X_I	Vector of independent coordinates for the system (= X), N x 1
X_{I1}	Vector of independent coordinates for system after transformation β_1 (see equation (14))
X_{I2}	Vector of independent coordinates for the system after transformation β_2 ($=X_I=X$) (see equation (15)), N x 1
$(X_I)_n$	Vector of independent coordinates at n-th time step in time-history solution
X_o	Vector of dependent coordinates resolved to global reference axis, N_D x 1
X_s	Coefficient vector of first sine harmonic term in harmonic expansion of X_I vector (see equation (24)), N x 1
X_{so}	Coefficient vector of sine harmonic term in harmonic expansion of X_I vector for no HHC control input (see equations (84) and (85)), N x 1

Y	Vector of coordinates used to obtain the complex eigensolution system response (see equation (35)), 2N x 1
	Vector of response variables in the expression for the vibration reduction performance index (see equations (90) and (91))
z_H	Impedance matrix relating rotor hub loads to hub displacements (see equation (60)), 12 x 12
z_{11H}, z_{12H}, z_{21H}, z_{22H}	Submatrices of matrix z_H (see equation (61)), 6 x 6
Z_{11D}, Z_{12D}, Z_{21D}, Z_{22D}	Submatrices of the system impedance matrix referred to dependent coordinates (see equation (64)), N_D x N_D
β	Transformation matrix relating dependent coordinates to independent coordinates (see equation (4)), N_D x N
β_c	Coefficient of cosine term in harmonic expansion of bifilar mass flap displacement (see equation (77)), rad
β_n	Flap displacement of n-th bifilar mass (see equation (77)), rad
β_s	Coefficient of sine term in harmonic expansion of bifilar mass flap displacement (see equation (77)), rad

β_o Transformation matrix relating dependent coordinates X_D resolved to substructure local orientation axis to dependent coordinates X_o referred to global orientation axis (see equation (12)), $N_D \times N_D$

Bifilar mass flap collective displacement, rad

β_1 Transformation matrix relating coordinate vector X_o to coordinate vector X_{I1} (see equation (14))

β_2 Transformation relating coordinate vector X_{I1} to coordinate vector X_{I2} (see equation (15))

β^* Newmark-Beta factor

$[\gamma]$ Modal matrix relating displacements at a node to vector of normal mode coordinates (see equation (17)), 6 x M

γ_c Coefficient of cosine term in harmonic expansion of bifilar mass lead displacement (see equation (74)), rad

γ_n Lead displacement of n-th bifilar mass (see equation (74)), rad

γ_s Coefficient of sine term in harmonic expansion of bifilar mass lead displacement (see equation (74)), rad

δ Fixed absorber mass displacement, m (ft)

θ	Rotor blade collective pitch angle (scalar), rad
	Euler angle relating local and global axes (see figure (3))
θ_c	Vector of cosine coefficients of HHC control angles (see equation (78)), 3 x 1
θ_s	Vector of sine coefficients of HHC control angles (see equation (79), 3 x 1
$(\theta_N)_c$	Coefficient of N-th cosine harmonic in blade HHC control angle expansion
$(\theta_N)_s$	Coefficient of N-th sine harmonic in blade HHC control angle expansion
θ_1, θ_2, θ_3	Angular displacements of a connection node (see Figure 2)
θ, ϕ, ψ	Euler angles relating local and global axes (see Figure (3))
ω	Frequency of a normal mode, rad/sec
ω_f	Load excitation frequency, rad/s
Ω	Rotor speed, rad/s

Subscripts

c	Coefficient of cosine term in a harmonic expansion of a variable
n	n-th harmonic of stress or pushrod load
	n-th bifilar mass
	time index
s	coefficient of sine term in a harmonic expansion of a variable
H	hub

Superscripts

i	i-th substructure
I	imaginary part
n	index of last substructure in a set of substructures
R	real part
T	transpose
-1	inverse
.	first derivative with respect to time

$\ddot{}$ second derivative with respect to time

$-$ amplitude

$*$ optimum value of a control angle

OVERVIEW OF THE COUPLED ROTOR/AIRFRAME VIBRATION ANALYSIS

The Coupled Rotor/Airframe Vibration Analysis consists of a Base Program which is used in conjunction with a set of External Programs to achieve a vibration prediction capability for helicopters. A substructure assembly method is used in the Base Program to assemble a dynamical model of the helicopter from physical helicopter components contained in the Base Program and External Program models of the rotor system. The Base Program solution modes include steady state forced responses, eigensolutions, time history solutions, and parameter variation capability. Rotor data are transferred to the Base Program, which functions in a stand-alone mode to facilitate the evaluation of parameter variations on vibrations. Stand-alone operation is achieved with a small core requirement. The Base Program and the External Programs are configured to provide the user with latitude to select applications tailored to user interest, aptitude, and convenience. If rotor data are on file, the use of the External Programs is not required. The Base Program may be used in a stand-alone mode also for cases not requiring rotor data - e.g., investigation of transmission/isolator/fuselage response. Input to the Base Program is designed to provide an economical format requiring input only for selected components. Input to the Base Program is not restricted to the External Programs discussed in this report. Programs with similar capabilities may be utilized provided that input formats are followed.

Base Program

The Base Program calculates the mass, damping, and stiffness matrices, and forcing function vectors of substructures resident in the Base Program code. Input data consist of 3-character literal strings which define the components to be included in the configuration. These 3-character literal strings trigger input

requirements for the components and the forming of the properties of the requested components. Input data also define component element numbers and points of connection with other components. The Base Program uses these data to calculate a transformation matrix which synthesizes the coupled equations of motion for the assembly from the separate equations for the components. The transformation matrix relates the set of coordinates for the components of the requested system to a reduced coordinate set applicable to the coupled equations of motion. Redundant coordinates are removed from the coordinates for the requested components (the dependent set) to create the coordinates for the coupled system (the independent set). Rotation transformations relating component local axes to assembled system global axes are included in the transformation matrix. The user may elect to solve the final equation of motion by one of several methods. Component responses are recovered from the solution by multiplication of the solution vector by the system transformation matrix.

The External Programs yield the dynamic and aerodynamic mass, damping, and stiffness matrices, and forcing functions of the rotor system. These properties are assembled with the properties of the components resident in the Base Program by using the transformation method described above.

Figure 1 illustrates the data transfer between the Base Program and the External Programs. The arrows indicate the directions of the data transfer. Cycling of data between modules is indicated by two separate arrows joining program blocks. The character of the data transferred is shown in Figure 1. The data transfer from the External Programs into the Base Program is accomplished by file transfers and the Base Program operates in a stand-alone mode to obtain solutions.

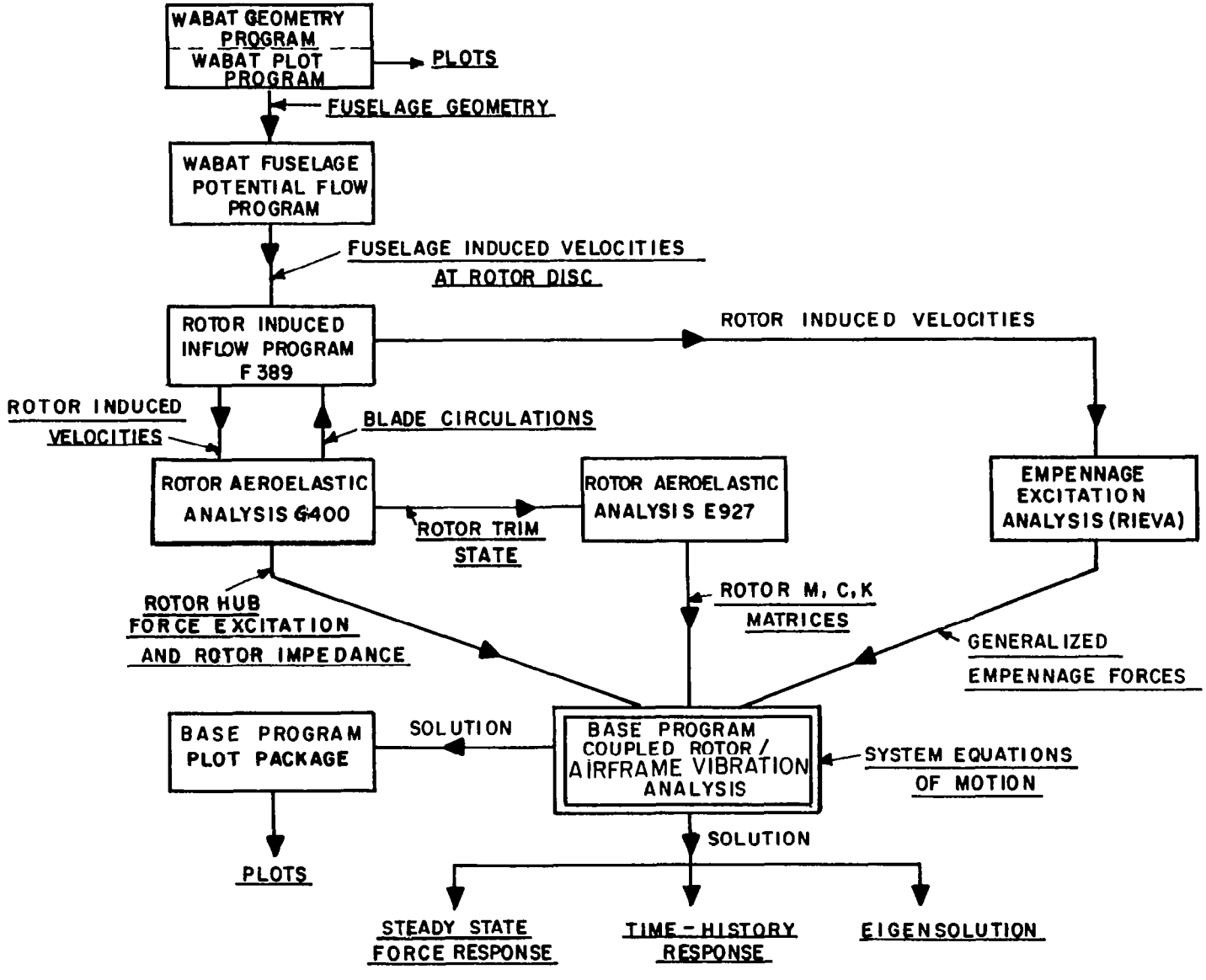

Figure 1. Coupled Rotor/Airframe Vibration Analysis Data Flows.

The Four External Programs chosen to support the Base Program to form the coupled rotor/airframe analysis are described in a subsequent section.

SUBSTRUCTURE ASSEMBLY METHOD

The configuration of the Base Program and the data transfer between the Base Program and the External Programs are based on a substructure approach. The substructure approach synthesizes the equations of motion from dynamical models of parts of the system. The substructure approach is the key to a flexible modeling capability permitting wide latitude in design studies. The approach achieves an accurate representation of rotor/airframe systems in the framework of an efficient computer program.

The substructure method employed is the Hurty method of Reference 4. The coordinates or degrees of freedom of a substructure (also called physical component) are physical and generalized displacements, such as modal amplitudes. The equation of motion for each substructure is expressed in mass, damping, and stiffness matrix, and force vector form. Character and treatment of exceptions to these forms occurring in the Base Program and the External Programs are described subsequently. Properties of the i-th substructure are $[m]^{(i)}$, $[c]^{(i)}$, $[k]^{(i)}$, $\{f\}^{(i)}$, and $\{r\}^{(i)}$. These are respectively mass, damping, and stiffness matrices, and external force and reaction force vectors. The submatrices for the substructures are collected into a partitioned diagonal matrix equation which represents the system. This partitioned diagonal matrix equation is

$$M_D\ddot{X}_D + C_D\dot{X}_D + K_DX_D = F_D - R_D \qquad (1)$$

The matrix M_D illustrates the typical form of the diagonal matrices as:

$$M_D = \begin{bmatrix} [m]^{(1)} & & \\ & [m]^{(2)} & \\ & & \ddots \\ & & & [m]^{(n)} \end{bmatrix} \qquad (2)$$

The vector of coordinates X_D illustrates the form of the vectors F_D and R_D in equation (1).

$$X_D = \begin{Bmatrix} \{x\}^{(1)} \\ \{x\}^{(2)} \\ \vdots \\ \{x\}^{(n)} \end{Bmatrix} \qquad (3)$$

The subscript D signifies that equation (1) applies to a set of coordinates X_D which may contain coordinate elements which are equal to or depend on each other. In other words, X_D is a "dependent" coordinate set, which can contain redundant elements. The coordinate vector X_D contains unconnected coordinates and connection node coordinates. The displacement of the mass of a simple absorber would be an unconnected coordinate. The displacement of the base of the absorber would be a connection node coordinate because the base of the absorber may be attached to another component. When components are connected to each other redundant coordinates occur in X_D.

A force vector, $\{f\}^{(i)}$, represents external forces and moments applied to the i-th substructure. The forces may act at points of the structure which are unconnected, like an absorber mass, or at a connection node, like the absorber base. Reaction forces act on a substructure at points of connection betwen it and other substructures, and are induced by the other substructures. The reaction force vector, $\{r\}^{(i)}$, does not have any elements associated with unconnected coordinates. Figure 2 shows the sense of

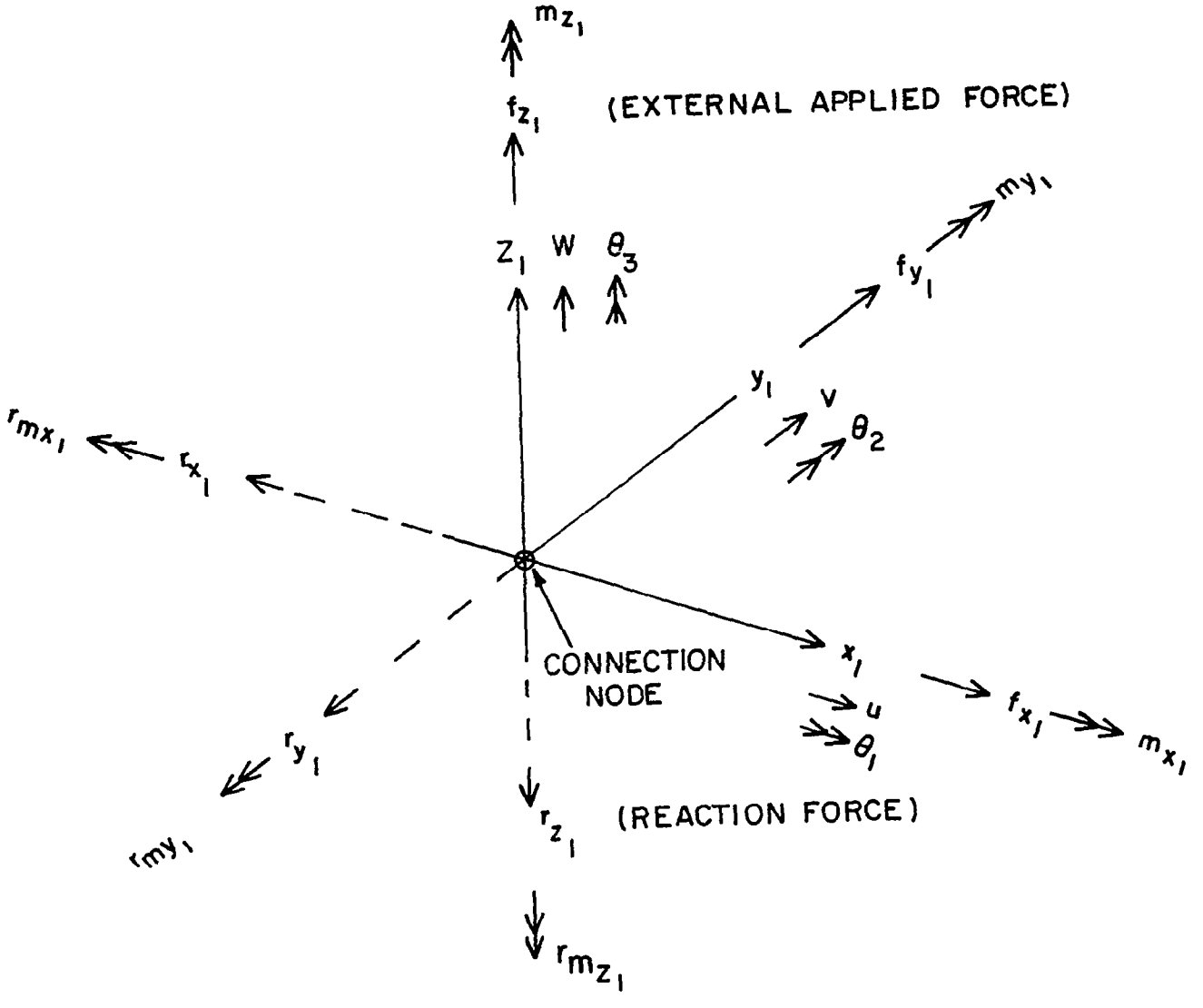

Figure 2. Displacements and Forces Acting on a Connection Node of a Substructure.

forces and moments applied to a connection node. Appendix A illustrates the terminology introduced for a simple system.

The synthesis of the equations of motion for the coupled system is accomplished by a mapping or transformation relating the dependent coordinates, X_D, to a reduced coordinate set, X_I. Redundant coordinates are eliminated by requiring component displacements to be equal at connections. The reduced coordinate set may include modal coordinates. The transformation matrix relating X_D and X_I is denoted by β. The mapping from one coordinate set to the other is:

$$X_D = \beta X_I \tag{4}$$

Appendix A shows a sample set of coordinates, X_D and X_I, and a sample mapping.

Substitution of the transformation equation (4) in equation (1) and pre-multiplication of equation (1) by β^T yields the final equation of motion for the coupled system. This is

$$M\ddot{X}_I + C\dot{X}_I + KX_I = F \tag{5}$$

The matrices and vector in equation (5) are

$$M = \beta^T M_D \beta \tag{6}$$

$$C = \beta^T C_D \beta \tag{7}$$

$$K = \beta^T K_D \beta \tag{8}$$

$$F = \beta^T F_D \tag{9}$$

Matrix β is assumed to be a constant function of time, since its elements relate displacements at interfaces which are rigidly joined, or coordinates which are identical - e.g. internal coordinates. The condition that reaction forces at connection nodes are equal and opposite was used to obtain equation (5). This condition reduces to

$$\beta^T R_D = 0 \tag{10}$$

Equation (10) satisfies the requirement that work done by internal reactions of the assembled structure in a virtual displacement, consistent with the constraints, is zero.

Equations (6) through (9) are used in the Base Program to synthesize the equations of motion for the coupled system. Appendix A illustrates the synthesis of coupled system equations.

The component displacements X_D may be recovered from the solution to equation (5), X_I, by mapping equation (4). Component velocities and accelerations are derived similarly. With X_D and its derivatives known, connection node or interface reactions from equation (1) may be expressed as

$$R_D = F_D - (M_D \ddot{X}_D + C_D \dot{X}_D + K_D X_D) \tag{11}$$

Rotor hub shears and moments are sample interface reactions. Appendix A illustrates the recovery of interface reactions.

Composition of Transformation β

The transformation matrix β is expressed as the product of three transformations which assemble coupled systems from components whose properties are defined in component local axes, and allow for the use of modal coordinates. These transformations are described in the following subsections.

Transformation from Local to Global Axes, β_o

The transformation from dependent coordinates resolved to local axes with arbitrary angular orientations to dependent coordinates resolved to a global reference axis is

$$X_D = \beta_o X_o \tag{12}$$

Dependent coordinate sets X_D and X_o can include coordinates which are redundant. Redundant coordinates occur when components are connected to each other at connection nodes. Equation (12) resolves coordinates at connection nodes to the same system and is a prerequisite to the elimination of redundant coordinates from X_o. Figure 3 illustrates the angular orientation of a local axis system relative to a global system. The local system is obtained by three successive rotation displacements of axes through Euler angles θ, ϕ, and ψ.

The rotation transformation relating linear displacements in the local and global axes is

$$\begin{Bmatrix} u \\ v \\ w \end{Bmatrix}_{\text{Local}} = [E] \begin{Bmatrix} u \\ v \\ w \end{Bmatrix}_{\text{Global}} \tag{13}$$

Matrix [E] is a 3 X 3 matrix of direction cosines each of which is a function of Euler angles θ, ϕ, ψ. The same transformations apply also when small angular displacements θ_1, θ_2, θ_3 are substituted for u, v, w. Linear and angular velocities and accelerations are mapped by equivalents of equation (13). Figure 4 defines the elements of matrix [E]. Appendix A shows the application of a rotation transformation to a simple absorber. The

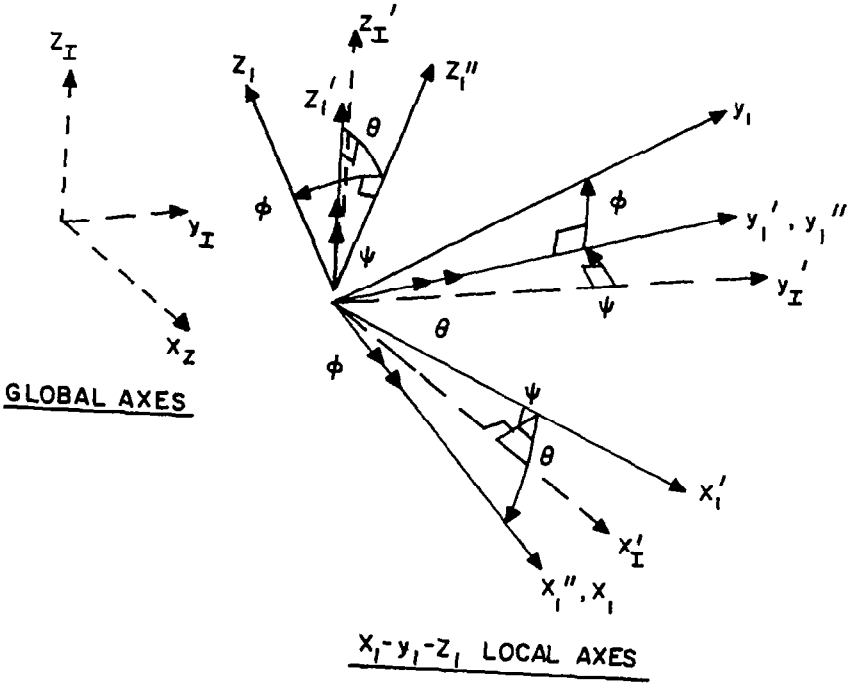

Figure 3. Local and Global Axes.

absorber mass displacement, δ, is an unconnected coordinate and is retained as a coordinate in the final system. It is not necessary to resolve δ to a global system because unconnected coordinates do not have to be eliminated by equating displacements at connections. Unconnected coordinates are assumed to be invariant to rotation transformations from local to global axes.

Transformation from Dependent Coordinates to Physical Domain Independent Coordinates, β_1

The transformation from dependent coordinates referred to a global reference axis to coordinates from which redundant coordinates at connection nodes have been removed is

$$X_o = \beta_1 X_{I1} \tag{14}$$

Coordinate set X_{I1}, is referred to as the physical domain independent coordinate set since connection node displacements are physical displacements. The determination of β_1 is based on a convention in the computer program specifying the order of coordinates in the dependent sets X_o and X_{I1}. Coordinates in X_o are ordered according to ascending component element numbers assigned by the user in the input specification to the Base Program. Appendix A illustrates this organization in X_o. In coordinate set X_{I1}, unconnected coordinates are listed first in order of ascending element number. Connected coordinates are listed after unconnected coordinates in order of ascending connection mode numbers. Redundant coordinates are eliminated by first retaining coordinates for a component with the lowest element number, and then eliminating redundant connected coordinates with higher element numbers from a connection node. Appendix A shows the ordering of coordinates in X_{I1}. The logic yielding the elements of β_1 is based on the ordering of coordinates in X_o and X_{I1}

described above. Appendix A shows the transformation matrix β_1 corresponding to the illustrations given for X_o and X_{I1} .

Transformation from Physical Domain Independent Coordinates to Modal Domain Independent Coordinates, β_2

The transformation from physical domain independent coordinates, X_{I1} , to coordinates which include modal coordinates, X_{I2} , is

$$X_{1I} = \beta_2 \; X_{I2} \tag{15}$$

This transformation is required when modal structures are used. Since X_{I2} is the final coordinate set for the system to be solved it is symbolized also by X_I, i.e.

$$X_I = X_{I2} \tag{16}$$

The coordinate set X_{I2} is obtained from X_{I1} by expressing connection node coordinates in terms of modal coordinates. For example, rotor/airframe hub coordinates may be expressed in terms of airframe modal coordinates. Coordinate set X_{I2} may contain connection coordinates which have not been expressed as modal coordinates, and will in general include unconnected coordinates for the substructures. Coordinate set X_{I2} is referred to as the independent coordinate set in the modal domain.

Connection node displacements are expressed in terms of modal coordinates {q}. The linear and angular displacements at a connection node referred to a local axis for the modal structure are

$$\begin{Bmatrix} u \\ v \\ w \\ \theta_1 \\ \theta_2 \\ \theta_3 \end{Bmatrix}_{\text{Local}} = [\gamma]\ \{q\} \qquad (17)$$

In equation (17),[γ] is a 6XM modal matrix. The vector of normal modes of the substructure has dimensions MX1, i.e., the substructure equations of motion have M normal modes. Small angular displacements are assumed. Velocities and accelerations are mapped by the equivalents of equation (17). The local axis system displacements for the modal structure are related to the global axis displacements for the final system by

$$\begin{Bmatrix} u \\ v \\ w \\ \theta_1 \\ \theta_2 \\ \theta_3 \end{Bmatrix}_{\text{Local}} = \left[\begin{array}{c|c} [E] & O \\ \hline O & [E] \end{array}\right] \begin{Bmatrix} u \\ v \\ w \\ \theta_1 \\ \theta_2 \\ \theta_3 \end{Bmatrix}_{\text{Global}} \qquad (18)$$

In equation (18), [E] is the matrix of direction cosines introduced in equation (13) with elements defined in Figure 4. To obtain the connection node displacements referred to the global system in terms of modal coordinates, the inverse of the rotation transformation [E] is expressed as:

$$[E]^{-1} = [E]^{T} \qquad (19)$$

$$\begin{Bmatrix} u \\ v \\ w \end{Bmatrix} = [E] \begin{Bmatrix} u \\ v \\ w \end{Bmatrix}$$

Local Global

$$[E] = \begin{bmatrix} c_\theta c_\psi & , & c_\theta s_\psi & , & -s_\theta \\ s_\phi s_\theta c_\psi - c_\phi s_\psi & , & s_\phi s_\theta s_\psi + c_\phi c_\psi & , & s_\phi c_\theta \\ c_\phi s_\theta c_\psi + s_\phi s_\psi & , & c_\phi s_\theta s_\psi - s_\phi c_\psi & , & c_\phi c_\theta \end{bmatrix}$$

Figure 4. Elements of Rotation Transformation Matrix [E].

The solution to equations (17) and (18) is

$$\begin{Bmatrix} u \\ v \\ w \\ \theta_1 \\ \theta_2 \\ \theta_3 \end{Bmatrix}_{Global} = \begin{bmatrix} [E]^T & O \\ O & [E]^T \end{bmatrix} [\gamma]\{q\} \qquad (20)$$

Combining equation (20) with equation (15) yields the matrix β_2 relating the coordinates in X_{I1} to modal coordinates and other coordinates in X_{I1}. Equation (20) is used at each connection node where physical displacements are to be expressed in terms of modal displacements. In general, the matrices [E] and [γ] will differ among the nodes because different modal substructures may be joined to different nodes of the system, and because of different component orientations. Appendix A gives examples of X_{I1}, X_{I2} and β_2.

Composite Transformation β Relating Dependent Coordinates to Independent Coordinates

From equations (12), (14), (15), and (16) it is found that

$$X_D = \beta_o \beta_1 \beta_2 X_I \qquad (21)$$

Comparison of equations (4) and (21) yields

$$\beta = \beta_o \beta_1 \beta_2 \qquad (22)$$

This transformation relates the dependent coordinate set, X_D, for the assembly of substructures to the final independent (non-redundant) coordinate set, X_I, used to solve the equations of motion. Equation (22) is used to construct the β-transformation in the computer program. Appendix A gives an example of the composite transformation.

SOLUTION MODES

Four solution modes of equation (5) can be obtained. Each method has different attributes affecting information provided, speed of execution, and computer program core requirements. These solution modes are: 1) steady state forced response, FR1, 2) eigensolution mode for systems without damping, EG1, 3) eigensolution mode for systems with damping, EG2, and 4) time history mode yielding system response as a function of time, TH1.

In addition to the solution modes described above, two more operational modes of the program may be invoked. These modes are 1) parameter variation mode, PV1, designed to provide a convenient selection and variation of parameters in design studies, and 2) general program control mode, GEN, presently configured to control display of program output and graphics options.

Table 2 lists the character names associated with each solution mode and operational mode available.

A description of each solution and operational mode is given below:

TABLE 2 - BASE PROGRAM SOLUTION MODES AND OPERATIONAL MODES

MODE FLAG	DESCRIPTION OF MODE
FR1	FORCED RESPONSE 1 - Forced response solution mode yielding harmonics of steady state response
EG1	EIGENSOLUTION 1 - Eigensolution mode for systems without damping
EG2	EIGENSOLUTION 2 - Eigensolution mode for systems with damping
TH1	TIME HISTORY 1 - Time history solution mode using Newmark-Beta method
PV1	PARAMETER VARIATION 1 - Operational mode facilitating variation of parameters for design studies
GEN	GENERAL - General control mode providing general control for a case

Steady State Forced Response (FR1)

The harmonic steady-state forced response mode FR1, yields harmonic coefficients of response to a steady harmonic excitation. This solution mode is useful for design studies by virtue of execution time, small system core requirements, and importance of steady state vibrations.

The forcing function which appears in equation (5) is assumed to be

$$F = F_c \cos \omega_f t + F_s \sin \omega_f t \qquad (23)$$

In equation (23), ω_f is the forcing frequency and F_c and F_s are N X 1 vectors, where N is the dimension of vectors in equation (5). The harmonic steady state forced response is also assumed periodic.

$$X_I = X_c \cos \omega_f t + X_s \sin \omega_f t \qquad (24)$$

Substitution of equations (23) and (24) into (5) and equating the coefficient expressions of cos $\omega_f t$ and sin $\omega_f t$ to zero yields the 2N X 2N algebraic equation

$$\begin{bmatrix} -\omega_f{}^2M+K & \omega_f C \\ -\omega_f C & -\omega_f{}^2M+K \end{bmatrix} \begin{Bmatrix} X_c \\ X_s \end{Bmatrix} = \begin{Bmatrix} F_c \\ F_s \end{Bmatrix} \qquad (25)$$

The solution to equation (25) is

$$\begin{Bmatrix} X_c \\ X_s \end{Bmatrix} = \begin{bmatrix} -\omega_f{}^2M+K & \omega_f C \\ -\omega_f C & -\omega_f{}^2M+K \end{bmatrix}^{-1} \begin{Bmatrix} F_c \\ F_s \end{Bmatrix} \qquad (26)$$

Determination of vibratory response requires one inversion, equation (26). Solution speed is much higher than a time history solution and the method is well suited to parametric design studies.

Equations (25) and (26) apply to systems expressible in mass, damping, and stiffness form. These matrices may contain aerodynamic contributions such as in the matrices derived from aeroelastic analysis E927. In aeroelastic analysis G400, rotor characteristics, including aerodynamic effects, are represented as a hub force and moment excitation vector and a hub impedance matrix. Rotor induced impedance matrices Z_{ij} must be added to the system matrices in equation (26) to obtain the vibratory res ponse. The steady state solution is

$$\begin{Bmatrix} X_c \\ X_s \end{Bmatrix} = \begin{bmatrix} -\omega_f{}^2M+K+Z_{11} & \omega_f C+Z_{12} \\ -\omega_f C+Z_{21} & -\omega_f^2\, M+K+Z_{22} \end{bmatrix}^{-1} \begin{Bmatrix} F_c \\ F_s \end{Bmatrix} \qquad (27)$$

Forcing function vectors F_c and F_s in equation (27) contain rotor contributions. Impedance matrices in equation (27) apply to the assembled system with independent coordinates, X_c and X_s. Transformations similar to those used to transform mass, damping, and stiffness matrices in equations (6) through (8) yield the impedance matrices in equation (27). The subject of mapping rotor impedance matrices to independent coordinates is treated in a subsequent section.

The system vibratory response can be expressed in units of acceleration of gravity by

$$\ddot{X}_c/g = -(\omega_f{}^2/g)X_c \tag{28}$$

$$\ddot{X}_s/g = -(\omega_f{}^2/g)X_s \tag{29}$$

The computer program displays the amplitude and phase of each coordinate in X_I. This information is extracted from the elements of X_c and X_s. The response of each coordinate is assumed to be a cosine function. The standard line-printer output does not display X_c and X_s. A debug option may be flagged to obtain X_c and X_s. Amplitude and phase data only are stored for plotting.

Eigensolution for Systems Without Damping (EG1)

The eigensolution mode for systems without damping yields the frequencies and mode shapes of structures without damping. Matrices must be constant with respect to time. The effects of changes in physical properties on mode shapes and frequencies can be determined. These effects are used to aid the interpretation of the effects of design variables on normal modes and vibratory response. This solution mode has a potential capability, not implemented in the present version of the base program, to transform substructure mass, damping, stiffness and force vector properties to normal mode coordinates. Normal mode coordinates reduce the problem to one requiring fewer coordinates.

Equation (5) is specialized to

$$M\ddot{X}_I + K\dot{X}_I = 0 \tag{30}$$

The solution is assumed to be periodic

$$X_I = \bar{X}e^{i\omega t} \tag{31}$$

Substitution of equation (31) into (30) yields the NxN algebraic equation

$$(-\omega^2 M + K)\,\bar{X} = 0 \tag{32}$$

Solutions to equation (32) yield the eigenvalues, ω^2, and corresponding eigenvectors, $\bar{X}$.

Eigensolutions for Systems with Damping (EG2)

The eigensolution mode for systems with damping is used to provide information on the stability of coupled systems. This solution mode is restricted to hover. Coupled systems may include rotor representations which embody dynamic and aerodynamic matrices derived from rotor aeroelastic analysis E927. Stability information may be used to supplement the steady state vibratory response data for a system to provide more data on system attributes. Matrices must be constant with respect to time.

Equation (5) is specialized to

$$M\ddot{X}_I + C\dot{X}_I + KX_I = 0 \tag{33}$$

Reduced to the first order system equation (33) becomes

$$\dot{A}Y - BY = O \tag{34}$$

This is accomplished by the substitution

$$Y = \begin{Bmatrix} \dot{X}_I \\ X_I \end{Bmatrix} \tag{35}$$

Matrices in equation (34) are

$$A = \left[\begin{array}{c|c} O & M \\ \hline M & C \end{array}\right] \tag{36}$$

$$B = \left[\begin{array}{c|c} M & O \\ \hline O & -K \end{array}\right] \tag{37}$$

The eigenvalue problem is obtained from equation (34) by assuming

$$Y = \bar{Y} e^{\lambda t} \tag{38}$$

which yields the 2N X 2N algebraic equation

$$(\lambda A - B)\bar{Y} = O \tag{39}$$

The modal frequency in hertz and modal damping in fractions of critical damping respectively are

$$\omega = \lambda_i/(2\pi) \tag{40}$$

$$\zeta = -\lambda_r/(\lambda_i^2 + \lambda_r^2)^{\frac{1}{2}} \tag{41}$$

with

$$\lambda = \lambda_r + i\,\lambda_i \tag{42}$$

representing a complex eigenvalue. The real and imaginary components of Y are displayed for each mode. A stable mode corresponds to a positive value of ζ (negative value of λ_r).

Time History Solution Mode (TH1)

The time history solution mode TH1, yields the response of a system as a function of time. Transient responses, steady responses, and the stability of systems can be determined from the time-history behavior of a system. Responses of nonlinear systems can be determined. The time-history mode is able to, or has the potential to, supply all the information provided by forced response and eigensolution modes, in addition to the analysis of transient and non-linear data. A drawback of the method is its high execution time in comparison with the other methods making it comparatively costly and inefficient for design studies.

The solution algorithm yielding the time history response is the Newmark-Beta method described in Reference 5. The method is a finite difference method. Displacement responses are obtained from displacements known at prior times, and from data defining the magnitudes of known external forces acting on the system.

The vector of coordinates satisfying equation (5) at time step n is denoted $(X_I)_n$. The corresponding time is

$$t_n = t_{n-1} + nh \qquad (43)$$

In equation (43) h is the step size. The integer step number n ranges from one to the number of steps in the calculation. Time t_o is the initial time. Corresponding initial conditions are $(X_I)_o$ and $(\dot{X}_I)_o$.

When $(X_I)_o$ and $(\dot{X}_I)_o$ are specified the displacement response at t_1 is found from

$$(X_I)_1 = D^{-1} \quad [P(X_I)_o + Q(\dot{X}_I)_o + \beta^* h^2 F_1 + RF_o] \tag{44}$$

Matrices D, P, Q and R are functions of M, C, and K in equation (5), time step h, and factor β^* (see equations (48) through (52)). They have dimensions NXN where N is the size of X_I in equation (5). The Factor β^* is the Newmark-Beta Factor. Values of β^* ranging from 0 to 0.25 can be input to the Base Program. The factor β^* is used to control the variation of acceleration assumed in the time interval (see remarks in Reference 5). A numerical solution with $\beta^* = 0.25$ is unconditionally stable. Force vectors F_1 and F_o are known external forcing functions at t_o and t_1.

After the solution $(X_I)_1$ is known, successive solutions are obtained from the recursion formula

$$(X_I)_{n+1} = D^{-1} \quad [\ (X_I)_n - F'(X_I)_{n-1}$$

$$+ \beta^* h^2\ (F_{n+1} + (1/\beta^* - 2)F_n + F_{n-1})] \tag{45}$$

The NxN Matrices B and F' are known functions of M, C, and K, step size h, and factor β^* (see equations (53) and (54)).

Equation (45) may be used also to restart solutions from solutions calculated up to the time of restart.

The additional assumption is made in the Base Program code that the force F_{n+1} linearly extrapolates the forces F_n and F_{n-1}. For equal intervals of time h this assumption reduces to

$$F_{n+1} = 2F_n - F_{n-1} \tag{46}$$

and equation (44) becomes

$$(X_I)_{n+1} = D^{-1} \quad [B(X_I)_n - F'(X_I)_{n-1} + h^2F_n] \tag{47}$$

Equation (46) allows for the inclusion of aerodynamic forces which are functions of X_I, $\dot{X}_I$ and $\ddot{X}_I$. The present version of the Base Program does not model these aerodynamic forces. A technique to include these forces is to assume F to be a function of X_I and its derivatives at a prior time. Equations (46) and (47) are consistent with this assumption.

Matrices in equations (44), (45), and (47) are

$$D = M + (h/2)C + \beta^*h^2K \tag{48}$$

$$P = M + (h/2)C - (1/2-\beta^*)\, h^2K \\ -(1/4-\beta^*)h^3CM^{-1}K \tag{49}$$

$$Q = [M - (1/4 - \beta^*)\, h^2CM^{-1}C]\ h \tag{50}$$

$$R = [(1/2 - \beta^*)I + (1/4 -\beta^*)\, hCM^{-1}\ ]\ h^2 \tag{51}$$

$$I = \text{unit matrix} \tag{52}$$

$$B = 2M - (1-2\beta^*)\, h^2K \tag{53}$$

$$F' = M - (h/2)C + \beta^*h^2K \tag{54}$$

The dimensions of matrices in equations (48) through (54) are NXN where N is the dimension of the vector of independent coordinates X_I.

Parameter Variation Mode (PV1)

The parameter variation mode, PV1, is used to identify and specify a range for a parameter which is to be changed in design studies. This operational mode provides a convenient and general mode of selection of parameters to be varied among the substructures available in the Base Program. Up to ten parameters from any of the substructures may be varied simultaneously.

General Control Mode, GEN

The general control mode, GEN, is designed to provide a basis for the application of general controls to a case such as line printer output and graphics selection.

ASSEMBLY OF ROTOR IMPEDANCE MATRIX

The purpose of this section is to derive the procedure for the assembly of a rotor impedance matrix with mass, damping, and stiffness matrices and forcing functions of other substructures. The mapping of the rotor impedance matrix to independent coordinates for the coupled system is shown to be the same as for other substructure properties. The rotor impedance matrix must be partitioned to accomplish the mapping.

The effects of hub displacement are included in the coupled rotor/airframe system by representing the rotor effects as the sum of a hub excitation for a fixed hub and a correction involving the rotor impedance matrix multiplied by hub displacement. This representation enables rotor properties to be calculated prior to execution of the Base Program. This formulation maintains the desired small core and execution time for the Base Program.

To obtain a rotor hub excitation vector and a rotor hub impedance matrix, the rotor is first analyzed for a fixed hub in the aeroelastic analysis - e.g. G400. The six hub forces and moments acting on the fixed hub are

$$\{f\}_H = \{f_c\}_H \cos \omega_f t + \{f_s\}_H \sin \omega_f t \qquad (55)$$

Vectors $\{f_c\}_H$ and $\{f_s\}_H$ are 6X1 component vectors of cosine and sine terms in equation (55). For a N-bladed rotor with identical blades, frequency ω_f is equal to $nN\Omega$, where n is an integer and Ω is the rotor speed. Forces and moments at frequency ω_f are the only vibratory forces that can be transmitted to the non-rotating axis at the hub.

To calculate elements of the rotor impedance matrix in aeroelastic analysis G400, the rotor hub is perturbed harmonically in the fore-aft direction by a displacement $u_c \cos \omega_f t$. This displacement causes a force perturbation acting on the hub. The reaction force acting on the hub can be expressed as

$$\{r\}_H = \{f_c\}_H \cos \omega_f t + \{f_s\}_H \sin \omega_f t$$
$$-\{z_{c1}\} u_c \cos \omega_f t - \{z_{s1}\} u_c \sin \omega_f t \qquad (56)$$

The 6X1 reaction force is equal to the constrained hub forces augmented by terms which are proportional to the hub fore-aft displacement, u_c. The 6X1 column vectors $\{z_{c1}\}$ and $\{z_{s1}\}$ are columns of the impedance matrix. Elements in these vectors are assumed to be constant. In a similar way, lateral perturbations of the hub, $v_c \cos \omega_f t$, are introduced to derive impedance columns $\{z_{c2}\}$ and $\{z_{s2}\}$. This procedure is repeated for all possible displacements at the hub, including displacements proportional to $\sin \omega_f t$. The complete rotor impedance matrix and the expression for the hub reactions including all hub displacements is obtained.

The following definitions express harmonic coefficients for the hub reactions as functions of the impedance matrix. The 6X1 hub reactions are assumed to be

$$\{r\}_H = \{r_c\}_H \cos \omega_f t + \{r_s\}_H \sin \omega_f t \tag{57}$$

The 6 X 1 hub displacement perturbation vector is

$$\{x\}_H = \{x_c\}_H \cos \omega_f t + \{x_s\}_H \sin \omega_f t \tag{58}$$

with

$$\{x\}_H^T = \{u,\ v,\ w,\ \theta_1,\ \theta_2,\ \theta_3\}^T \tag{59}$$

Expressions similar to equation (59) define $\{x_c\}_H$ and $\{x_s\}_H$

Equating the coefficient expressions for $\cos \omega_f t$ and $\sin \omega_f t$ in the reaction force equation to zero yields

$$\begin{Bmatrix} \{r_c\}_H \\ \{r_s\}_H \end{Bmatrix} = \begin{Bmatrix} \{f_c\}_H \\ \{f_s\}_H \end{Bmatrix} - z_H \begin{Bmatrix} \{x_c\}_H \\ \{x_s\}_H \end{Bmatrix} \tag{60}$$

$$z_H = \left[\begin{array}{c|c} z_{11H} & z_{12H} \\ \hline z_{21H} & z_{22H} \end{array}\right] \tag{61}$$

Matrix z_H is a 12 X 12 rotor hub impedance matrix composed of four 6 X 6 submatrices z_{11H}, z_{12H}, z_{21H}, z_{22H} as shown in equation (61). The hub reaction force in equation (60) is composed of fixed hub forces $\{f_c\}_H$, and $\{f_s\}_H$ and a correction proportional to the impedance matrix z_H multiplied by the hub displacement vector. Substituting equation (61) into (60) and rearranging the terms yields

$$\left[\begin{array}{c|c} Z_{11H} & Z_{12H} \\ \hline Z_{21H} & Z_{22H} \end{array}\right] \left\{\begin{array}{c} \{x_c\}_H \\ \hline \{x_s\}_H \end{array}\right\} = \left\{\begin{array}{c} \{f_c\}_H \\ \hline \{f_s\}_H \end{array}\right\} - \left\{\begin{array}{c} \{r_c\}_H \\ \hline \{r_s\}_H \end{array}\right\} \qquad (62)$$

To develop the algorithm for assembling impedance properties in equation (62) with properties of other substructures expressed in mass, damping, and stiffness form, a rotor impedance substructure is introduced. This has null mass, damping, and stiffness matrices, and non-zero hub force and moment excitation and rotor hub impedance. The vector of the dependent coordinates X_D is expressed as

$$X_D = (X_D)_C \cos \omega_f t + (X_D)_S \sin \omega_f t \qquad (63)$$

External forces F_D and reactions R_D are expressed similarly. Substructure mass, damping, and stiffness matrices are collected with impedances to yield

$$\left[\begin{array}{c|c} -\omega_f^2 M_D + K_D + Z_{11D} & \omega_f C_D + Z_{12D} \\ \hline -\omega_f C_D + Z_{21D} & -\omega_f^2 M_D + K_D + Z_{22D} \end{array}\right] \left\{\begin{array}{c} (X_D)_C \\ \hline (X_D)_S \end{array}\right\}$$

$$= \left\{\begin{array}{c} (F_D)_C \\ \hline (F_D)_S \end{array}\right\} - \left\{\begin{array}{c} (R_D)_C \\ \hline (R_D)_S \end{array}\right\} \qquad (64)$$

Vectors $(X_D)_C$ and $(X_D)_S$ contain rotor hub coordinates $\{x_c\}_H$ and $\{x_s\}_H$ from equation (62). In equation (64), the partitioned matrices are diagonal. Matrices M_D, C_D, and K_D are typified by

$$M_D = \begin{bmatrix} [m]^{(1)} & & & \\ & [m]^{(2)} & & \\ & & [O]_H & \\ & & & [m]^{(n)} \end{bmatrix} \qquad (65)$$

Zero diagonal submatrices $[O]_H$ are associated with coordinates $\{x_c\}_H$ and $\{x_s\}_H$ which have no mass, damping, or stiffness matrices in the rotor impedance substructure defined by equation (62). The impedance matrix Z_{11D} in equation (64) is

$$Z_{11D} = \begin{bmatrix} [O]^{(1)} & & & \\ & [O]^{(2)} & & \\ & & z_{11H} & \\ & & & [O]^{(n)} \end{bmatrix} \qquad (66)$$

The matrix in equation (66) is zero except for a 6 X 6 diagonal element z_{11H} associated with hub vector $\{x_c\}_H$. Element z_{11H} derives from the impedance substructure defined in equation (62). The forms of impedance matrices Z_{12D}, Z_{21D}, Z_{22D} in equation (64) are similar to equation (66).

Substructure RE3 which models a rotor hub excitation force and a hub impedance matrix incorporates the properties described above. Each 6 X 6 mass, damping, and stiffness matrix for RE3 is zero. Substructure impedance elements and hub excitation forces are transmitted from external aeroelastic analysis G400.

The derivation of the transformation to independent coordinates is accomplished by substituting equation (63) for X_D and equation (24) for X_I into equation (4). This yields

$$(X_D)_c = \beta X_c \tag{67}$$

$$(X_D)_s = \beta X_s \tag{68}$$

Substitution of equation (67) and (68) in equation (64) and pre-multiplication of equation (64) by

$$\begin{bmatrix} \beta^T & O \\ O & \beta^T \end{bmatrix} \tag{69}$$

yields equation (27) for the vibratory response of the coupled system given by

$$\begin{Bmatrix} X_c \\ --- \\ X_s \end{Bmatrix} = \begin{bmatrix} -\omega_f^2 M+K+Z_{11} & +\omega_f C+Z_{12} \\ -\omega_f C+Z_{21} & -\omega_f^2 M+K+Z_{22} \end{bmatrix}^{-1} \begin{Bmatrix} F_c \\ --- \\ F_s \end{Bmatrix} \tag{27}$$

Impedance matrix mappings yielding the matrices in equation (27) are

$$Z_{11} = \beta^T Z_{11D} \beta \tag{70}$$

$$Z_{12} = \beta^T Z_{12D} \beta \tag{71}$$

$$Z_{12} = \beta^T Z_{21D} \beta \tag{72}$$

$$Z_{22} = \beta^T Z_{22D} \beta \tag{73}$$

In the computer program implementation the zero mass, damping and stiffness properties of substructure RE3 are assembled with the properties of other substructures to form M_D, C_D, and K_D in equation (1). These matrices are mapped to the independent coordinate system by equations (6) through (8). The forced response solution mode is invoked and matrices in equation (26) are formed. Impedance matrices are mapped to independent coordinates by equations (70) through (73) and are added to the matrices of equation (26) to form equation (27). Equation (27) yields the vibratory response of systems including a rotor impedance model.

Hub reactions can be recovered from equations (67), (68), and (64) after the coupled system solution is found from equation (27).

The RE3 impedance substructure is consistent only with a steady state forced response mode of solution, FR1. The forcing frequency in FR1 must be the same as the forcing frequency used to derive rotor impedance properties. This frequency will be an integer multiple of rotor speed and blade number ($\omega_f = nN\ \Omega$).

BASE PROGRAM SUBSTRUCTURES

Substructures available in the Base Program listed in Table 3 are described below. Descriptions are provided of substructure function, coordinates, properties, and assumptions.

Substructure FA1

The function of substructure FA1 is to simulate a vibration absorber which may be attached to any other substructure in the fixed - i.e., non-rotating-system. Substructure FA1 has seven coordinates. These are absorber mass displacement, and six

TABLE 3 - BASE PROGRAM SUBSTRUCTURES

COMPONENT FLAG	DESCRIPTION OF COMPONENT
FA1	FIXED ABSORBER 1 - Single mass, spring and damper vibration absorber.
GF1	GENERALIZED FORCE 1 - Force component allowing specification of harmonic force and moment excitation.
BM1	BEAM MODEL 1 - Uniform elastic beam segment.
CN1	CONSTRAINT COMPONENT 1 - Component allowing elimination of coordinates (degrees of freedom) from a connection node.
RE2	ROTOR ELASTIC 2 - Model of aeroelastic rotor expressed in mass, damping, and stiffness form. Rotor data are transmitted to the Base Program by rotor aeroelastic analysis E927. Restricted to hover.
MS1	MODAL SUBSTRUCTURE 1 - Normal mode representation of a dynamical structure.
BF1	BIFILAR 1 - Horizontal linear bifilar vibration absorber for reducing rotor inplane vibrations.
BF2	BIFILAR 2 - Vertical linear bifilar vibration absorber for reducing rotor out of plane vibrations.
IS1	ISOLATOR 1 - Nodal isolator employing two anti-resonant bar weights.
RE3	ROTOR ELASTIC 3 - Impedance model of aeroelastic rotor in hover or forward flight. A hub force and moment excitation vector and a hub impedance matrix are transmitted to the Base Program by rotor aeroelastic analysis G400. Vibratory response of a coupled system is found using solution mode FR1. This component has a capability to obtain optimal HHC control angles for vibration reduction.

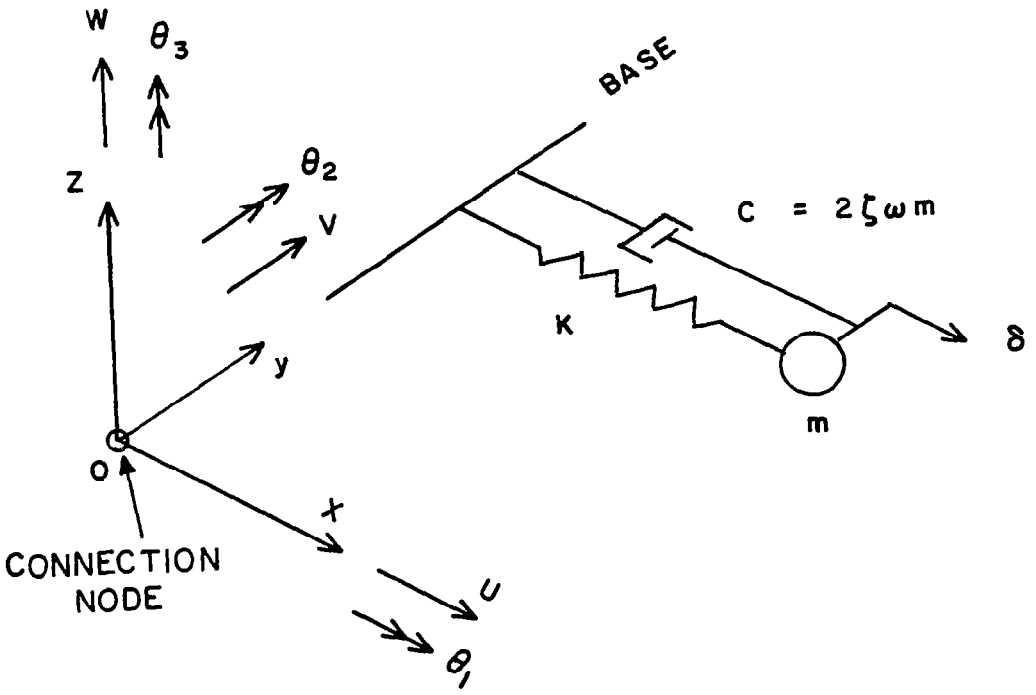

Figure 5. Fixed Absorber FA1.

displacements of the base consisting of three linear base displacements and three angular base rotations. The mass of the absorber is free to move perpendicular to the base and does not move parallel to the base. Viscous damping is assumed. Figure 5 illustrates substructure FA1 properties. Initial mass displacement and velocity can be specified for transient response analysis.

Substructure GF1

Generalized Force 1, GF1, specifies a harmonic force and moment excitation acting at a point on a structure. The GF1 substructure has six coordinates, comprising three linear displacements and three angular rotations at a connection node. Forces and moments are resolved to a non-rotating axis system. The user specifies the cosine and sine coefficients of these forces and moments to define a harmonic excitation of known magnitude. The mass, damping, and stiffness matrices for substructure GF1 are null matrices. Substructure GF1 may be used to represent an excitation for forced response (FR1) or time-history (TH1) solution modes. Substructure GF1 may be included in eigensolution (EG1 and EG2) input streams without affecting the final eigensolution. Figure 6 illustrates substructure GF1 properties.

Substructure BM1

Beam Model 1, BM1, is a uniform elastic beam. This substructure has 12 coordinates consisting of three linear displacement and three angular rotations at each end of the beam. The beam may be connected to other substructures. The uniform mass of the beam, m_o, is approximated by two concentrated masses equal to $m_o/2$ at its ends. The beam is assumed to have zero mass moments of inertia associated with bending and torsion rotations. Structural damping is assumed to be zero. Figure 7 illustrates substructure BM1 properties.

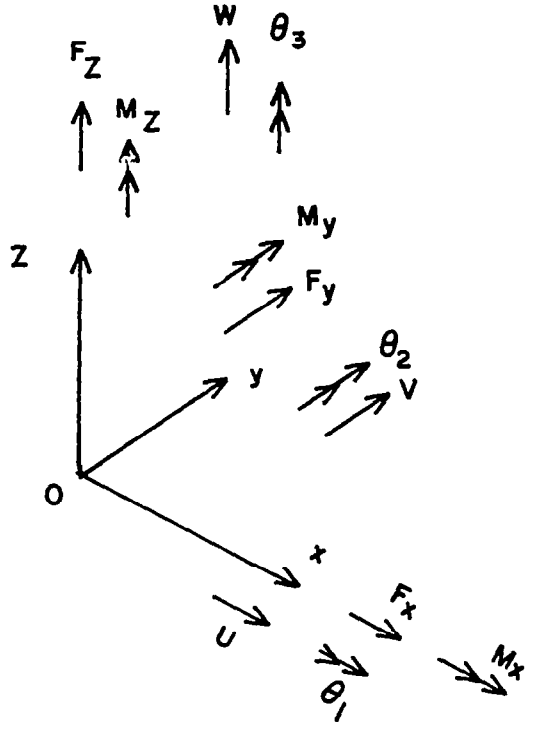

Figure 6. Generalized Force GF1.

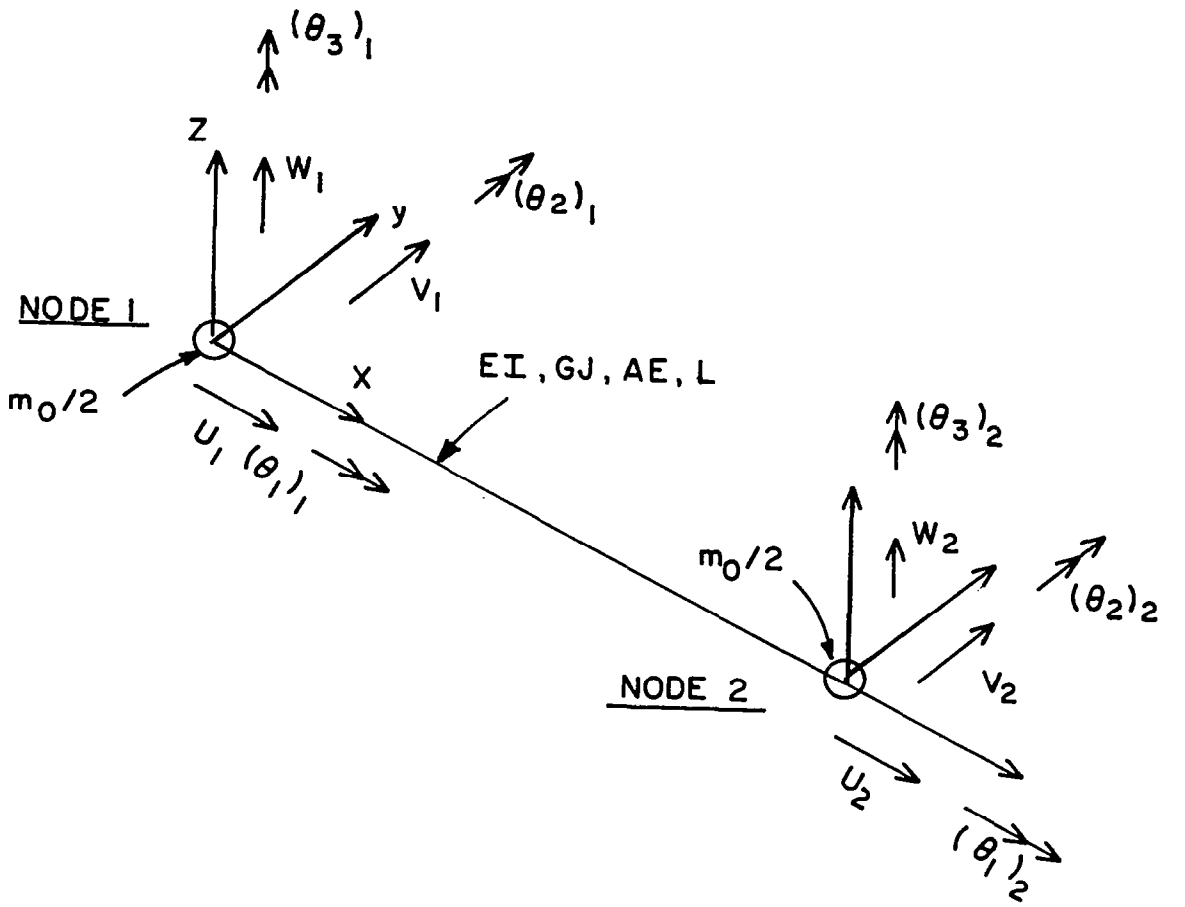

Figure 7. Uniform Beam Segment BM1.

Constraint Substructure CN1

Constraint substructure CN1 may be used to eliminate or constrain coordinates at a connection node. There are six coordinates at each connection node (see Figure 2). The coordinates consist of three linear displacements and three angular rotations. The user may constrain any five of the six coordinates at a connection node. At least one coordinate among the six must be retained. The constraint component is a specialized modal substructure (see Substructure MS1) whose modal matrix contains ones and zeroes. The occurrence of a one in a modal matrix row causes a connection node coordinate to be replaced by a modal coordinate which is identical to the connection coordinate. The occurrence of zeroes in a modal matrix row eliminates a connection node coordinate. Equation (20) explains how the connection node coordinates are eliminated. Matrix $[E]^T$, containing the rotation transformation from local to global axes is replaced by the identity matrix I. The number of coordinates in vector {q} is selected to be equal to the retained coordinates at the connection node. The coordinates in vector {q} are identical to coordinates to be retained at the connection.

Rotor Aeroelastic Substructure RE2 and External Program E927

Rotor aeroelastic substructure RE2 is used to represent a multi-blade aeroelastic rotor in hover. This component identifies rotor matrices transmitted from the rotor aeroelastic analysis E927 and arranges the rotor data for assembly with other components. Standard application of RE2 is in conjunction with eigensolution mode EG2.

Table 4 lists RE2 coordinates, expressed as output labels displayed by the Base Program. Use of rotor coordinates in the rotor

TABLE 4 - AEROELASTIC ROTOR RE2 COORDINATE LABELS

COORDINATE OUTPUT LABEL	DESCRIPTION
QFT1-QFT4	Blade bending collective modal amplitude[a]
THTR	Blade pitching[b]
THTE	Blade torsion[b]
BETA	Flapping collective mode[c]
GAMA	Leading collective mode[d]
QT1S, QT1C QT2S, QT2C QT3S, QT3C QT4S, QT4C	Blade bending cyclic sine and cosine modal amplitudes[a]
THRS, THRC	Blade pitching sine and cosine cyclic amplitudes[b]
THES, THEC	Blade torsion sine and cosine cyclic amplitudes[b]
BETS, BETC	Blade flapping sine and cosine cyclic amplitudes[c]
GAMS, GAMC	Blade leading sine and cosine amplitudes[d]
X, Y, Z, THTX, THTY, THTZ	Hub displacements. See Figure 2 for positive directions

NOTES: a) Positive flatwise bending up and edgewise bending forward.
b) Positive nose down.
c) Positive up.
d) Positive forward.

equations, and the assumption of identical blades, equally disposed on the rotor disc, enables a constant coefficient equation set to be derived (see Reference 6). Rotor coordinate selection is made in the input specification to E927. Rotor aeroelastic analysis E927 transmits to a file the number of coordinates, flags defining coordinates selected, and corresponding mass, damping, and stiffness matrices. Matrices embody dynamic and aerodynamic contributions. Numerical input data following the RE2 flag consist of hub connection node number and hub orientation angles. Processing by the Base Program includes the addition of a dummy yaw coordinate. Zero mass, damping, and stiffness matrices are created for this coordinate. This yields a six coordinate hub consistent with coordinate representation for other substructures. Six hub coordinates enable the rotor component to be coupled to other components without changing Base Program assembly logic. A valid physical model of rotor yaw motion is not achieved. Null rotor matrices are associated with this displacement. The user must eliminate the hub yaw coordinate from the system model. This may be accomplished with constraint component CN1. A valid model would occur also if fuselage normal modes in component MS1 have no hub yaw displacement.

Modal Substructure MS1

Modal Substructure MS1 represents a dynamical system employing normal modes of a substructure. Each substructure of MS1 type is limited to the use of one normal mode. The user must supply input defining the modal generalized mass, damping ratio, and frequency of the normal mode. These properties can be generated from analysis or from test data. Processing in the program forms damping and stiffness of the mode from the input data. Each substructure of type MS1 is allowed to have up to five nodes at

which node number, structure orientation angles, and elements of the modal matrix for the normal mode are defined. At each such node, the elements of the modal matrix are three linear displacements and three angular rotations for a unit value of the normal mode amplitude. The directions of the displacements at a node must be consistent with the convention shown in Figure 2. The specification of the same node number between two substructures of any type leads to the connecting of the two substructures at the node. More than one modal substructure of type MS1 is connected to the same node when it is desired to represent the effects on a node of several normal modes. Nodes on MS1 substructures may be used to monitor airframe responses at up to five points. If a physical substructure is not connected to a node at which responses are desired, these responses may be displayed by connecting a GF1 substructure to the node of interest, with zero forces and moments specified. This GF1 substructure contributes no matrices or forces to the system. It introduces physical displacements at the node which become members of the set of dependent system coordinates which are used to monitor the node response. Initial modal amplitudes and velocities can be specified to analyze system transient response.

Horizontal Linear Bifilar BF1

Horizontal linear bifilar BF1 represents a bifilar vibration absorber designed to reduce N per rev vibrations in the plane of rotation of a helicopter rotor. The bifilar absorber is assumed to consist of N arms equal in number to the rotor blades. Each arm holds a pendular mass free to lead or lag. The arms are assumed to be equally disposed and each holds an identical absorber mass. The bifilar absorber rotates at the helicopter rotor speed Ω. Figure 8 is a schematic of one arm of the bifilar. Each bifilar mass lead-lag displacement may be expressed as the sum of bifilar lead-lag collective and cyclic displacements. The lead-lag displacement γ_n of the n-th bifilar is

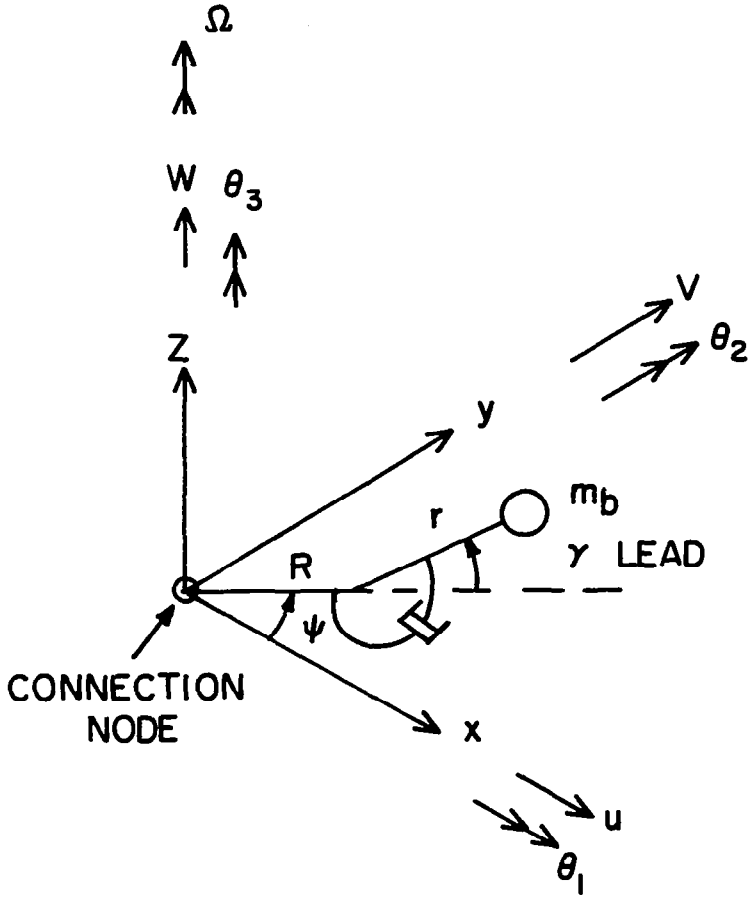

N MASSES, ONLY ONE MASS SHOWN

$$\gamma = (\gamma_c \cos\psi + \gamma_s \sin\psi)(2/N)$$

Figure 8. Horizontal Linear Bifilar BF1.

$$\gamma_n = \gamma_o/N + (\gamma_c \cos\psi_n + \gamma_s \sin\psi_n)(2/N) \quad (74)$$

$$\psi_n = (2\pi/N)(n-1) + \psi \quad (75)$$

$$\psi = \Omega t \quad (76)$$

Equation (74) introduces the bifilar collective and cyclic coordinates in the equations of motion of the bifilar. The angle ψ_n is the azimuth angle of the n-th bifilar arm. The equations of motion for each bifilar consist of N equations defining the equilibrium of moments about the hinge point of each pendular mass. These N equations are supplemented by six equations defining the equilibrium of the bifilar hub in three translational and three rotational directions. When equation (74) is substituted into these equations, an equation set with eight coordinates is obtained. The assumption is made that $\gamma_o = 0$. The eight coordinates consist of two bifilar mass sine (γ_s) and cosine (γ_c) cyclic amplitudes and six hub displacements shown in Figure 8. The reduced equation set has constant coefficients. Restrictions on the configurations that can be analyzed are bifilars which have three or more equally disposed and equal masses. Pendulum displacements are assumed to be small enough to permit linearizations of the equations. Solutions are obtained in terms of the cyclic amplitudes γ_c and γ_s, as functions of time. Solution modes that may be used with BF1 are FR1, EG1, EG2, and TH1. Initial values of bifilar mass cyclic mode amplitudes can be specified for transient analysis.

Horizontal bifilars are tuned to eliminate hub vibrations induced by forces referred to the rotating system at frequencies (N-1) Ω or (N+1) Ω, respectively. These forces are transformed to forces with frequency NΩ resolved to non-rotating axes. Thus, two separate horizontal bifilars are required to eliminate NΩ forces resolved to the fixed system. Post-processing of response results

obtained from the system solution may be required to evaluate horizontal bifilar designs. The Sample Applications section illustrates post-processing of γ_c and γ_s responses. A formula is given (see equation (101)) expressing the bifilar mass (N-1) Ω displacement in terms of γ_c and γ_s to permit comparisons to be made with measured bifilar mass accelerations.

Vertical Linear Bifilar BF2

Vertical linear bifilar BF2 represents a bifilar vibration absorber designed to reduce N per rev vibrations perpendicular to the plane of rotation of a helicopter rotor. The bifilar absorber is assumed to consist of N arms equal in number to the rotor blades. Each arm holds a pendular mass free to flap up or down. The arms are assumed to be equally disposed and each holds an identical absorber mass. The bifilar absorber rotates at the helicopter rotor speed Ω. Figure 9 is a schematic one arm of the bifilar. The derivation of the equations of motion employed in the BF2 model is similar to the derivation described in the previous section for bifilar BF1. Each bifilar mass flapping displacement is expressed as the sum of a bifilar flapping collective and cyclic displacements.

$$\beta_n = \beta_o/N + (\beta_c \cos \psi_n + \beta_s \sin \psi_n)\ (2/N) \qquad (77)$$

Substitution of equation (77) into the equations of motion (see previous section for a similar discussion) yields a nine coordinate constant coefficient equation set. The nine coordinates consist of bifilar mass collective (β_o) sine cyclic (β_s), and cosine cyclic (β_c) amplitudes, and six hub displacements shown in Figure 9. Restrictions on the configurations that can be analyzed are bifilars which have three or more equally disposed and identical masses. Solution modes that may be used with BF2 are FR1, EG2, and TH1. Initial values of bifilar mass collective, and cyclic amplitudes may be specified for transient analysis.

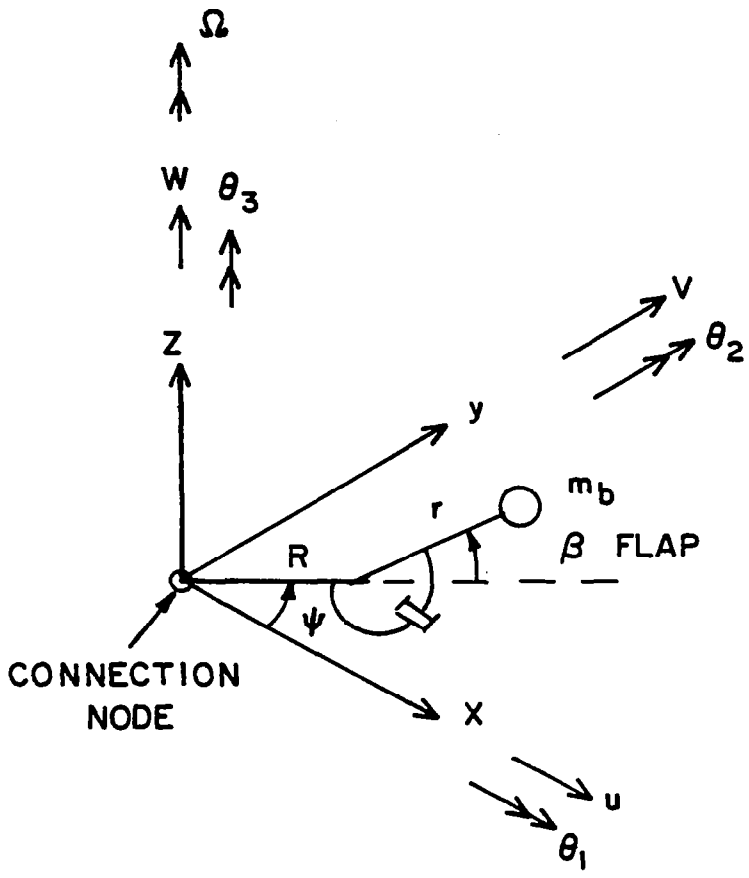

N MASSES, ONLY ONE MASS SHOWN

$$\beta = \beta_0/N + (\beta_c \cos\psi + \beta_s \sin\psi)(2/N)$$

Figure 9. Vertical Linear Bifilar BF2.

Vertical bifilars are tuned to eliminate hub vibrations induced by forces referred to the rotating system at a frequency equal to NΩ. These forces transform to NΩ forces resolved to non-rotating axes. Post-processing of response results obtained from the system solution may be required to evaluate vertical bifilar designs. The approach is analogous to that described for the horizontal bifilar (see previous section).

Vibration Isolator IS1

Vibration isolator IS1 is a nodal isolator which may be placed between an excitation source, like the rotor/transmission system, and an airframe, to minimize vibrations on the airframe. The concept of the nodal isolator is described in Reference 7. The isolator employs a pivoted bar weight to balance spring and inertia forces to create a node or point of zero vibratory motion at the airframe attachment. When damping is present, vibrations are minimized at the airframe attachment at the excitation frequency. In coupled rotor/airframe systems the excitation frequency is N per rev where N is the number of rotor blades. Figure 10 illustrates the basic nodal isolator, whose coordinates are upper and lower mass displacements. The antiresonant bar displacement is a function of upper and lower mass displacements.

The upper mass simulates the rotor/transmission system. The lower mass simulates the airframe. Design variables are spring rate, antiresonant bar weight, bar weight overhang, and distance between bar pivots. Variables are selected to achieve minimum vibrations at a point on the airframe at a desired excitation frequency applied by rotor/transmission A. Design variables are selected to protect the isolator from resonance at the rotor excitation frequency. Reference 7 describes the dynamic attributes of the system.

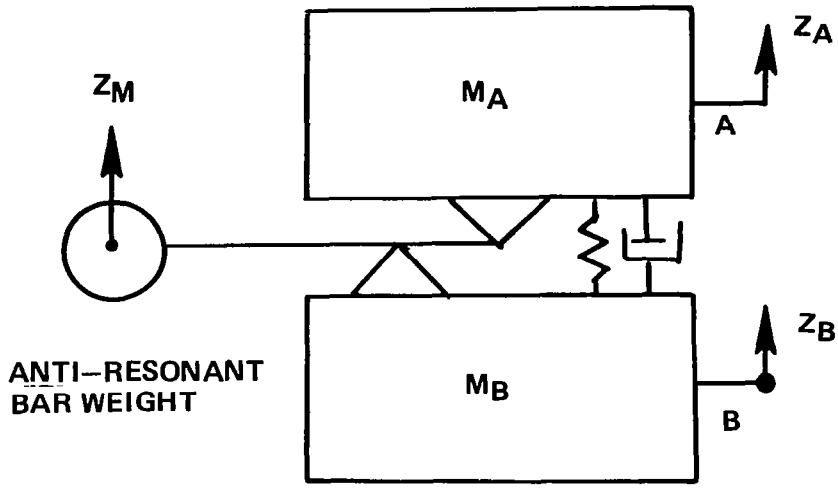

Figure 10. Basic Nodal Isolator.

Nodal isolator IS1 generalizes the isolator concept to introduce six translational and rotational displacements at each upper and lower isolator attachment. The antiresonant bar weight is allowed to translate in three directions. Figure 11 illustrates the physical isolator and a schematic corresponding the physical isolator. Figure 11 does not show a second antiresonant bar weight included in the mathematical model. The lower bar weight permits additional design flexibility and is shown in Figure 12. The isolator transmission attachment (node 1) in Figure 11 corresponds to A in Figure 10. The isolator airframe attachment (node 2) corresponds to B in Figure 10. Six coordinates at each attachment added to three coordinates for each antiresonant bar weight sum to a total of eighteen coordinates for IS1. Connection node numbers and Euler angles defining the isolator bar orientation are associated with each attachment. These attributes enable the isolator bars to be connected and assembled with any other substructures of the Base Program. A subsequent section (see Sample Applications) describes a configuration assembled from four isolator bars of type IS1 to create a "six degree-of-freedom" nodal isolator. Nodal isolator IS1 can be specialized to the isolator shown in Figure 10.

Rotor Aeroelastic Substructure RE3 and External Program G400

Rotor aeroelastic substructure RE3 is used to represent a multiblade aeroelastic rotor in forward flight or hover. The rotor representation in this substructure is defined by a rotor hub excitation force and moment vector and a rotor impedance matrix. The force and moment vector and impedance matrix may be generated by the G400 aeroelastic analysis. The Base Program combines the aeroelastic rotor representation with the impedance elements of other dynamical components to form a coupled system. The definitions of the rotor hub force excitation vector and rotor impedance matrix are given in a preceding section (Assembly of

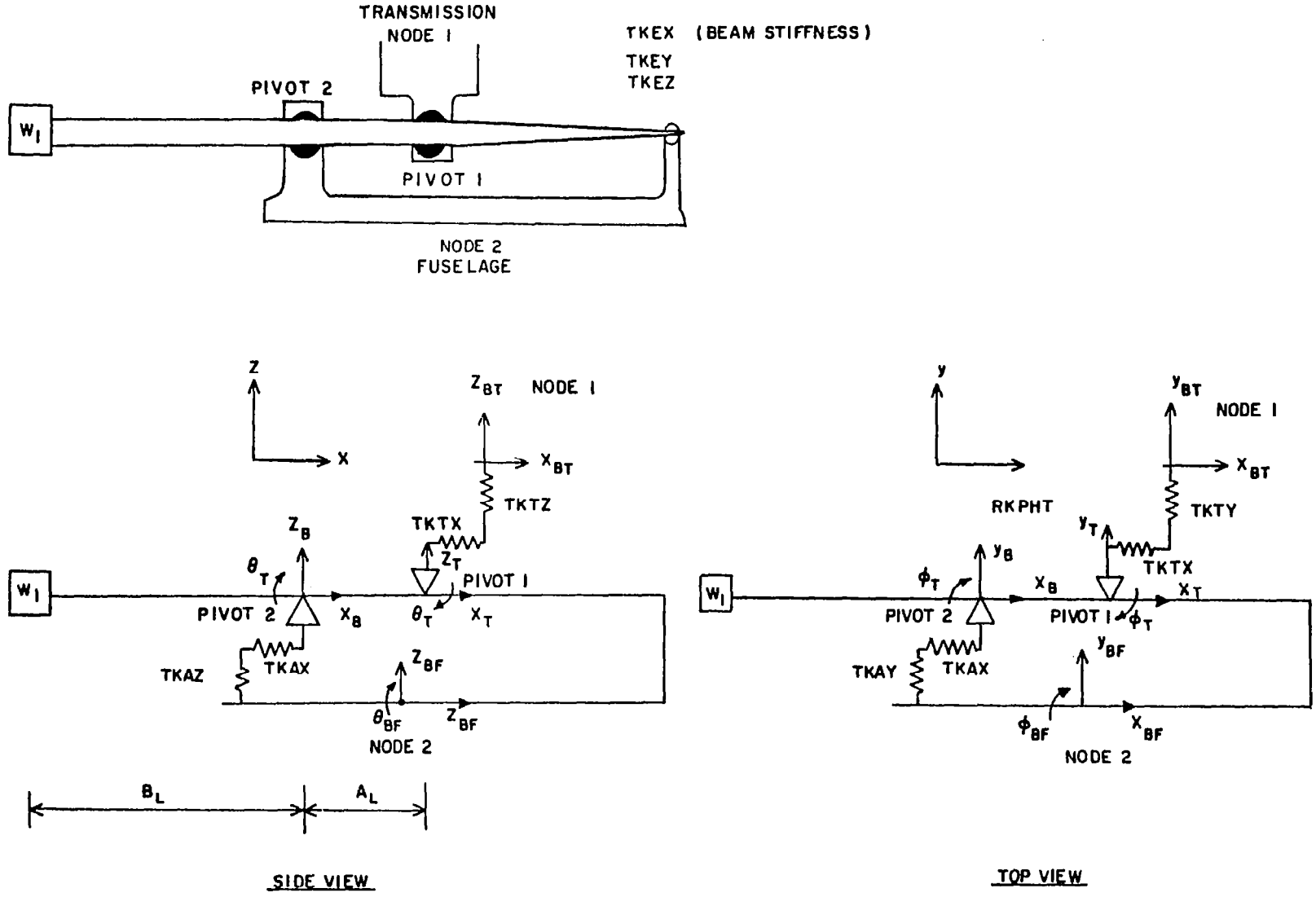

Figure 11. Vibration Isolator IS1.

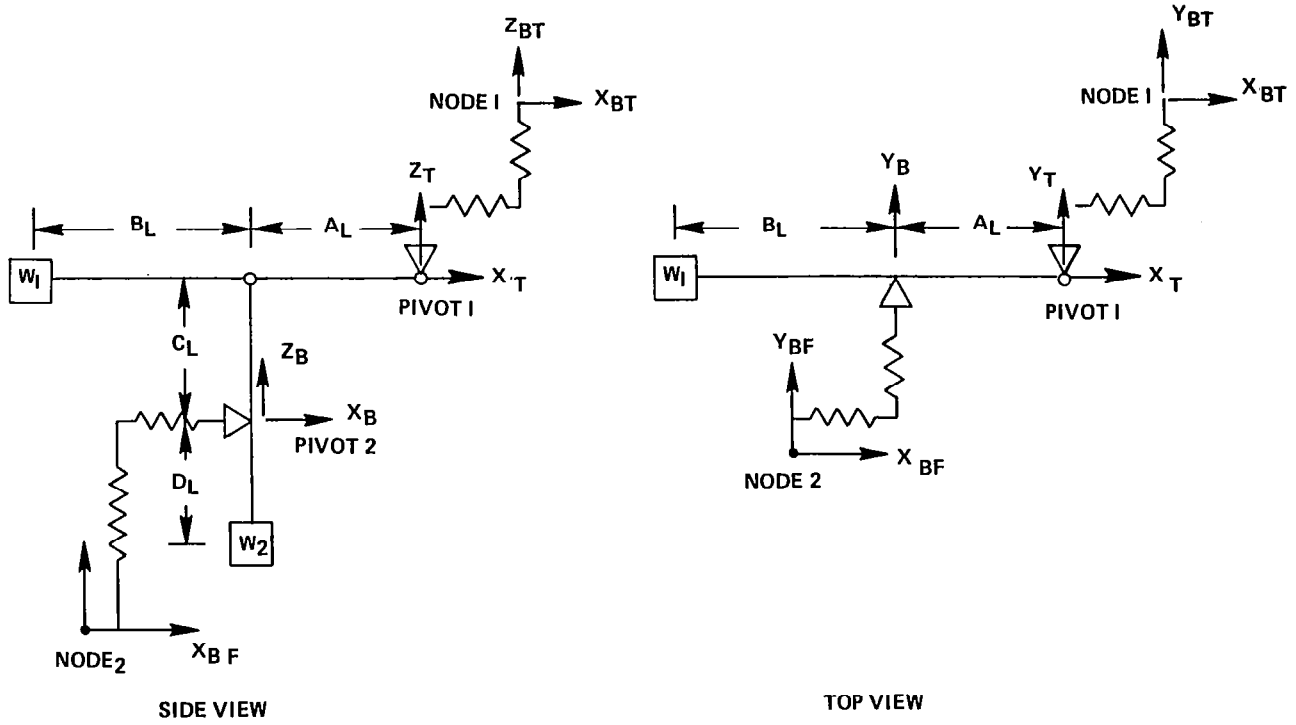

Figure 12. Schematic Showing Nodal Isolator with Second Antiresonant Bar Weight.

Rotor Impedance Matrix). The coordinates represented in the RE3 substructure are the six hub displacements listed in equation (59). The RE3 rotor impedance substructure is limited to the steady state forced response solution mode, FR1. The frequency of force excitation specified in FR1 must be the same as that specified for G400 to derive the rotor impedance matrix. This frequency must be an integer multiple of rotor speed and blade number ($\omega_f = nN\Omega$). Component RE3 may be flagged to calculate Higher Harmonic Control (HHC) angles to minimize vibrations, such as described in a later section (Higher Harmonic Control for Vibration Reduction). Optimal control angles, and blade stresses resulting from hub displacements and HHC control inputs may be calculated. This is achieved by utilizing data from G400 defining the effects on hub loads and blade stresses of HHC angle perturbations and hub displacements. Table 5 summarizes G400 capabilities.

Component RE3 may also be used to represent the impedance of a substructure which is not a rotor, such as an empennage. Aerodynamic dampings may be represented in the impedance matrix. Structural and inertial contributions to the impedance matrix may also be included.

HIGHER HARMONIC CONTROL FOR VIBRATION REDUCTION

Higher harmonic control (HHC) is a concept for helicopter vibration reduction which employs high frequency blade pitch controls to reduce helicopter vibrations. Vibration reduction is accomplished by modification of vibratory forces and moments acting on the rotor blades, such that the resultant hub forces and moments are reduced. This section describes the approach used in the Coupled Rotor/Airframe Vibration Analysis to calculate helicopter vibrations for specified HHC angles and to calculate optimal HHC control angles for minimum vibrations.

TABLE 5 - CAPABILITIES OF G400 ROTOR AEROELASTIC ANALYSIS

- Rotor Type
  - Conventional articulated
  - Composite bearingless
  - Teetering
- Blade
  - Redundant torque tube flex beam
  - Pendulum absorbers
  - Structural twist
  - Aerodynamic twist
- Aerodynamics
  - Static aerodynamic data
  - Unsteady data
  - Nonuniform rotor induced inflow
- Stress Calculation
  - Mode deflection
  - External force integration
- Mathematical
  - Uncoupled normal modes
  - Time history solution
  - Hub force and moment excitation vector and rotor impedance matrix
  - Higher harmonic control matrices

Higher harmonic control may be achieved by superimposing non-rotating swashplate motions at the blade passage frequency upon the collective and cyclic control inputs at Ω. The blade passage frequency is $N\Omega$ for an N bladed rotor. The $N\Omega$ cyclic motions of the non-rotating swashplate transform to $(N-1)\Omega$ and $(N+1)\Omega$ blade pitch motions referred to the rotating system. The $N\Omega$ collective motion of the swashplate results in $N\Omega$ blade pitch changes in the rotating system. The harmonic coefficients of the blade pitch angle referred to the rotating system may be expressed as

$$\theta_C^T = \{\theta_{N-1} \ , \ \theta_N \ , \ \theta_{N+1}\}_C^T \tag{78}$$

$$\theta_S^T = \{\theta_{N-1} \ , \ \theta_N \ , \ \theta_{N+1}\}_S^T \tag{79}$$

The elements of the vectors in equations (78) and (79) are the coefficients of cosine and sine terms in the pitch angle expression with frequencies $(N-1)\Omega$, $N\Omega$, and $(N+1)\Omega$. The control inputs induce rotor forces and moments at $N\Omega$ in the non-rotating system.

Higher harmonic control angles are perturbed in the G400 analysis to obtain a transfer matrix h_H. Matrix h_H relates the rotor hub reaction forces to HHC control perturbations, and enables HHC to be introduced in the Coupled Rotor/Airframe Analysis. Successive perturbing of HHC controls enables columns of the transfer matrix to be identified. The procedure is similar to the determination of the rotor impedance matrix leading to equation (60). The resulting expression for the harmonics of hub reaction force at frequency $N\Omega$ is

$$\begin{Bmatrix} \{r_c\}_H \\ \{r_s\}_H \end{Bmatrix} = \begin{Bmatrix} \{f_c\}_H \\ \{f_s\}_H \end{Bmatrix} - Z_H \begin{Bmatrix} \{x_c\}_H \\ \{x_s\}_H \end{Bmatrix} + h_H \begin{Bmatrix} \theta_c \\ \theta_s \end{Bmatrix} \tag{80}$$

$$h_H = \left[\begin{array}{c|c} h_{11H} & h_{12H} \\ \hline h_{21H} & h_{22H} \end{array}\right] \tag{81}$$

Equation (80) is the same as equation (60) with an additional term involving the HHC angles. Matrix h_H has dimensions 12x6. Each submatrix h_{11H}, h_{12H}, h_{21H}, h_{22H} in equation (81) has dimension 6x3. Each of the control vectors θ_c and θ_s has dimensions 3x1 as shown by equations (78) and (79).

Assembly of the rotor hub excitation forces induced by HHC with the properties of other substructures is achieved by utilizing substructure RE3. The assembly procedure parallels the hub force and moment assembly described in a preceding section (see Assembly of Rotor Impedance Matrix). The resulting system equation expressed in terms of dependent coordinates is

$$\left[\begin{array}{c|c} -\omega_f^2 M_D + K_D + Z_{11D} & \omega_f C_D + Z_{12D} \\ \hline -\omega_f C_D + Z_{21D} & -\omega_f^2 M_D + K_D + Z_{22D} \end{array}\right] \left\{\begin{array}{c} (X_D)_c \\ \hline (X_D)_s \end{array}\right\}$$

$$= \left\{\begin{array}{c} (F_D)_c \\ \hline (F_D)_s \end{array}\right\} - \left\{\begin{array}{c} (R_D)_c \\ \hline (R_D)_s \end{array}\right\} + \left[\begin{array}{c|c} H_{11D} & H_{12D} \\ \hline H_{21D} & H_{22D} \end{array}\right] \left\{\begin{array}{c} \theta_c \\ \hline \theta_s \end{array}\right\} \tag{82}$$

Terms in equation (81) are the same as the terms in equation (64) except for the HHC terms. Matrix H_{11D} in equation (82) is

$$H_{11D} = \begin{Bmatrix} [0]^{(1)} \\ [0]^{(2)} \\ \vdots \\ h_{11H} \\ \vdots \\ [0]^{(n)} \end{Bmatrix} \tag{83}$$

The matrix in equation (83) is zero except for 6x3 element h_{11H} which derives from equations (80) and (81). The forms of matrices H_{12D}, H_{21D}, H_{22D} in equation (82) are similar to equation (83). The row dimensions of the zero rectangular matrix $[0]^{(i)}$ is equal to the number of coordinates for the i-th substructure in the system. The column dimension of this submatrix is 3.

The transformation from dependent to independent coordinates for the system is analogous to the derivation in equations (67) to (73). The resulting system response is

$$\begin{Bmatrix} X_c \\ --- \\ X_s \end{Bmatrix} = \begin{Bmatrix} X_{co} \\ --- \\ X_{so} \end{Bmatrix} + T \begin{Bmatrix} \theta_c \\ \\ \theta_s \end{Bmatrix} \tag{84}$$

$$\begin{Bmatrix} X_{co} \\ --- \\ X_{so} \end{Bmatrix} = A \begin{Bmatrix} F_c \\ --- \\ F_s \end{Bmatrix} \tag{85}$$

$$A = \left[\begin{array}{c|c} -\omega_f^2 M + K + Z_{11} & \omega_f C + Z_{12} \\ \hline -\omega_f C + Z_{21} & -\omega_f^2 M + K + Z_{22} \end{array}\right]^{-1} \qquad (86)$$

$$T = A\,H \qquad (87)$$

$$H = \left[\begin{array}{c|c} H_{11} & H_{12} \\ \hline H_{21} & H_{22} \end{array}\right] \qquad (88)$$

$$\begin{aligned} H_{11} &= \beta^T H_{11D} \\ H_{12} &= \beta^T H_{12D} \\ H_{21} &= \beta^T H_{21D} \\ H_{22} &= \beta^T H_{22D} \end{aligned} \qquad (89)$$

Equation (85) is the same as equation (27) derived in a preceding section (Assembly of Rotor Impedance Matrix). Equation (85) yields the system response including a rotor, without HHC. Equation (84) yields the system response when HHC is specified. It is essentially the same as equation (1) in Reference 11.

Matrix T is the transfer matrix relating HHC inputs to vibratory response. The dimensions of the matrices introduced in equation (84) are: T = 2Nx6, A = 2Nx2N, H = 2Nx6, H_{11}, H_{12}, H_{21}, H_{22} = Nx3 where N is the number of coordinates in the independent coordinate system.

To derive the control angle vector for minimum vibrations, a scalar performance index J is defined.

$$J = \{Y_c^T \;\vdots\; Y_s^T\} \left[\begin{array}{c|c} W_z & 0 \\ \hline 0 & W_z \end{array}\right] \left\{\begin{array}{c} Y_c \\ \hline Y_s \end{array}\right\}$$

$$+\{\theta_c^T \;\vdots\; \theta_s^T\} \left[\begin{array}{c|c} W_\theta & 0 \\ \hline 0 & W_\theta \end{array}\right] \left\{\begin{array}{c} \theta_c \\ \hline \theta_s \end{array}\right\} \qquad (90)$$

The control vector must be chosen to minimize J. The vector of response variables Y, whose cosine and sine components are Y_c and Y_s, may be identified with the displacement vector X_D, the interface force vector R_D, or a vector composed of both displacements and interface forces. In this application, Y is selected as

$$Y = X_D \qquad (91)$$

which identifies Y as the dependent coordinate vector. The diagonal weighting matrix W_z permits the weighting of some responses more than others. Diagonal elements may be selected to be zero except at a point on the structure whose displacements are to be minimized. A typical requirement is the weighting of cockpit or tail responses for minimization. Weighting matrix W_z has dimensions N_D x N_D where N_D is the size of the vector of dependent coordinates, X_D.

The 3x3 weighting matrix W_θ limits the amplitudes of the rotor controls. Equation (90) is analogous to equation (2) in Reference 11. The control state for a minimum value of J is obtained by first substituting equation (84) into equations (67) and (68). This yields

$$\begin{Bmatrix} (X_D)_C \\ \hline (X_D)_S \end{Bmatrix} = \begin{Bmatrix} \beta X_{CO} \\ \hline \beta X_{SO} \end{Bmatrix} + \left[\begin{array}{c|c} \beta & 0 \\ \hline 0 & \beta \end{array}\right] T \begin{Bmatrix} \theta_C \\ \hline \theta_S \end{Bmatrix} \qquad (92)$$

Equations (91) and (92) are substituted into equation (90) to express the performance index in terms of control variables. The resulting expression is differentiated with respect to the control variables and equated to zero to obtain the control state for a minimum value of J.

$$\begin{Bmatrix} \theta_C^* \\ \hline \theta_S^* \end{Bmatrix} = -(T^T \left[\begin{array}{c|c} \beta^T W_Z \beta & 0 \\ \hline 0 & \beta^T W_Z \beta \end{array}\right] T + \left[\begin{array}{c|c} W_\theta & 0 \\ \hline 0 & W_\theta \end{array}\right])^{-1} T^T \left[\begin{array}{c|c} \beta^T W_Z \beta & 0 \\ \hline 0 & \beta^T W_Z \beta \end{array}\right] \begin{Bmatrix} X_{CO} \\ \hline X_{SO} \end{Bmatrix} \qquad (93)$$

Equation (93) is analogous to equation (3) in Reference 11, except that it is expressed in terms of cosine and sine components of the independent coordinate vector, X_I. An equivalent version of equation (93) is implemented in the program code to minimize the computer storage requirement. Transformations are applied to the T matrix in the code as opposed to the W_Z matrix such as shown in equation (93).

Substituting equation (93) into equation (92) yields the minimum vibration vector. The optimal control solution and corresponding vibrations are calculated in the Base Program. File data are read to acquire the transfer matrix h_H tramsmitted from G400. A non-linear dependence of h_H on the control state is approximated by deriving h_H for control perturbations centered at prior solutions obtained from the Base Program. The HHC solution is refined by iterating between the Base Program and G400.

Blade stresses and push rod loads are monitored for the effects of rotor hub displacement and higher harmonic control inputs. This is achieved by expanding the harmonic coefficient of a stress in terms of hub displacements and HHC control angles, such as was done for the harmonics of hub reaction force in equation (80).

$$S_n = (S_n)_o + [S_{nH}] \begin{Bmatrix} X_{c\ H} \\ ----- \\ X_{s\ H} \end{Bmatrix} + [S_{n\theta}] \begin{Bmatrix} \theta_c \\ -- \\ \theta_s \end{Bmatrix} \quad (94)$$

Stress coefficient S_n is the n-th harmonic of stress at a point on the rotor blade where n is an integer multiple of rotor speed, Ω. Stress coefficient S_n represents either the flatwise, edgewise, torsion stress, or push rod load. Stress harmonic coefficient S_n is a scalar. The coefficient $(S_n)_o$ is the n-th harmonic coefficient of stress without hub displacement nor HHC controls. Row matrix $[S_{nH}]$ is a 1x12 matrix of coefficients introducing the effects of hub displacement. Row matrix $[S_{n\theta}]$ is a 1x6 matrix of coefficients introducing the effects of HHC controls. Scalar $(S_n)_o$ and matrices $[S_{nH}]$ and $[S_{n\theta}]$ are calculated by G400 and are transmitted to the Base Program. The Base Program calculates the harmonics of stress or push rod load from equation (94). These harmonics are used to calculate the variation of stress or push rod load with time. Peak to peak values are determined in the Base Program.

SAMPLE APPLICATIONS

A discussion is given below of sample applications performed with the Base Program to demonstrate the capabilities of the analysis package. The set of applications exercises each component (substructure or solution mode). The problems were selected for physical significance and ability to test program capabilities and component combinations. Table 6 summarizes the attributes of the Base Program sample problems. A brief description is keyed to a list of components employed for the case.

Base Program Applications

Case 1 was used to verify the functioning of the horizontal linear bifilar BF1 and components GF1, MS1 and FR1. Attributes of the UH-60 system were used. The configuration consists of a bifilar with four pendulum masses, coupled to a modal fuselage with five modes. Shake test data were the source of modal properties. A 4Ω inplane force is applied to the hub to simulate the effects of a rotor. The components of the applied force are resolved to the fixed system and are equal to

$$f_{x1} = 1700 \cos 4\Omega t, \text{ N (lb)} \quad (95)$$

$$f_{y1} = 1100 \sin 4\Omega t, \text{ N (lb)} \quad (96)$$

The above values of the force coefficients are input to GF1. Figure 2 shows the positive directions of the forces. These forces are equivalent to

$$f_{x2} = 1400 \cos 3\Omega t + 300 \cos 5\Omega t, \text{ N (lb)} \quad (97)$$

$$f_{y2} = 1400 \sin 3\Omega t - 300 \sin 5\Omega t, \text{ N (lb)} \quad (98)$$

TABLE 6.- BASE PROGRAM TEST CASES SUMMARY

Case No.	Case Description	BASE PROGRAM SUBSTRUCTURES										OPERATIONAL AND SOLUTION MODES						Size of Work Vector	CPU Time (Sec)
		BF1	BF2	BM1	FA1	IS1	RE2	RE3	CN1	GF1	MS1	GEN	PV1	EG1	EG2	FR1	TH1		
1	Inplane bifilars with 5 fuselage normal modes using a forced response solution with longitudinal and lateral excitation forces.	V								V	V					V		1855	0.8
2	Vertical bifilars with 5 fuselage normal modes using a forced response solution with a vertical excitation force.		V							V	V					V		2211	1.7
3	Elastic beam model comprising 5 segments constrained to vertical displacement using eigensolution 1.			V					V					V				7840	1.9
4	Fixed system absorber with mass added to base using a forced response solution with a longitudinal force at various frequencies.				V					V	V		V			V		1033	1.3
5	As Case 4 above using a time history solution calculated up to 1 second-line printer output suppressed.				V					V	V	V	X				V	1025	8.5
6	As Case 5 above using the time history restart option from 0.05 to 0.10 second-line printer output suppressed.				V					V	V	V	X				V	1124	0.9

NOTES: 1) V indicates substructures and solution method used.
2) X indicates operational modes and solution methods which cannot be used.

TABLE 6. - Continued

Case No.	Case Description	BASE PROGRAM SUBSTRUCTURES										OPERATIONAL AND SOLUTION MODES						Size of Work Vector	CPU Time (Sec)
		BF1	BF2	BM1	FA1	IS1	RE2	RE3	CN1	GF1	MS1	GEN	PV1	EG1	EG2	FR1	TH1		
7	One d.o.f. (Vertical Motion) nodal isolator with 2 fuselage and one transmission normal mode using a forced response solution with a vertical excitation force at various frequencies					V				V	V	V	V			V		3048	1.8
8	Two d.o.f. (Vertical and Lateral Motion) nodal isolator with one fuselage normal mode and one transmission normal mode with the vertical force applied to the transmission attachment.					V				V	V		V			V		2762	1.0
9	Two d.o.f. (Vertical and Lateral Motion) nodal isolation with one fuselage normal mode and one transmission normal mode with the vertical force applied above the transmission.					V				V	V		V			V		3058	1.0
10	As Case 9 above but with 6 normal modes for the fuselage and six normal modes for the transmission.					V				V	V		V			V		5883	2.5
11	Multi d.o.f. nodal isolator assembled from 4 isolator bars, positioned 90° to each other.					V				V	V		V			V		14824	15.3

NOTES: 1) V indicates substructures and solution method used.
2) X indicates operational modes and solution methods which cannot be used.

TABLE 6.- Continued

Case No.	Case Description	BASE PROGRAM SUBSTRUCTURES										OPERATIONAL AND SOLUTION MODES						Size of Work Vector	CPU Time (Sec)
		BF1	BF2	BM1	FA1	IS1	RE2	RE3	CN1	GF1	MS1	GEN	PV1	EG1	EG2	FR1	TH1		
12	E927 elastic rotor with 12 rotor coordinates and 5 fuselage modes using eigensolution 2.						V				V				V			14529	4.9
13	G400 elastic rotor impedance matrix with 6 hub displacements and 4 fuselage normal modes using forced response solution.							V		V	V	V	V	X	X	V	X	1836	2.5

NOTES: 1) V indicates substructures and solution method used.
2) X indicates operational modes and solution methods which cannot be used.

referred to the rotating system. The fixed system 4Ω forces result from rotating system forces with frequencies 3Ω and 5Ω referred to the rotating system. The rotating system forces applied by the rotor were found from measured bifilar arm accelerometer readings. Hub displacements were assumed to be negligible as a result of the bifilar having minimized the hub motions. The steady state forced response of the system was obtained from solution mode FR1. The coupled system solution has cosine and sine components (see equation (24)) and the bifilar arm displacements are therefore

$$\gamma_s = (\gamma_s)_c \cos 4\Omega t + (\gamma_s)_s \sin 4\Omega t, \text{ rad} \tag{99}$$

$$\gamma_c = (\gamma_c)_c \cos 4\Omega t + (\gamma_c)_s \sin 4\Omega t, \text{ rad} \tag{100}$$

Substitution of equations (99) and (100) in equation (74) yields

$$/\gamma/_{3\Omega} = \frac{1}{4} [[-(\gamma_s)_c) + (\gamma_c)_s]^2 + [(\gamma_s)_s + (\gamma_c)_c]^2]^{\frac{1}{2}}, \text{ rad} \tag{101}$$

For the bifilar mass 3Ω amplitude additional cases were run to find the bifilar mass amplitude variation with airspeed, shown in Figure 13. Results are compared with test data obtained from a bifilar mass mounted accelerometer. The agreement of theoretical results and test data shows the correctness of the substructure coupling procedure, the equations of motion for the components employed in the configuration, and the system properties determined from test data. The analytical model is not suitable for bifilar or fixed system design when rotor hub loads data are not available or at bifilar off-design conditions with large hub displacements when rotor impedance effects are important. A suitable general model for design studies would employ an aeroelastic rotor model, such as RE3.

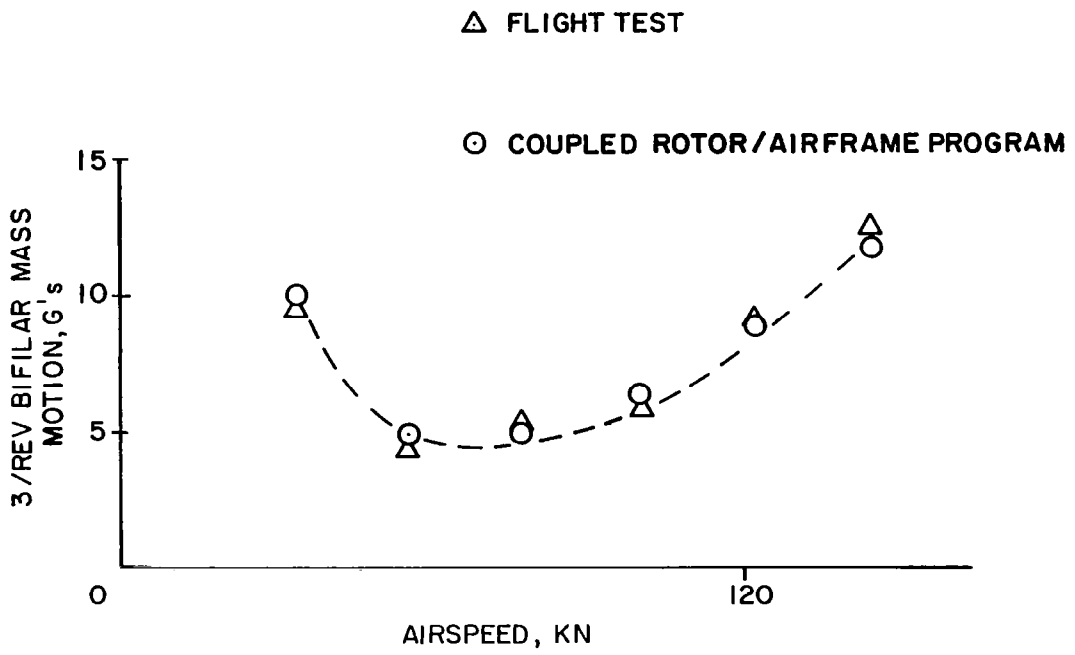

Figure 13. Bifilar Mass Amplitude Variation with Airspeed.

Case 2 is a verification of a vertical linear bifilar BF2. A vertical rotor induced force is applied to the hub. In other respects, the case is similar to Case 1.

Case 3 is a verification of beam model BM1, constraint component CN1, and eigensolution mode EG1. The case yields the mode shapes and frequencies for a five element uniform beam. The beam is constrained from motion in all directions except vertical translation. Figure 14 shows mode shapes and frequencies for a ten element beam model similar to Case 3. Results are in close agreement with classical results. The ten element beam case required approximately $15K_{10}$ decimal working storage words ($1K_{10}$ = 1024 words), which together with the storage required for instructions and common blocks ($17K_{10}$ decimal words) shows that this problem has approached the $32K_{10}$ decimal word limit for interactive CDC system usage (see Reference 17). The beam model BM1 could have been used with any solution mode. In particular, a forced response study with FR1 and rotor system RE3 could have been performed to study the vibration behavior of a helicopter preliminary design.

Case 4 is a verification of the fixed absorber FA1, with parameter variation mode PV1. A mass is attached to the base of the absorber by means of an MS1 component to simulate a two mass system joined by a spring and damper. An oscillating force is applied to the base of the absorber and a steady state forced response solution is obtained. The forcing frequency is specified to range between one and ten Hz. This parameter variation is achieved by means of input to PV1. Vibratory response results agree with analytical derivations. Analytical results were derived manually by application of the Laplace transform method to the assumed system.

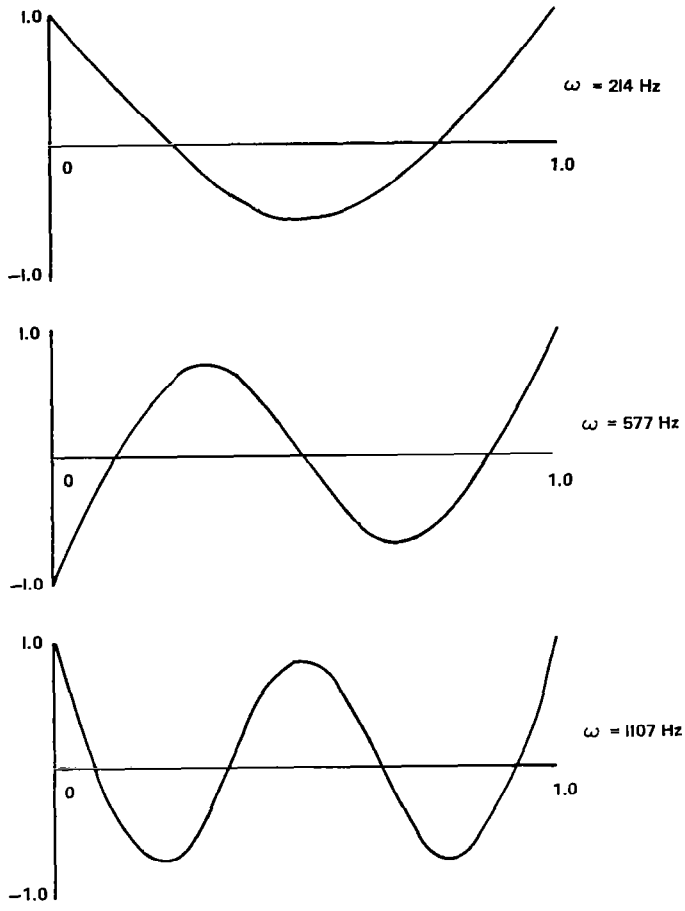

Figure 14. Normal Modes of a Ten Element Uniform Beam with Free Ends.

Case 5 is similar to Case 4 except that a time-history solution mode TH1 substitutes for steady-state forced response mode FR1 and parameter variation mode PV1. The case is also used to verify the general (GEN) control mode line printer output suppression capability. The case transmits data to a plot file and the Plot Package is used to plot results. Figure 15 illustrates the variation with time of the responses of the two masses. The steady-state values of vibratory response agree with the values obtained from Case 4, and with analytical derivation. A rigid body component of displacement of the two mass system shows a linear increase with time and agrees with analytical derivation.

Case 6 is the same as Case 5 except that it is used to check the restart option in the time-history solution mode. The case employs time-history restart data transmitted to a file from a prior time history run.

Case 7 consists of one nodal isolator of type IS1 coupled to upper and lower masses, connected by a spring such as shown in Figure 10. The isolator is free to move vertically. The frequency response of the system to a force applied to the isolator upper node is shown in Figure 16. The isolator capability to create a point of zero vibration at the lower attachment node is evident at the antiresonant frequency (27 Hz).

Cases 8 to 10 serve as a systematic synthesis and verification of features employed in a hypothetical six degree-of-freedom isolator model, Case 11.

Case 8 is similar to Case 7 in the character except that the isolator is free to move vertically and laterally. Two modal structures (MS1) were connected to the isolator at nodes one and two. A force of type GF1 was applied to node 1 of the isolator. The configuration is shown in Figure 17.

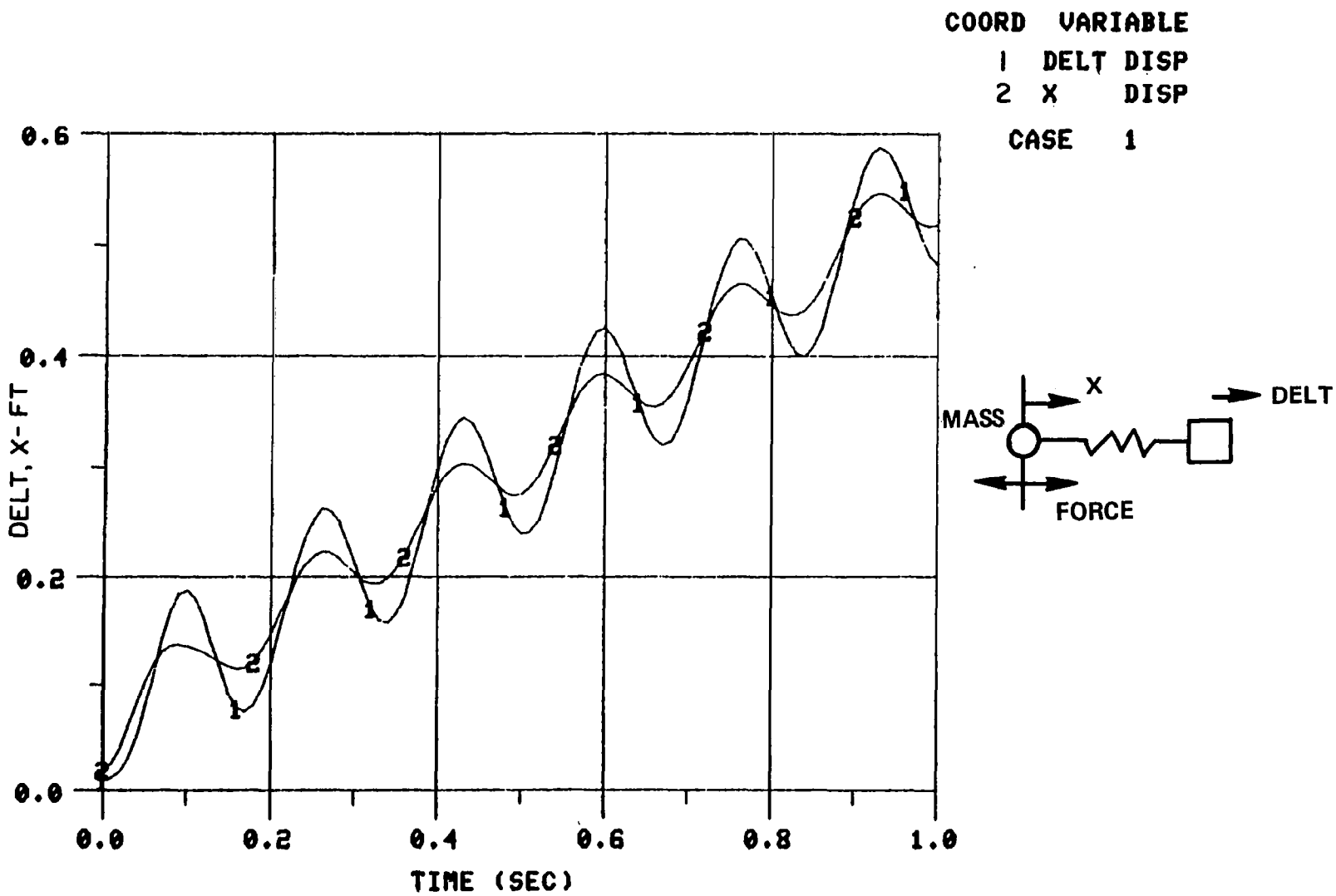

Figure 15. Variation with Time of the Displacment of a Two-mass System to which an Oscillating Force is Applied.

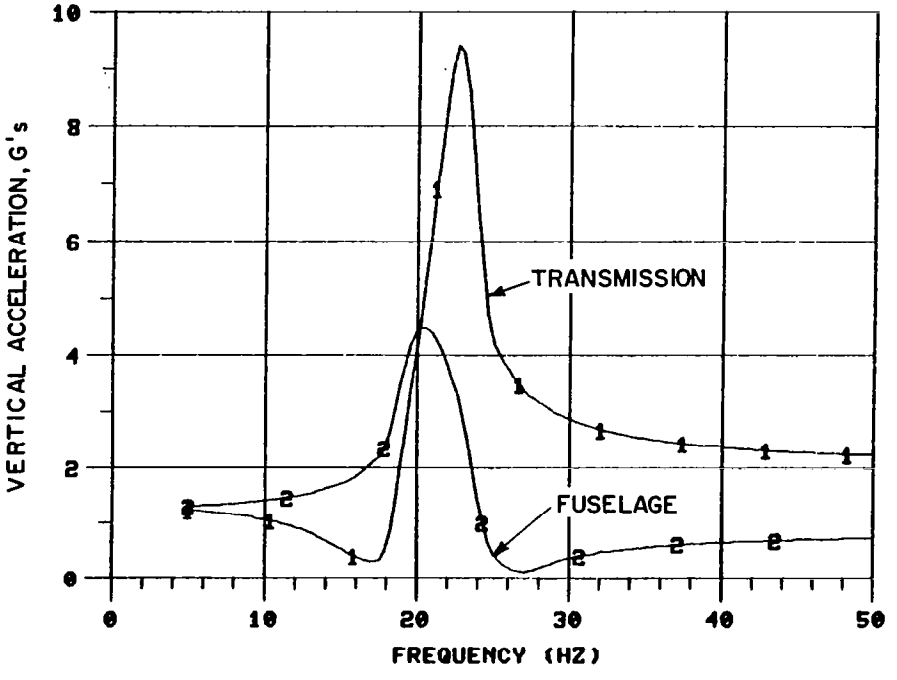

Figure 16. Frequency Response of a Simple Nodal Isolator.

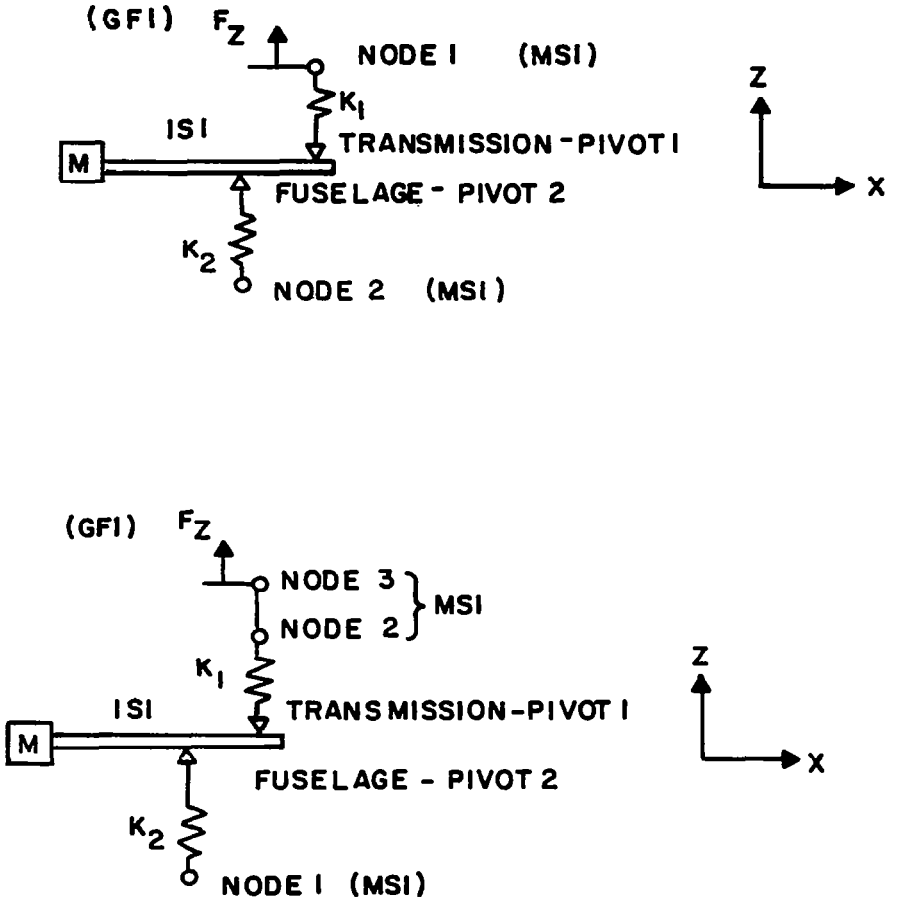

Figure 17. Configurations Used to Test IS1 Component.

Case 9 is similar to case 8 except that the GF1 force was applied to node 3 of an MS1 substructure (see Figure 17) which connects the force application point and the substructure attachment to the upper isolator node (node 2). The upper MS1 substructure simulates a transmission placed between a rotor and an isolator. The lower MS1 substructure simulates a fuselage.

Case 10 generalizes Case 9 to a configuration employing six modes for transmission representation, six modes for fuselage representation, and an isolator of type IS1. All the modes are rigid-body modes. A steady state forced response solution is obtained.

Case 11 consists of a six degree-of-freedom isolator constructed from four isolator bars of type IS1 connected at right angles to each other. Six rigid-body transmission modes, and six rigid-body fuselage modes are simulated. Six hub forces and moments are applied to the upper transmission to simulate the loading applied by a rotor. Isolator characteristics were derived from a half scale UH-60 isolator. An illustration of the model is shown in Figure 18. A total of nine connection nodes is used. This case introduces substructure Euler angles to check the correct formation of angular transformations from local to global axes. Bar Euler angles of 0, 90, 180 and 270 degrees are introduced. Figure 19 shows the frequency response of the isolator at a fuselage attachment. The variations with forcing frequency of three components of translation are shown at this point. Figure 20 is a three dimensional view of vertical displacements at the four fuselage attachments (see Reference 18 for plot types that can be requested).

Case 12 verifies the ability of the program to employ rotor aeroelastic model RE2 (E927 rotor). A five mode fixed system was coupled to the rotor. The rotor employs twelve coordinates consisting of flap collective, lead collective, two flap cyclic

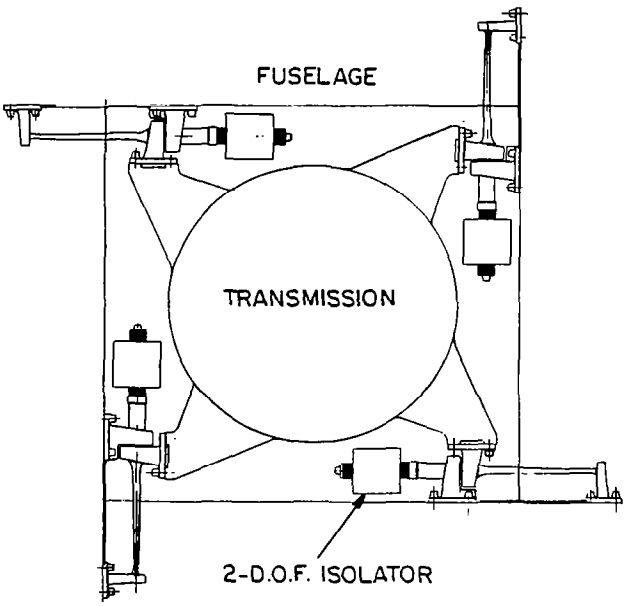

Figure 18. Six Degree-of-Freedom Isolator.

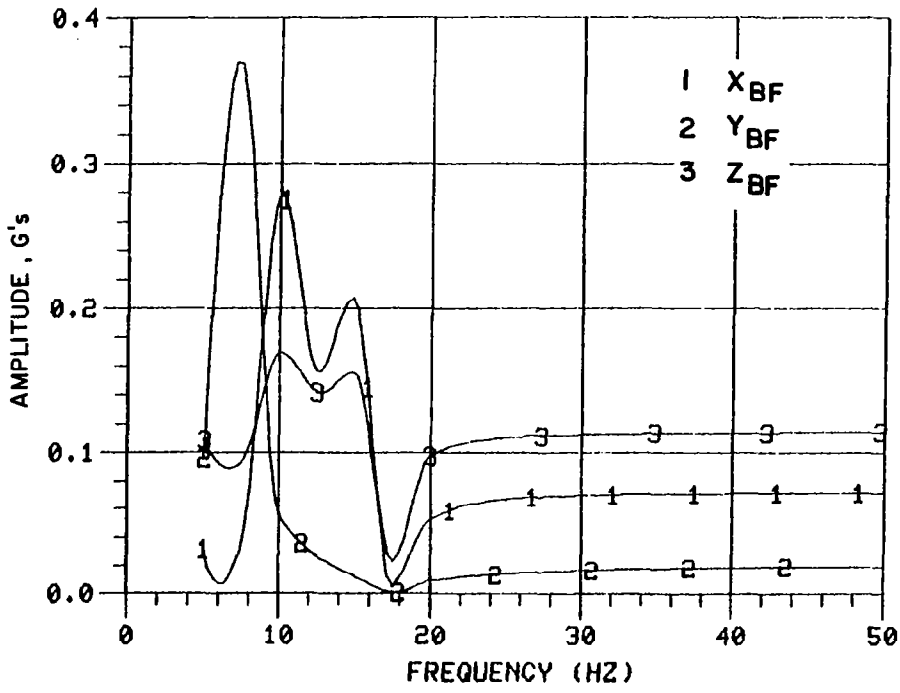

Figure 19. Frequency Response of Six Degree-of-Freedom Isolator at a Fuselage Attachment.

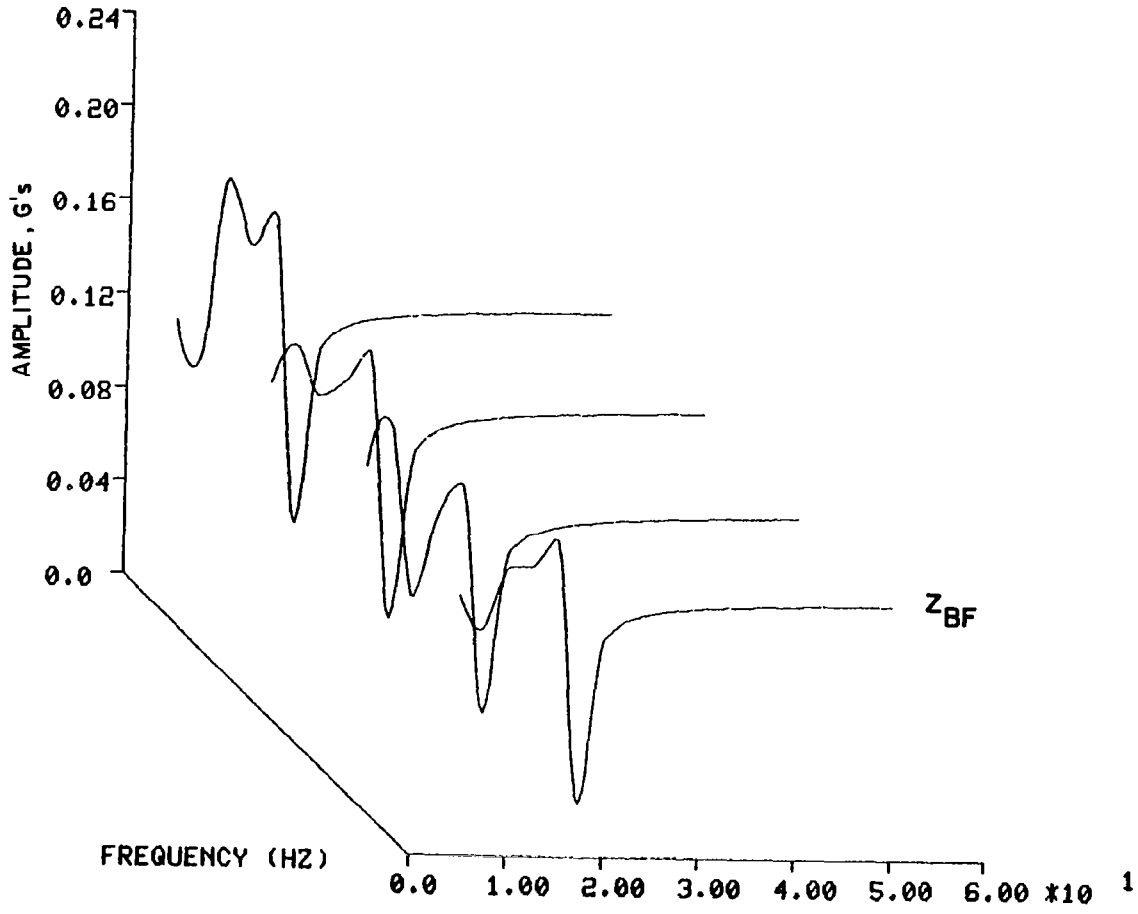

Figure 20. Six Degree-of-Freedom Isolator Vertical Responses at Fuselage Attachment Points.

modes, two lead cyclic modes, two bending collective modes, and four bending cyclic modes. An eigensolution of the system was obtained using the eigensolution mode with damping, EG2. Results agreed with results obtained from the unmodified E927 analysis, which included an elastic fuselage.

Case 13 verifies the ability of the program to employ rotor aeroelastic analysis RE3 and to serve as a tool to study efficiently the effects of variations in components internal to the Base Program. A rotor hub load excitation vector and a hub impedance matrix were transmitted by G400. A hypothetical full scale four blade rotor and four fixed system modes were specified. One flap, one lead, three uncoupled flatwise, two uncoupled edgewise, and one uncoupled torsion blade modes were used. Airspeed of 120 knots was specified, and uniform inflow was used. Figures 21 and 22 show the effects of changes in the frequency of the third fuselage mode on hub loads and accelerations, respectively (magnitudes of loads and accelerations should not be interpreted as being representative of an actual helicopter). Selected elements of the rotor impedance matrix were derived analytically and agreed with the G400 results. Verification of the ability of program package to derive and use rotor hub loads and impedances for rotors employing variable inflow is covered in the subsequent text. Case 13 verifies the END CASE command (see Reference 17). The first set of data in Case 13 employs a flag in RE3 to display the output solution vector in feet and the rotor hub interface forces (see equation (60)). The data following the END CASE command request the output to be displayed in units of acceleration of gravity (see equations (28) and (29)).

EXTERNAL PROGRAMS IN THE PROGRAM PACKAGE

Descriptions are given here of the functions and assumptions of the External Programs available in the Coupled Rotor/Airframe Vibration Analysis package.

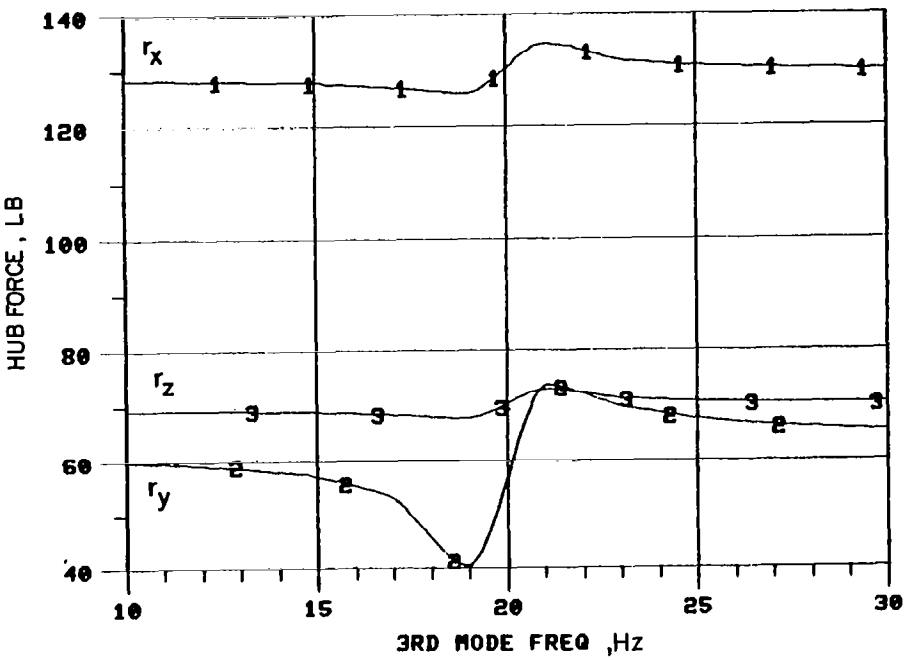

Figure 21. Effects on Rotor Hub Loads of Variations in Third Fixed System Mode Frequency.

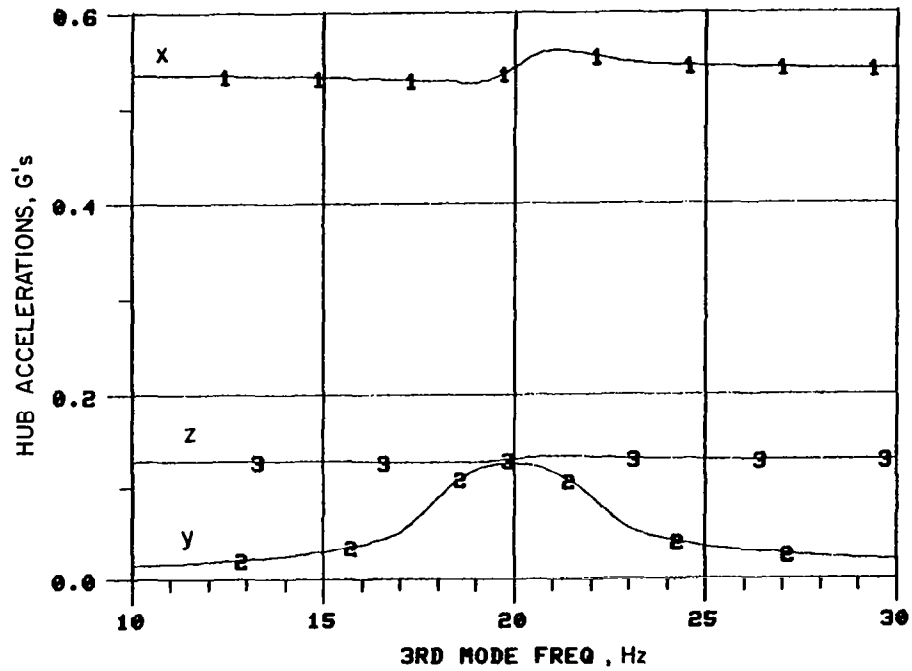

Figure 22. Effects on Rotor Hub Accelerations of Variations in Third Fixed System Mode Frequency.

Rotor Aeroelastic Analysis E927

The E927 Rotor Aeroelastic Stability Analysis (see Reference 6) is a linear analysis yielding dynamic, and aerodynamic mass, damping, and stiffness matrices of the rotor system in hover. These matrices are associated with perturbations of the coordinates of the rotor system. Coordinates comprise blade generalized displacements, both physical (e.g. flap angle) and modal. Five hub displacements are represented; lateral, longitudinal, and vertical translations, and hub pitch and roll. Linearization occurs about a rotor trim state. The trim vector is obtained from G400 or any other suitable analysis. Mass, damping, and stiffness matrices are transmitted to a file and read by the Base Program. These are assembled with matrices for other components selected. The Base Program eigensolution mode is used to evaluate the stability of the rotor system coupled to other components. Steady-state forced response may be calculated if a rotor hub force and moment excitation vector is input to the Base Program. Hub force and moment excitation data are obtained from the G400 analysis or any other suitable analysis.

Rotor Aeroelastic Analysis G400

The G400 Rotor Aeroelastic Analysis yields the time-history response of conventional articulated, teetering, and composite bearingless rotors. Options permit the use of variable rotor induced inflow, static blade aerodynamic data, and unsteady aerodynamic data. Blade mounted pendulum absorbers are modeled. Forward flight and hover are represented. The program calculates the hub excitation vector for a fixed hub, and the rotor impedance matrix relating six hub forces and moments to harmonic perturbations of the hub. These data are transmitted to a file which is read by the Base Program. The rotor hub excitation vector and the hub impedance are assembled with mass, damping, and stiffness

elements of internal components in the Base Program. The steady state forced response mode in the Base Program is invoked to obtain coupled system responses.

Rotor aeroelastic analysis G400 was created to overcome inadequacies of applications of conventional analyses to composite bearingless rotors. The analysis is based on a normal modes model of a non-linear rotor blade. References 8 and 9 describe the basis of the method. A coordinate transformation is applied to second derivatives of blade bending deflections as opposed to bending deflections. This transformation enables uncoupled normal modes to be used to achieve non-linear twist representations which satisfy the blade root and tip boundary conditions. Uncoupled modes derive from eigensolutions which employ uncoupled flatwise bending, edgewise bending, and torsion equations. Up to four flatwise, three edgewise, and three torsional elastic modes may be used. Blade articulation reduces the number of allowed modes. A Galerkin method yields modal differential equations which are integrated to obtain the time history response of the blade. Blade stress calculation options are mode deflection and external force integration methods (see Reference 10). Single blade loads are analyzed harmonically to obtain harmonics of rotor loads for a fixed hub. The hub is perturbed by specified harmonic motions and the resulting hub load perturbations are analyzed harmonically to obtain the rotor impedance matrix (see Assembly of Rotor Impedance Matrix). Control perturbations yield matrices required with the HHC solution mode (see Higher Harmonic Control for Vibration Reduction). Table 5 lists the capabilities of the G400 analysis. All rotor types are based on a single blade analysis, except for teetering rotors which are treated as two bladed rotors. Variable rotor induced inflow is introduced by executing sequentially G400 and the F389 Prescribed Wake Rotor Inflow Analysis. Refinement with variable inflow precedes calculation of the hub excitation vector and impedance matrix. The same interfacing of the Base Program and G400 occurs as in the uniform inflow case. Fuselage

induced inflow at the rotor disc is introduced by transferring harmonics of these data from WABAT to inflow program F389.

Prescribed Wake Rotor Inflow and Flow Field Analysis F389

Prescribed wake rotor inflow and flow field analysis F389 calculates the aerodynamic flow field induced by a rotor. The analysis may be used to calculate rotor induced velocities in the plane of the rotor or at user selected points - e.g., at the empennage.

The F389 analysis is based on a lifting line rotor blade representation. A vortex wake of prescribed shape is assumed to trail from the rotor blades. The assumption built into the program is that the wake form is a skewed helix (classical wake) as shown in Figure 23. The skew angle and distance between successive helixes is calculated by assuming the wake to be convected from the rotor by a uniform self-induced rotor inflow derived from momentum balance considerations, and from contributions from components of vehicle flight speed. The distance from the blade at which the trailing vortices roll up into a single tip vortex may be specified. The wake is terminated at a finite number of wake revolutions. The method of finding unknown circulations on blades and wake is described in Reference 12. The state of motion of the blades is assumed to be known. This state is derived from any suitable analysis external to F389.

The procedure consists of using the Kutta-Joukowski condition to derive a formula expressing blade circulation as the product of blade section lift curve slope, and blade section effective angle of attack. The effective angle is the geometric angle of attack corrected for inflow induced by rotor blades and wake. Circulation continuity (Helmholtz law) is used to express the circulation values in the trailing wake in terms of the circulations on the blades. A steady-state of flight is assumed, and as a result, the

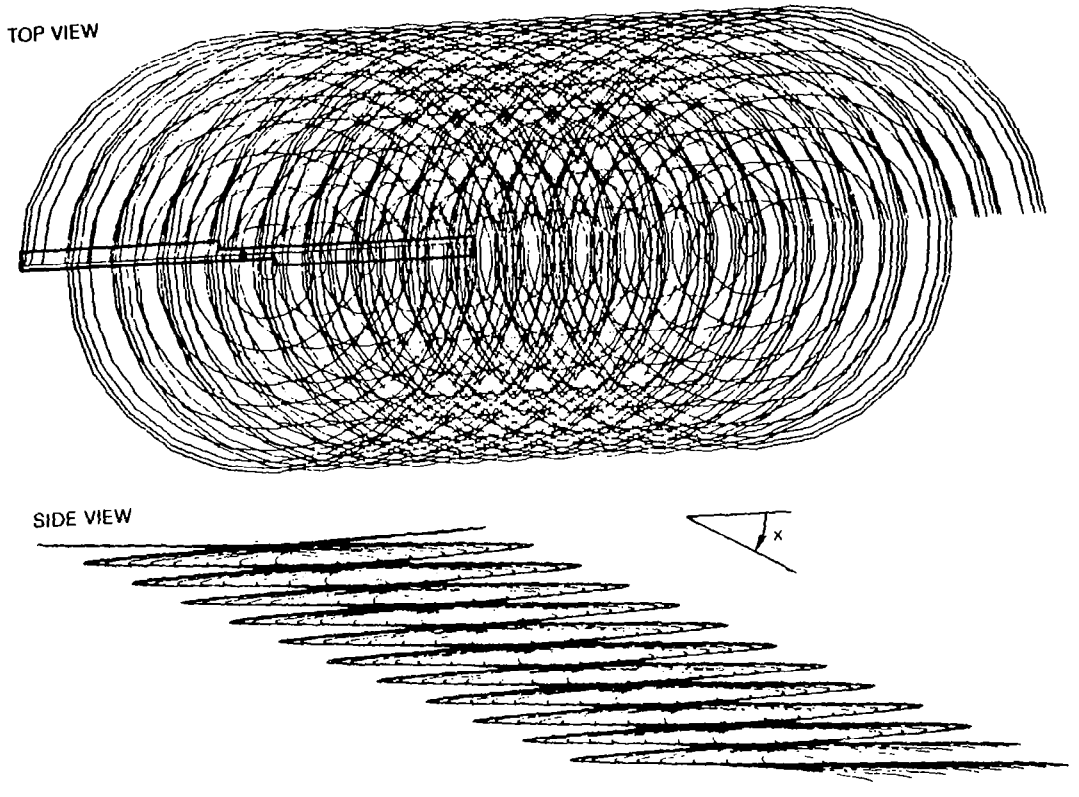

Figure 23. Computer Wake Representation-Undistorted Wake.

azimuthal variation of circulation is periodic. Flow velocities induced by blades and trailing vortex wake are found from the Biot-Savart law and contain circulation variables as unknowns. The induced velocity expressions are substituted in the formula for blade circulation to obtain a finite set of linear simultaneous equations which are solved for the unknown circulations.

After the circulations are known, induced velocities can be calculated anywhere in the flow field by application of the Biot Savart law.

Section airfoil lift coefficients are approximated by straight line curve fits to airfoil data, approximating unstalled and stalled regions of lift curves (see Figure 24).

The F389 program can be made to calculate the flow field consistent with the motions of an elastic blade. This is achieved by calculating the component of airflow normal to the median surface of the rotor blade induced by the motion of the elastic blade, which excludes the rotor induced flow contribution to the airflow. This airflow component is

$$w_1 = U_T\theta + U_p - \text{ROTOR INDUCED FLOW} \qquad (102)$$

The calculation of w_1 is performed in G400. The angle, θ, is the blade pitch angle. The variable, w_1, is automatically transmitted to F389 by G400. Program F389 adds the rotor induced inflow to w_1 to calculate the effective angle of attack of a blade section. Program F389 can represent an elastic rotor since no assumptions are made restricting U_T and U_p to non-elastic blades. It should be noted that another mode of F389 operation is to employ the flapping harmonics to define the blade motion input. This mode of calculation is less accurate than the mode employing w_1 because it omits elastic displacement contributions to airflow velocity components.

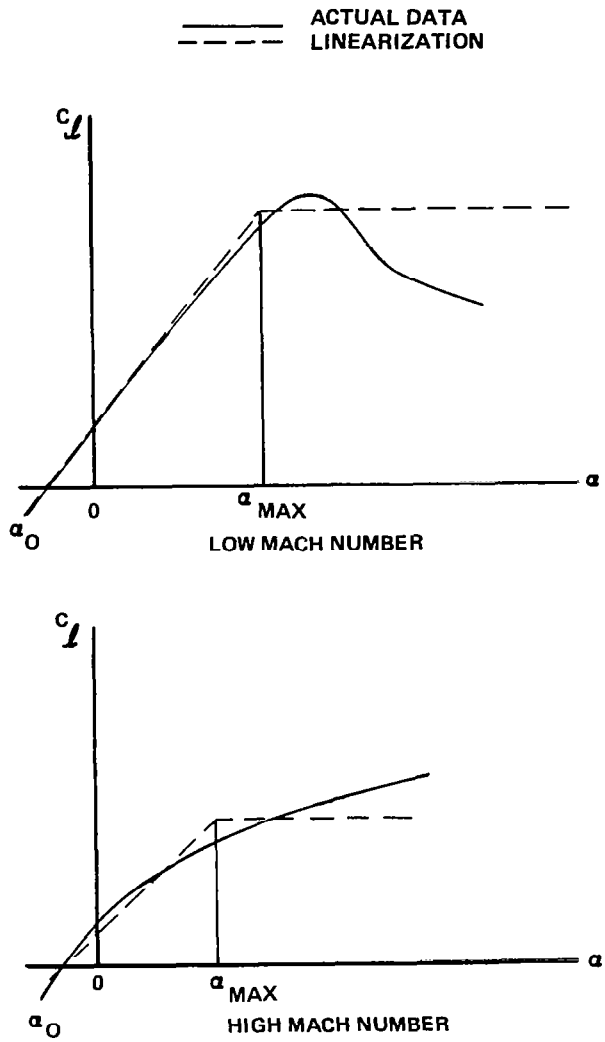

Figure 24. Approximations to Lift Curves in F389 Program.

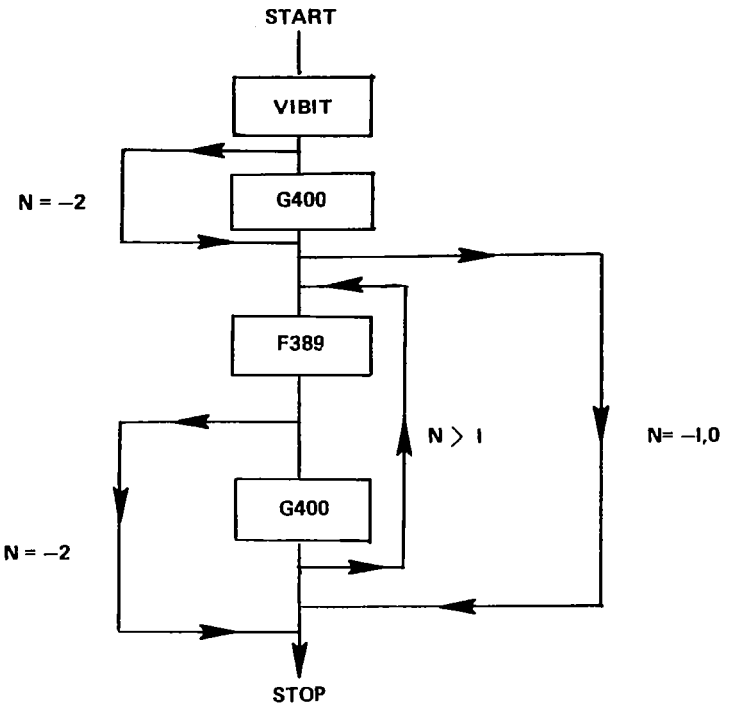

N (Execution Flag)	Execution Sequence
-2	F389 only
-1	G400 only
0	G400 only
1	G400/F389/G400 (one cycle)
2	G400/F389/G400/F389/G400 (2 cycles)

Figure 25. Calculation Sequences For The Coupled G400/F389 Programs

Determination of rotor induced flow requires a coupling of F389 and a rotor aeroelastic analysis. In the vibration analysis package, this is achieved by transmitting data automatically between F389 and G400. Data transmission and the invoking of F389 and G400 is controlled by a Fortran driver program, VIBIT. Driver program VIBIT causes G400 to be run first. Uniform rotor induced inflow is used. Program G400 transmits w_1 to F389 which calculates the rotor induced flow. The induced flow is transmitted by F389 to G400 which recalculates the blade aeroelastic response. The execution sequence G400/F389/G400 is referred to as one cycle of operation. An arbitrary number of cycles may be performed until the user is satisfied that consistency of blade circulations (lifts), blade motions, and aerodynamic velocities is achieved among the programs. Figure 25 illustrates the VIBIT/G400/F389 calculation sequences. After a converged solution is achieved calculations may be performed in the same run to obtain rotor output data - e.g., hub excitations and impedance.

The F389 program may be used to calculate rotor induced velocities at the empennage to provide data for the calculation of rotor wake induced empennage excitations by the RIEVA program (see Figure 1). The empennage flow field is assumed to have no effect on the rotor and no iterative calculations involving F389 and RIEVA are performed.

The F389 program accepts input defining velocities induced by a fuselage or gust. The velocity field is defined as harmonics of inflow at the rotor. Fuselage flow field data may derive from WABAT (see Figure 1). No change in fuselage velocities is assumed to occur as a result of the rotor wake influence on the fuselage.

Wing and Body Aerodynamic Technique (WABAT)

The Wing and Body Aerodynamic Technique (WABAT) is used to calculate a fuselage flow field. The flow velocities may be obtained

on the surface of the fuselage or at arbitrary (off-body) points. The velocity components in the plane of the rotor can be expressed as a harmonic series of blade azimuth angle whose coefficients depend on blade radius. The harmonic coefficients are transmitted to F389 to define the effects of fuselage induced flow at the rotor.

To obtain the solution to fuselage flow, the surface of the fuselage is divided into planar quadrilateral panels on which aerodynamic sources of constant strength are placed. The flow is assumed to be incompressible - i.e., the airspeed of the helicopter is assumed to be low. The sources satisfy the Laplace equation, which governs incompressible, inviscid (potential) flow. Strengths of the panel sources are determined from the condition that the flow normal to the fuselage is zero or that it is some specified value like that induced by an engine intake or exhaust. The number of solution points is specified to be equal to the number of sources of unknown strength. A set of linear simultaneous equations for the panel source strengths is obtained and solved. When the source strengths are found, the velocity field induced by the fuselage at any field point may be calculated by summing the contributions of the panels. Appendix B of Reference 13 gives further details of the method.

Lifting wings are represented by distributing horseshoe vortices (see Figure 26) in the mean surfaces of the wings and in the wing wake (trailing vortices). The solution technique for wing and body configurations consists of solving for the distribution of lift on the wing without the body. This lifting solution is achieved by means of a modified Multhropp analysis (see Appendix B Reference 13). The Multhropp lift distribution assigns circulation weighting factors among the horseshoe vortices. In other words, the relative strengths of the circulations among the horseshoe vortices distributed on a chord at each spanwise station are known. The magnitudes of the circulations are not known. As

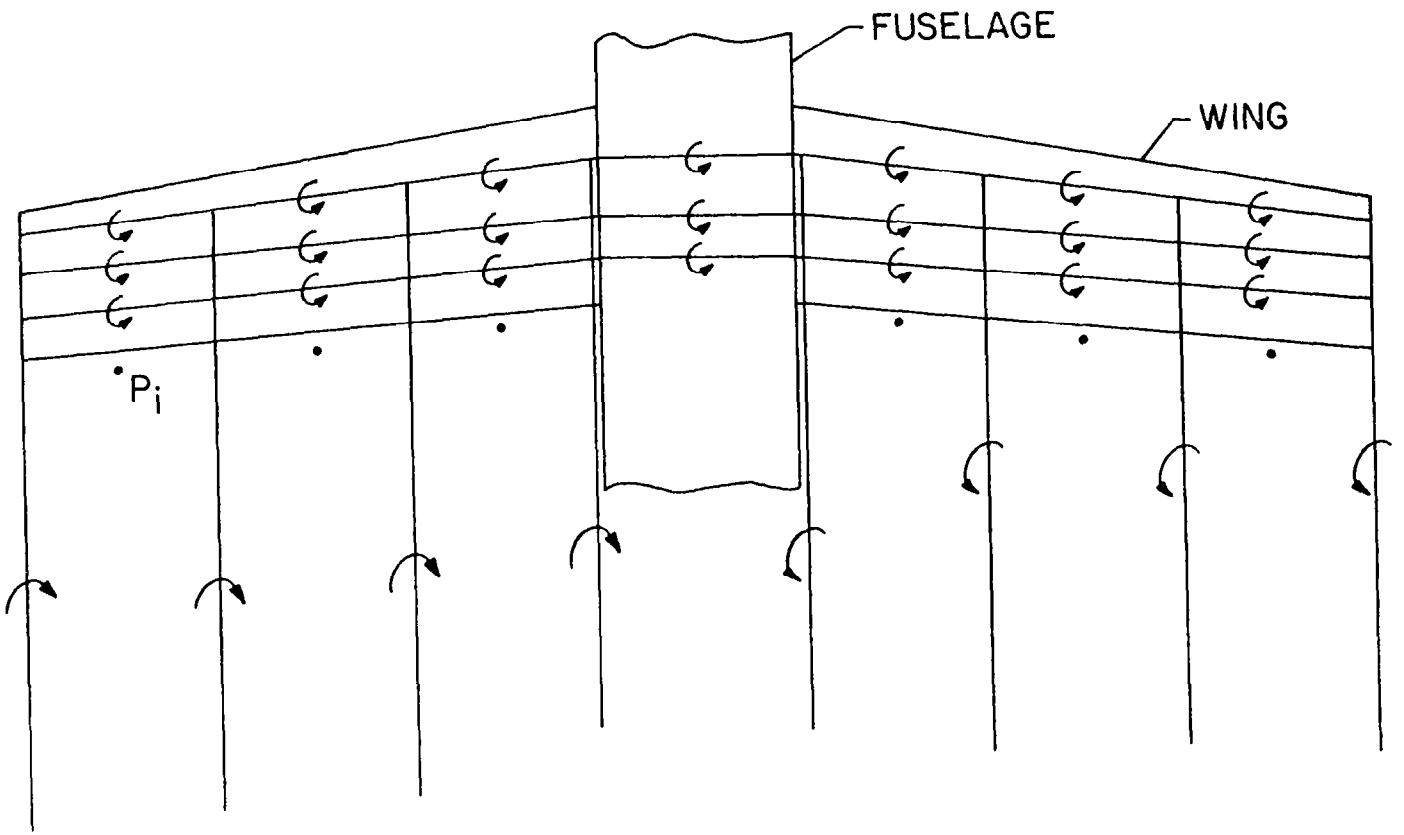

Figure 26. General Arrangement of Lifting Section Vortex Lattice Network.

a result of assignment of circulation weighting factors and a summing of the circulations on each chord, the circulation of each vortex can be expressed as some fraction of the total circulation at a spanwise station. The number of unknowns associated with the lifting wing at each spanwise station is therefore reduced to one, which is the total circulation at the station. The total number of lifting wing unknowns is N, where N is the number of spanwise stations on the wing. The determination of the circulation strength magnitudes is preceded by placing source panels on the wing to represent the thickness effects of the wing on the flow. The unknown circulations and source strengths are then obtained by summing the induced velocity effects of body and wing source panels and wing horseshoe vortices, and equating these velocities to specified velocities on the wing and body surfaces. When a wing is present, solution points are defined at each panel point on wing and body. In addition there are N solution points placed at the 3/4 chord of the aft-most horseshoe vortex at each spanwise station. The N additional points are introduced to increase the number of boundary conditions to accommodate the N additional unknowns (circulations) of the lifting wing. As a result, the number of unknowns and solution points are equal and the equations are solved for source and horseshoe vortex strengths. A wing and body solution satisfying the boundary conditions of the fuselage and wing is consistently obtained.

The synthesis of the fuselage geometry is facilitated by an automated technique of cross-section development from input data. Input data define a limited number of points on the cross section. This is performed by the Automated Paneling Technique (APT/Plot) program. Appendix A, Reference 13 describes the basis of the method. Incorporated in this program is a Tektronix plot capability which permits the user to verify the correctness of the panel input and transmits the panel data by means of a file to the WABAT potential flow program. The user may develop the fuselage geometry in subsections. Each section consists of a number of

panels. The Tektronix plot package assembles the sections into a complete fuselage and displays the resulting fuselage. The division of the fuselage into sections facilitates the development of the complete fuselage geometry. Parts of the fuselage - e.g., engine nacelles - requiring complex panel geometries may be developed and verified separately. The plot package is able to provide views of the fuselage from any angle and distance to permit the user to study and understand the data. Sections of the fuselage may be separated from each other to understand the data and character of the sections. Figures 27 to 29 illustrate views of the fuselage derived from the APT/Plot program. Reference 14 provides user instructions for the APT/Plot program.

Panel geometry data are transmitted by means of a file to the WABAT potential flow program (Figure 1) to calculate the wing and fuselage induced flow. The matrix of aerodynamic influence coefficients of the wing and body singularities (sources and vortices) may be saved on a file for subsequent applications. Employment of a stored influence coefficient matrix reduces the run time for subsequent cases using the same wing/fuselage geometry when attitude (angle-of-attack, sideslip) is varied. User instructions are provided in Reference 14. A secondary mode of the APT/Plot package may be invoked to obtain a fuselage surface flow display after the WABAT program has been run. The arrows in Figures 27 to 29 illustrate the flow directions of perturbational flows on fuselage panels.

Rotor Wake Induced Empennage Vibrations (RIEVA)

The Rotor Induced Empennage Vibration Airloads (RIEVA) program calculates the harmonics of empennage lift, rolling moment and pitching moment induced by a rotor wake at the blade passage frequency ($N\Omega$). These harmonic coefficients are input to the

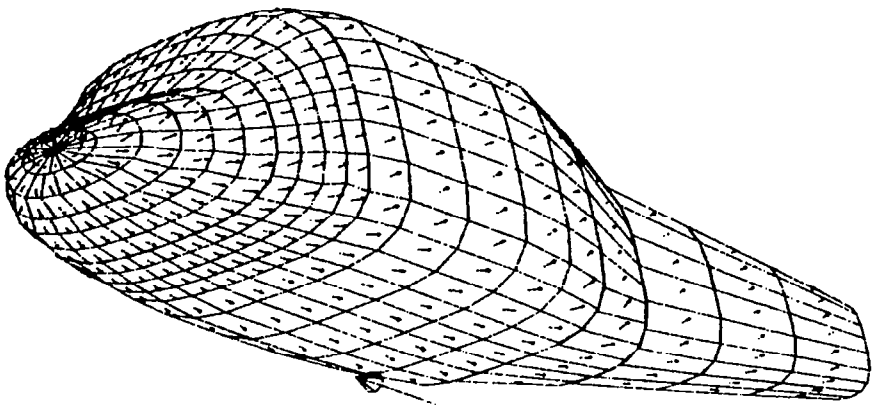

Figure 27. APT/Plot Program Fuselage View from Below.

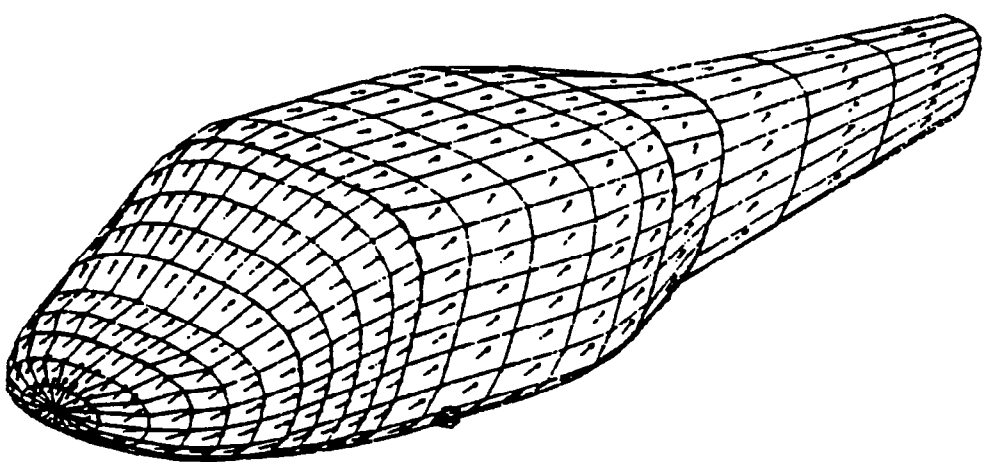

Figure 28. APT/Plot Program Fuselage View from Above.

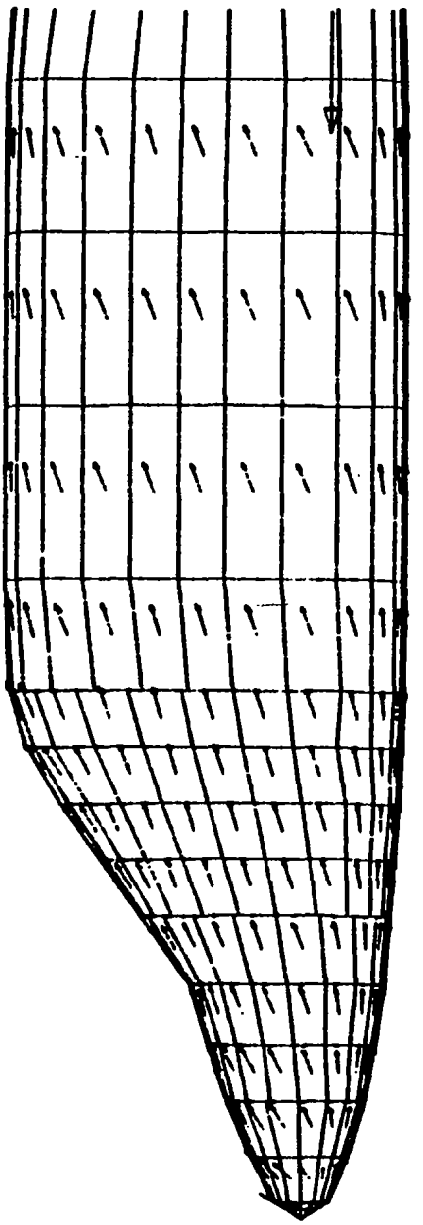

Figure 29. APT/Plot Program View Enlargement.

Coupled Rotor/Airframe Vibration Analysis Base Program to calculate the vibratory response of a helicopter to rotor wake excitations of the empennage. The steady state forced response mode in the Base Program is used to obtain a solution for the coupled system.

The empennage is represented as a three dimensional lifting surface of arbitrary shape. The empennage may include horizontal and vertical stabilizers. The flow is assumed to be incompressible and unsteady. The wing and its wake are represented by a doublet lattice on the mean surface of the wing and a vortex lattice on the wake. Figure 30 shows the lattice geometry. The perturbation velocities induced by the doublet and vortex lattices are calculated by the Biot-Savart law. At each instant of time the strengths of doublets and vortices must satisfy the boundary conditions of no flow normal to the wing surface, the Kutta condition of smooth flow from the trailing edge, and continuity relationships among the wake vortices and at the trailing edge interface between doublets and vortices. The distribution of circulations among the trailing vortices is known because vortices of known strengths are convected from the trailing edge at the speed of the flow. At the trailing edge there is an equivalence between the lifting surface doublet strengths and the strengths of the shed vortices. As a result of these relationships the number of unknowns reduces to the number of constant doublet panels on the empennage. These unknowns are assumed to satisfy as many simultaneous equations for normal velocities as there are boundary condition points specified on the empennage. The doublet strengths are obtained by simultaneously satisfying these equations at each time instant. The wake is assumed to begin at the calculation starting time. When doublet strengths are known empennage surface pressures may be calculated at each instant of time. The passage over the empennage of rotor vortices causes the flow over the empennage to be unsteady. When the empennage aerodynamic response is determined to be periodic at the blade

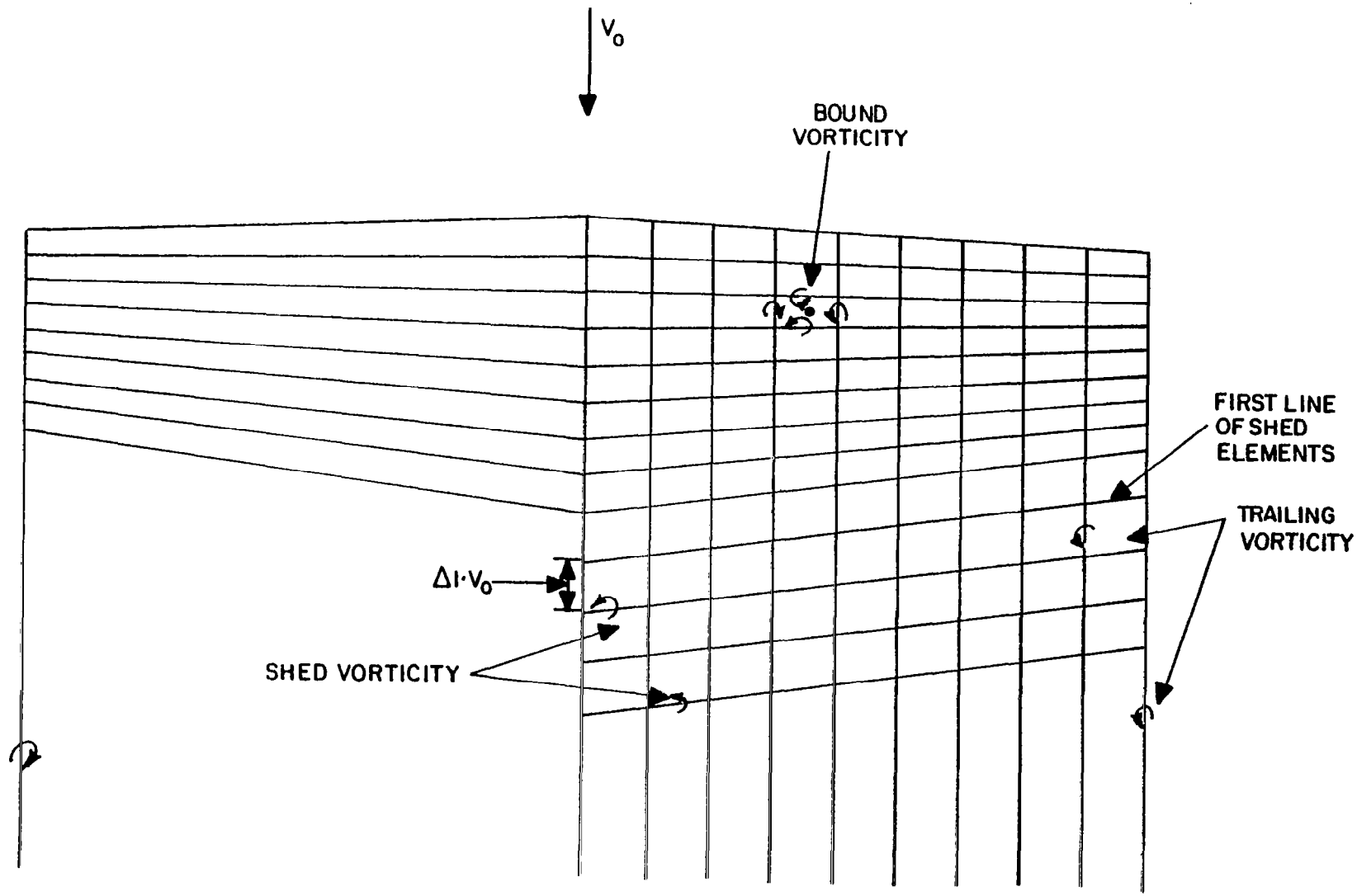

Figure 30. Empennage and Wake Lattice Geometry in RIEVA Analysis.

passage frequency (NΩ) the time-stepping calculation is terminated. Surface pressures are integrated to obtain empennage lift, pitching moment and rolling moments. These are harmonically analyzed at frequency NΩ. Vibratory response of a helicopter to rotor wake induced empennage excitations is obtained by input of these harmonics to the Base Program. Empennage loads are assumed to be applied to this fuselage junction.

Close passage of rotor induced vortices to the empennage is approximated by assuming surface pressures to be induced by Ran kine viscous vortices (see Reference 15). These consist of vortices with a solid core and a potential vortex region outside the core. The vortex is assumed to be more than one vortex core radius away from the lifting surface. If the vortex is closer than one core radius to the lifting surface, it is moved to a new position such as described in Reference 15.

The rotor induced wake is divided into a near wake region and a far wake region such as shown in Figure 31. The near wake region is contained by two vertical streamwise planes parallel to the flight direction, which also contain the empennage. The far wake is outside this region. The RIEVA program provides an internal calculation of the near wake from data defining the flight speed, tip path plane angle, position of the empennage, and rotor momentum induced flow. The far wake effects are represented as rotor induced flow velocity harmonics. These harmonics are obtained from F389 and are input into RIEVA. The user may elect not to input far wake harmonics if these effects are small. (Omission of far wake data simplifies RIEVA program usage, and has been found to be justified on the basis of applications made to this date.)

The following approximations are made in the present version of the RIEVA analysis. It is assumed first that the air pressures acting on the empennage are not influenced by the motion of the

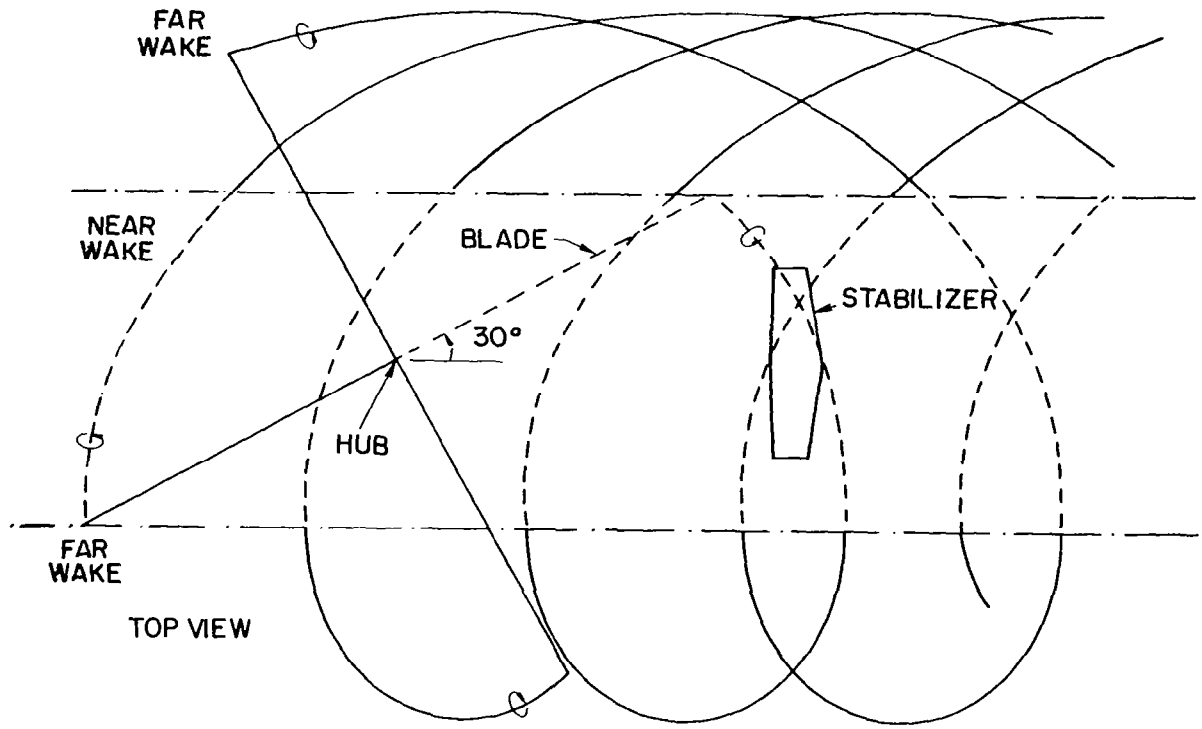

Figure 31. An Example of Splitting of Rotor Wake into Two Parts.

empennage. A second approximation is that the empennage displacement consists of plunge, pitch, and roll - i.e., the empennage is assumed to displace as a rigid body. The corresponding generalized forces acting on the empennage are lift, pitching moment, and rolling moment. These are assumed to act on the elastic structure at the empennage fuselage junction. When a modal representation of the fuselage is used it is necessary to define the components of modal displacement at this junction - e.g., plunge, pitch, and rolling elements of the modal matrix - to calculate the generalized forces induced by the empennage. Refinement of the calculation of generalized forces can be accomplished by multiplying empennage elastic mode shapes by the displayed values of pressures on the lifting surfaces to obtain generalized forces. The code does not provide this calculation.

The assumption that air pressures on the empennage are not influenced by motion of the empennage is equivalent to neglecting aerodynamic damping in plunge, pitch, and roll, and aerodynamic stiffness in pitch. These effects may be introduced as follows. Aerodynamically induced impedance elements can be calculated by employing an unsteady aerodynamic analysis. A simple approach would be to use Theodorsen unsteady aerodynamics (see Reference 16) and a strip theory assumption. Introduction of the empennage impedance matrix may be achieved by connecting a substructure of type RE3 to the point of application of empennage forces (see the subsection Rotor Aeroelastic Substructure RE3 and External Program G400 for use of RE3 as a general impedance substructure).

There are several alternative ways to representing the structural and inertial properties of the empennage. One method is to provide a modal representation. Fuselage modes would be determined with the empennage assumed to be present. An alternative approach is to calculate fuselage modes without the empennage. Empennage properties would be represented as contributions to the impedance matrix of substructure RE3, which are connected to the

fuselage at the empennage/fuselage junction. Impedance elements would also include aerodynamic contributions.

A third approximation in the analysis is that it does not include the contribution to the streamwise velocity component induced by vorticity shed from the rotor. This increment may be important when a rotor vortex passes near the vertical stabilizer. Components of rotor induced velocities normal to the lifting surfaces and perturbational streamwise components induced by the lifting surfaces are represented and are essential for obtaining the RIEVA solution.

Base Program Plot Package

The Base Program stores solution information on file for processing by the Base Program Plot Package. Line printer output produced by the Base Program may be suppressed optionally. The Plot Package is designed to recognize and display solution modes (forced response, time history, eigensolution) and coordinate labels without user intervention beyond identification of coordinate numbers selected for plotting. Comparative and perspective plots are options (see Reference 18).

EXTERNAL PROGRAM APPLICATIONS

Table 7 lists the check cases used to verify the capabilities of the External Programs. There are six external programs comprising the linked G400/F389, Tail Option (RIEVA), modified E927, Base Program plot package, WABAT geometry program/plot package (Automatic Paneling Technique/Plot or APT/Plot), and WABAT potential flow program. The check cases were selected to verify key capabilities, the abilities of the programs to transmit data to the Base Program and to each other, and to acquire data from the Base Program, such as plot data.

TABLE 7 - INPUT CHECK CASES FOR EXTERNAL PROGRAMS

External Program	Case Number	Case Description
G400/F389	1	G400 alone operation - baseline check case
G400/F389	2	G400 alone operation - blade-mounted pendulums option
G400-F389	3	G400 alone operation - higher harmonic control (HHC) and rotor impedance options (including trim)
G400/F389	4	G400 alone operation - teetering rotor and rotor impedance options (including trim)
G400/F389	5	F389 alone operation - field point induced velocity solution option - induced velocities output for RIEVA program
G400/F389	6	F389 alone operation - standard circulation solution option - induced velocities output for G400 program
G400/F389	7	Coupled G400/F389 program operation - 2 cycles option
RIEVA	1	Operation with far wake variable induced velocity field from F389 program
	2	Operation with far wake uniform induced velocity field
E927	1	Aeroelastic rotor in hover with 4 rotor degrees of freedom (12 rotor modes) and 5 hub degrees of freedom (see Table 6, Case 12)
Base Program Plot Package	1	Output file from Case 11, Table 6 - isolator model
APT/PLOT	1	Airframe buildup demonstration - nose cone + cylinder + reversed nose cone
APT/PLOT	2	Verification of panel geometry for a typical airframe
APT/PLOT	3	Graphical representation of airframe flow field (uses K/ABAT results as input)
WABAT	1	Typical input employing APT/PLOT (Case 2) file output - calculates harmonics of fuselage inflow at rotor

Coupled Rotor Aeroelastic Analysis and
Variable Inflow Analysis G400/F389

Case 1 verifies the ability of the G400 module to calculate an articulated rotor response. A full scale rotor of 22 foot radius was specified. Blade properties are typical of actual rotors. Uniform inflow was specified. This case uses specified input control angles - i.e., trim was not requested. Blade coordinates are flap, lead, three elastic flatwise, two edgewise, and one torsion uncoupled modes.

Case 2 is similar to Case 1, except the blade pendulum vibration absorbers are specified.

Case 3 is an application of G400 which is used to check the formation of the hub load excitation vector, rotor impedance matrix, matrix h_H containing the effects of input HHC angles on hub loads and blade stress matrices (see previous sections for descriptions of the above terms). The data are transmitted to a file. Base Program check case 13 (Table 6) uses the hub load excitation vector and rotor impedance data to calculate system response without HHC. Numerical rotor trim is requested, as opposed to analytic (Bailey derivative) trim (see Reference 9). Analytic trim was invoked for the HHC ARES model applications described subsequently. In other respects, the case is similar to Case 1.

Case 4 is similar to Case 3 except that a teetering rotor is specified.

Case 5 exercises the F389 program in a stand-alone mode. Inflow harmonics data are transmitted to a file which may be read by the Tail Option (RIEVA) module to represent the effects of the rotor induced far wake at the tail.

Case 6 exercises the F389 program in a stand-alone mode. Inflow harmonics data are transmitted to a file by F389 which may be read by G400, employed in a stand-alone mode.

Case 7 is a coupled G400/F389 run. Two cycles of calculation between G400 and F389 are performed - i.e., the execution sequence is G400/F389/G400, performed twice (see Figure 25). The rotor hub load excitation vector, rotor impedance matrix, and HHC matrix and stress matrices are not formed. The check of the formation of these matrices with variable inflow obtained from the coupled G400/F389 program is obtained in the ARES model application described subsequently.

Tail Option Program (RIEVA)

Case 1 verifies the calculation of harmonics of tail loads when rotor induced far wake data derive from a file to which inflow harmonics are transmitted by F389. Figure 32 shows the empennage airload variation with time.

Case 2 is similar to Case 1 except that the effects of the far wake are not included.

Rotor Aeroelastic Analysis E927

Case 1 has the rotor attributes described under Base Program check Case 12. Rotor M, C, and K matrices were transmitted to the Base Program.

Base Program Plot Package

Case 1 contains file data transmitted to a plot file by the Base Program. The file data were calculated for the six degree-of-freedom isolator system described as Base Program check Case 11. Figures 15, 16, 19, and 20 illustrate plots that may be obtained

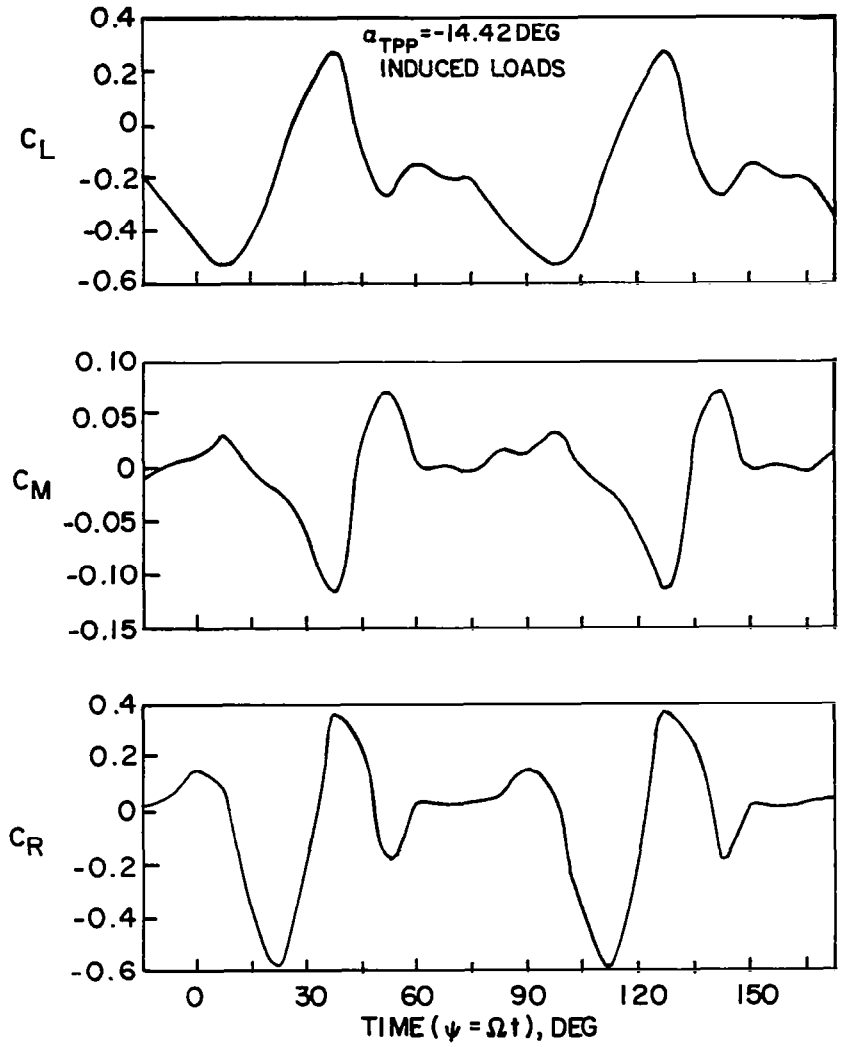

Figure 32. Stabilizer Airloads Time History in the RIEVA Analysis.

(see Reference 18 for plot variants).

WABAT Geometry/Plot Program (APT/Plot)

Case 1 checks the formation of panel geometry in the Automated Paneling Technique (APT/Plot) program from a hypothetical fuselage. The fuselage consists of three sections, each made up of several panels. The sections consist of a nose cone, center section cylinder, and reversed nose cone, which completes the fuselage. The APT/Plot program assembles the three sections into a body resembling a fuselage. The resulting geometry data are stored for input to the WABAT potential flow program or the plot module of APT/Plot.

Case 2 employs stored geometry data to check the plot module of the APT/plot program. The plot file data contain panel geometry data for a typical fuselage. Plotted results are shown in Figures 27 to 29. The results show the capability of the program to permit viewing of the geometry from any perspective, and the capability of the program to magnify regions of interest.

Case 3 employs WABAT potential flow calculations to display flow directions (arrows in Figures 27 to 29) on the surfaces of fuselage panels. It was necessary to run the WABAT potential flow module prior to obtaining the fuselage flow plots. The case illustrates the surface flow plotting function of the APT/Plot package.

WABAT Potential Flow Program

Case 1 uses APT/Plot file data to obtain the potential flow solution for the fuselage shown in Figures 27 to 29. Harmonics of fuselage inflow at the rotor are calculated and can be transmitted to F389.

USER DOCUMENTATION

The following section lists the documents which must be used to apply the programs contained in the Coupled Rotor/Airframe Vibration Analysis package. A brief description is given of the purpose and contents of the documents.

1. Cassarino, S.and Sopher, R.: Coupled Rotor/Airframe Vibration Analysis Program Manual. Volume I. User's and Programmer's Instructions NASA CR-165891, 1982.

The manual contains user instructions for the Base Program describing input preparation and output interpretation. Input/output files are described for transmitting data to External Programs. Program structure and subroutine functions are described. Appendixes describe the structure, file functions, and usage of the coupled G400/F389 program, and the E927 program. Descriptions are given of procedures for modifying the Base Program. Sample test cases are listed and described.

2. Volume 2 of the above contains line printer input and output samples for the Base Program, and coupled G400/F389 and E927 programs.

3. Bielawa, Richard, L.: Aeroelastic Analysis for Helicopter Rotors with Blade Appended Pendulum Vibration Absorbers - Mathematical Derivations and Program User's Manual. NASA CR-165896,1982.

The mathematical basis of modifications to the G400 analysis comprising teetering rotor and pendulum absorber modifications and the method used to calculate the rotor impedance are described. The complete mathematical basis of the analysis prior to modifications is described in Reference 8 listed also as item 4 below. Program hierarchy and subroutine functions are described. Input

preparation is described.

4. Bielawa, R. L.: Aeroelastic Analysis for Helicopter Rotor Blades with Time-Variable, Nonlinear Structural Twist and Multiple Structural Redundancy - Mathematical Derivation and Program User's Manual. NASA CR-2638, 1976.

5. Egolf, T. A., and Landgrebe, A. J.: A Prescribed Wake Rotor Inflow and Flow Field Prediction Analysis. NASA CR-165894, 1982.

This manual describes the mathematical basis of the rotor induced variable inflow analysis, F389, functions of program subroutines, and input preparation. The analysis is a single rotor version of the analysis listed below as item 6, which provides further details of the mathematical basis of the method.

6. Landgrebe, A. J., and Egolf, T. A.: Rotorcraft Wake Analysis for Prediction of Induced Velocities. USAAMRDL TR 75-45, 1976.

7. Cassarino, Sebastian, J., and Mouzakis, Timoleon: Bifilar Analysis User's Manual - Volume II. NASA CR-159228, 1980.

The manual describes input preparation, program structure, and functions of subroutines of the E927 program including a bifilar vibration absorber. Modifications were made to the bifilar version of E927 program for the present contract to eliminate the bifilar capability and to configure the E927 rotor as a substructure for use by the Base Program. Appendix B of item 1 above describes changes users must make to E927 input to employ the modified program and specifies the file for transmitting data to the Base Program. Sample inputs and outputs are provided in item 1 above. The mathematical basis of rotor aeroelastic analysis E927 is described in Reference 6, listed as item 8 below.

8. Johnston, R. A., and Cassarino, S. J.; Helicopter Rotor Stability Analysis, USAAMRDL TR-75-40, U.S. Army, January 1976.

9. Gangwani, Santu T.: A Doublet Lattice Method for the Determination of Rotor Induced Empennage Vibration Airloads - Analysis Description and Program Documentation. NASA CR-165893, 1982.

The manual describes the basis, program structure, subroutine functions, and input preparation for use of the Rotor Induced Empennage Vibration Airloads (RIEVA) program. Applications are described and discussed. The file for accepting variable inflow data from the F389 program is specified in item 1 above.

10. Studwell, R. E.: User's Manual for the Coupled Rotor/Fuselage Vibration Analysis Graphics Package. NASA CR-165897, 1982.

The manual describes the user responses to plot package messages for plotting results transmitted by the Base Program. Plot option results are illustrated. Program function and subroutine structure are described. The plot data transmission file format is specified in the text of item 1 above.

11. Studwell, R. E.: User's Manual for the Automated Paneling Technique (APT) and the Wing Body Aerodynamic Technique (WABAT) Programs. NASA CR-165895, 1982.

This manual describes the preparation of input for the WABAT geometry package (APT/Plot) and the WABAT potential flow program. The manual describes the user responses to plot fuselage geometry and fuselage surface flows. Sample problems are illustrated. Input data requirements for the geometry package (APT/Plot) are described. The basis of the automated paneling technique is

described in Appendix A of Reference 13 (see item 12 below). The potential flow analysis basis is summarized in Appendix B of Reference 13 (see item 12 below).

12. Sheehy, T. W.: A Method for Predicting Helicopter Hub Drag. (USAAMRDL Contract DAAJ02-74-C-0050.) USAAMRDL-TR-75-48, 1975.

CORRELATION OF THEORY AND TEST

In addition to development of the Coupled Rotor/Airframe Vibration Analysis, this contractual effort included a limited correlation study. The correlation study involved using wind tunnel data from a dynamically scaled UH-60A rotor system coupled with the NASA Langley aeroelastic rotor experimental system (ARES) powered test stand. Tests were conducted with and without higher harmonic control (HHC) employed. Model balance loads, rotor bending moments and vibrations in the ARES structure were measured. A shake test was performed to obtain the modal attributes of the system for input to the Coupled Rotor/Airframe Vibration Analysis.

Shake Test of the ARES Model

A shake test was conducted in the NASA Langley Transonic Dynamics Tunnel (TDT) to determine the support system modal properties required for vibration analysis predictions. The support system was provided by the Langley Research Center Aeroelastic Rotor Experimental System (ARES) (see Reference 19). The test procedure consisted of exciting the model by an electromagnetic shaker in several different directions. Random excitations were applied to the model. Data were recorded on 14 track FM magnetic tapes and consisted of outputs from eight hub accelerometers, three body accelerometers, six rotor balance channels, and the force load cell.

The shake test data were processed using a dual channel digital analyzer (HP 5420) to obtain transfer functions - e.g. acceleration/applied force harmonics - of the measurements with respect to the applied forces. The ARES modal attributes presented in this section and those used in the correlation study are based on the random excitations. Table 8 lists the characteristics of nine ARES modes covering a frequency range from 21 to 73 Hz. The frequencies of interest are located near 45 Hz which is 4/rev. for the four bladed model rotor. The natural frequency, generalized mass, percent critical damping, six-component mode shape at the hub, and three translational components of modal response at the airframe accelerometer location for each mode are listed in Table 8.

Modes 1, 2, 3, 7, 8 and 9 were obtained from a vertical off center excitation of the hub. A centered lateral excitation run defined the properties for modes 4 and 5. A centered longitudinal excitation run defined mode 6. The generalized masses for each of these nine modes were determined from single degree of freedom analytical models of the system. The damping in each mode was obtained by peak fit using the HP 5420. Imaginary components of the transfer functions were used to define the mode shapes at the rotor hub and airframe.

Wind Tunnel Test Program

The test program was conducted in the NASA Langley Transonic Dynamic Tunnel (TDT). The model rotor was installed on the Langley Research Center Aeroelastic Rotor Experimental System (ARES), Reference 19. Figure 33 shows the ARES model with the test rotor.

A four-bladed articulated rotor (1/6 scale) was installed on the ARES model. The dynamically scaled blades were based on UH-60A blades. The same blades were used for baseline studies in

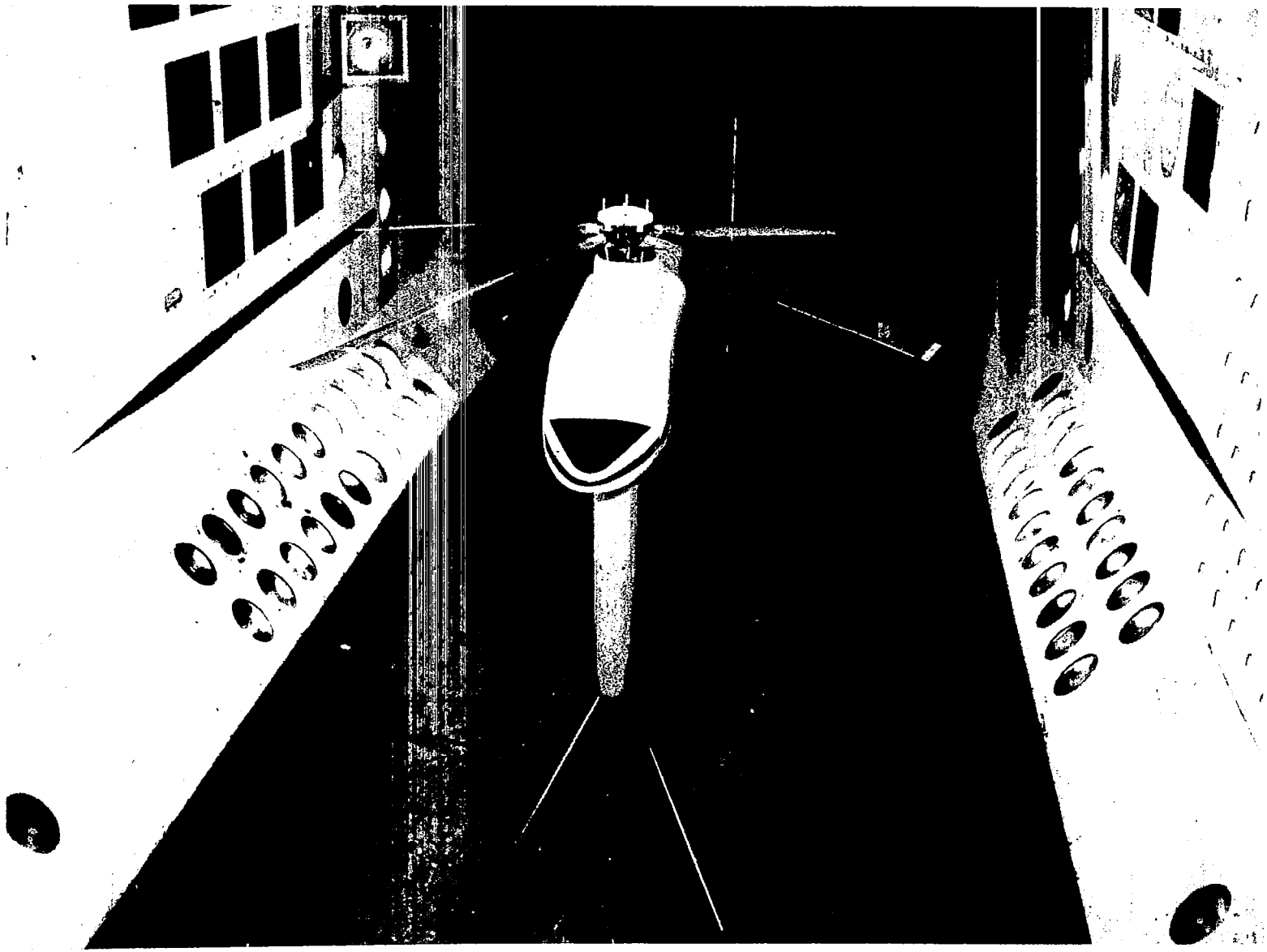

Figure 33. ARES Model in NASA Langley Transonic Dynamics Tunnel with Model Test Blades.

TABLE 8 - ARES AIRFRAME MODAL ATTRIBUTES

MODE SHAPES

No.	Freq. Hz	Mass lb-sec² in	Damp %	HUB Long. in/in	Lat. in/in	Vert. in/in	Roll rad/in	Pitch rad/in	Yaw rad/in	AIRFRAME Long. in/in	Lat. in/in	Vert. in/in
1.	21.1	32.54	12.2	-3.35	0.82	-3.86	-0.03	-0.29	0.03	0.05	-1.04	2.38
2.	25.4	115.38	2.0	4.40	-0.26	-1.61	-0.09	0.16	-0.05	0.64	.26	-231.06
3.	28.2	132.71	4.5	13.07	0.72	-3.13	-0.23	0.83	0.04	0.85	1.82	96.79
4.	37.5	2536.24	7.9	-1.92	-154.84	0.24	10.74	1.59	-1.64	0.57	-38.56	10.26
5.	48.8	2975.02	6.6	1.66	-151.74	-2.40	14.14	1.87	-0.38	2.83	28.22	-2.69
6.	57.8	7418.32	5.6	-321.04	21.15	-1.68	4.31	-36.17	1.94	17.51	8.68	20.58
7.	62.0	1306.88	1.9	70.72	-10.09	-2.36	-0.20	7.00	-1.23	2.95	1.93	4.58
8.	66.0	971.74	4.2	120.42	-21.49	3.68	-.15	14.08	-1.39	-7.46	10.38	4.31
9.	72.7	1428.70	1.5	54.06	-4.87	-0.82	-1.07	7.43	-2.79	-40.54	-3.89	-49.30

Reference 20 which contains details of the blade properties. The blades were scaled for operation at full-scale Mach numbers in Freon. Model Reynolds numbers were 40 percent of full-scale values. The blades have a 56.22-inch radius, a 3.625 inch chord, and a -12 degree twist. The blades have an SC1095 airfoil section inboard of the 50 percent and outboard of the 85-percent radius stations. The SC1095R8 airfoil is used between the 50- and 85-percent span stations.

To achieve vibration reductions with HHC, various types of higher harmonic controllers were tested. The control algorithms are described in References 11 and 21. Comparisons of theoretical predictions obtained with the Coupled Rotor/Airframe Vibration Analysis were made with test data for the adaptive closed-loop controller listed as controller 2 in Table 1 of Reference 21. In this controller, the T matrix was identified and updated on-line and "cautious" terms were provided (see Reference 21).

Application of the Analysis

The Base Program was applied in its forced response solution mode, FR1. The forcing frequency used in this solution mode for the present application was 44.7 Hz which is the 4/rev. frequency for the four bladed rotor model at its operating speed of 670 RPM.

Rotor Representation. The rotor effects were represented by substructure RE3 which models a multibladed aeroelastic rotor in forward flight or hover. This component reads the rotor hub excitation force and moment vector and the rotor impedance matrix and HHC and blade stress matrices computed by rotor aeroelastic analysis G400. In this application G400 was executed iteratively with External Program F389 to account for rotor induced variable inflow. The iterative sequence was G400-F389-G400 - i.e., one coupled cycle of these programs was run (see Figure 25).

The rotor was analytically trimmed to achieve the test values of lift and shaft angles for advance ratios from 0.20 to 0.40. Blade properties were taken from Reference 20. The resulting blade frequencies are listed in Table 9. Two flatwise, one edgewise, and one torsion mode(s) were employed in the computations. Full-scale Reynolds number data for the SC1095 and SC 1095R8 airfoils were used in rotor aeroelastic analysis G400. The thrust coefficient C_T/σ was equal to 0.07 for all cases.

Rotor Impedance Sensitivity to Perturbation Amplitudes. - External Program G400 obtains the rotor impedances with respect to hub motions and HHC angles. The perturbation amplitudes were selected to achieve accurate values of the numerically obtained impedance elements. Applications showed that there was a practical limit on the size of the perturbation amplitudes for accurate results. Accurate results were verified by comparisons of G400 numerical results with analytically derived results for rotor impedance and HHC control matrix elements.

Figures 34 and 35 show sensitivity of the $z_{11}(1,1)$ and $h_{11H}(3,3)$ elements of the rotor impedance and h_H matrices to perturbation amplitude. Based on these figures, the perturbation amplitudes selected were 152 m/sec^2 (500 ft/sec^2) for hub linear acceleration, 50 rad/sec^2 for hub angular acceleration, and 0.10 degree for HHC angles.

Support System Representation. - The ARES modal attributes listed in Table 8 were incorporated into the analysis by the use of modal substructure MS1. Each ARES mode was represented by one MS1 substructure. The connection point between the rotor hub and support system was defined as the first node. The airframe location where vibrations were measured was taken as the second node. The airframe node required the use of a generalized force GF1 type of substructure.

TABLE 9 - CALCULATED BLADE NATURAL FREQUENCIES FOR THE MODEL ROTOR (PER REV)

Mode No.	1	2	3
Flatwise	2.7	4.7	7.7
Edgewise	5.0	14.2	
Torsion	6.0	14.9	

TABLE 10 - COMPARISON OF ARES AIRFRAME AND MODEL ROTOR BLADE NATURAL FREQUENCIES

ARES SHAKE TEST DATA (REFERRED TO FIXED SYSTEM)

No.	Description	ω/Ω
1	-	1.9
2	-	2.3
3	-	2.5
4	Lateral Roll	3.4
5	Lateral Roll	4.4
6	Longitudinal Pitch	5.2
7	-	5.6
8	-	5.9
9	-	6.5

3 Mode Solution

CALCULATED BLADE MODES (REFERRED TO MOVING SYSTEM)

Description	ω/Ω
Flatwise 1	2.7
Flatwise 2	4.7
Edgewise 1	5.0

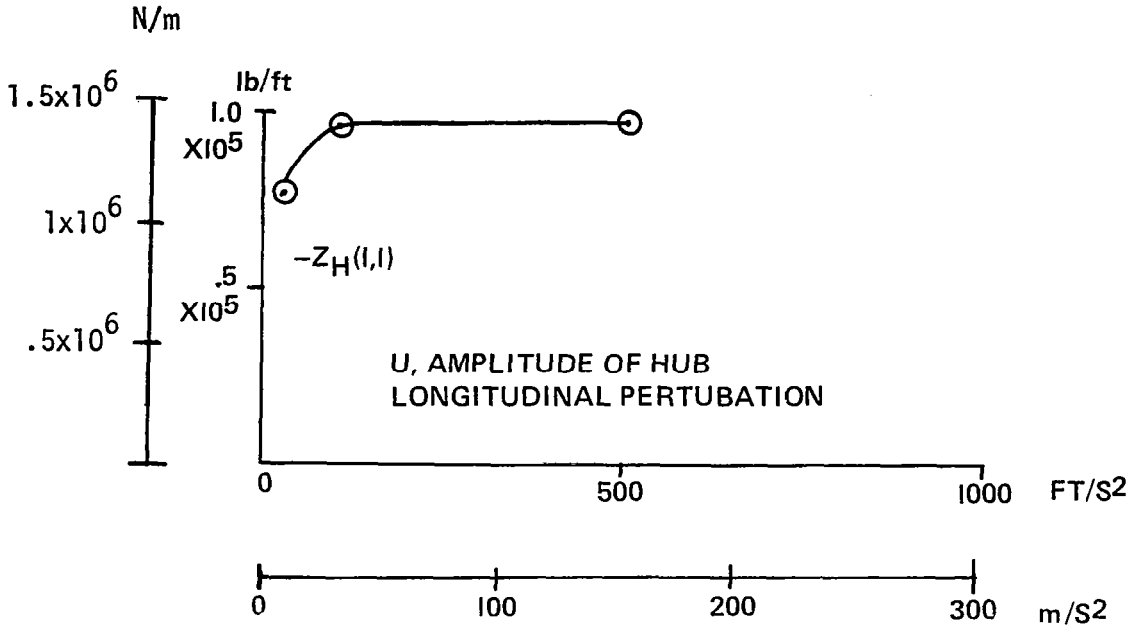

Figure 34. Sensitivity of Rotor Impedance to Hub Perturbation Amplitude.

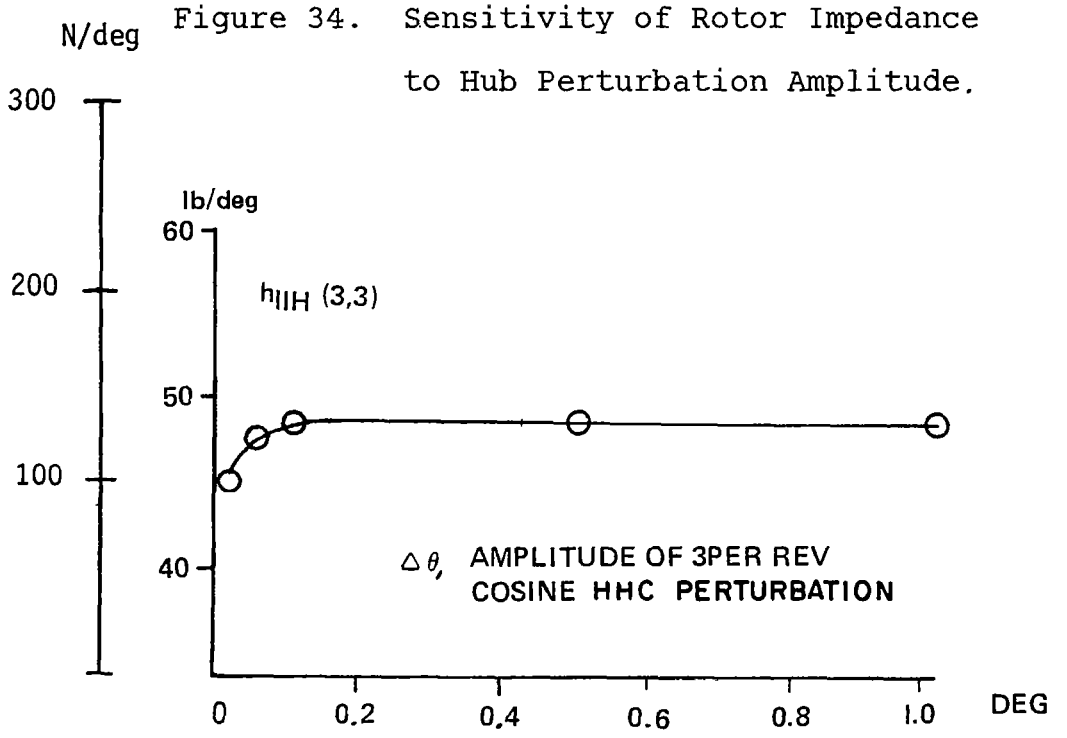

Figure 35. Sensitivity of h_H Matrix to HHC Perturbation Amplitude.

Specified Higher Harmonic Control. - Four values of pitch amplitude were specified to determine the effects of non-optimal control angle inputs on vibrations and loads. These four cases were obtained by specifying θ_{3C} = + 1°, and -1°, and θ_{3S} = + 1°, and -1°. These specified inputs are non-optimal because they are not determined from the requirement that they must minimize vibrations.

Optimal Higher Harmonic Control. - The analytical optimal control state is derived from equation (93), which is essentially the same as the algorithm presented in reference 11. The control angle vector has six components listed in equations (78) and 79) - i.e. cosine and sine components of 3-, 4-, and 5-per-rev. inputs. Three airframe vibrations (longitudinal, lateral, and vertical) were selected for inclusion in the performance index, J, to be minimized (see equation (90)). Elements of the weighting matrix w_z were 20,000, 20,000, and 150,000 - i.e., vertical vibration reduction was given more weight than rotor inplane vibration reductions. Diagonal elements of the control weight matrix used to limit the amplitudes of HHC control inputs were each equal to .01. Analytical control inputs were found to be less than 1.5° for all conditions except μ = 0.5 where θ_{3s} was predicted equal to 3°. The test HHC inputs were limited to a maximum of 1.5°. The analytical controller employed an analytical determination of the T matrix (see Higher Harmonic Control for Vibration Reduction). Noise was not represented.

Correlations for Baseline Conditions

Airframe Vibrations.- Comparison of predicted vibration levels for a three mode and nine mode solution versus ARES test data are shown in Figure 36. Both solutions adequately predict the trend of increasing vibration levels with increasing advance ratio. The modes used for the three mode solution are those modes with frequencies closest to the rotor 4/rev. which should be the primary

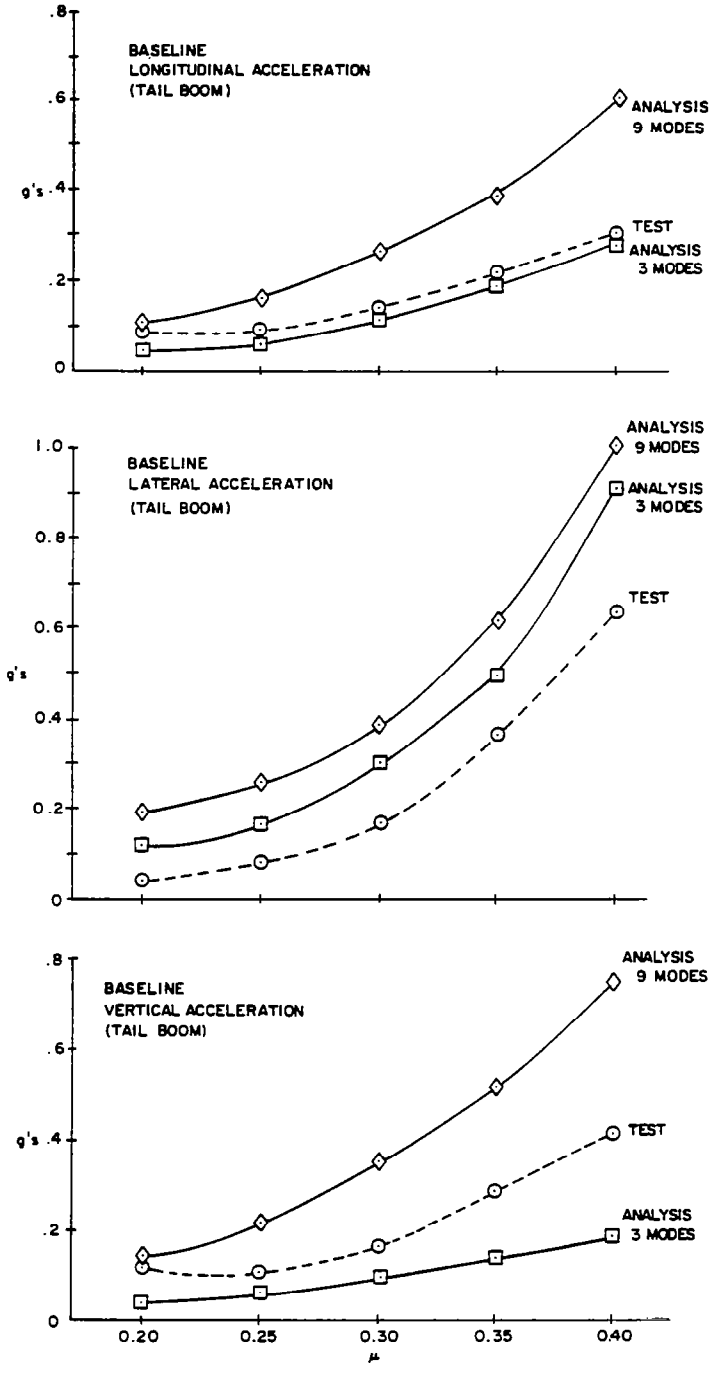

Figure 36. Correlation of Fuselage Accelerations.

contributions to vibration levels. The nine mode solution was employed in an attempt to improve the correlation with test data and assess the sensitivity to modal inputs. As would be expected, the additional modes resulted in higher absolute values of vibration levels, however, despite significant fuselage modal participation of modes 2, 3, 8, and 9, the large contribution to vibration levels was not expected. In fact, inclusion of the additional six modes results in predicted vibration levels significantly higher than measured values. All modes used were obtained from random shake test excitations which historically have proved less accurate than swept sine results. Since the vibration predictions appear to be very sensitive to modal characteristics, a higher level of accuracy in representing the fixed system modes is desirable.

Rotor Blade Moments. - Blade vibratory bending and torsion moment trends with airspeed predicted by the analysis (see Figure 37) were examined. Edgewise moments are overpredicted whereas the torsion moments are underpredicted by more than 50 percent. Blade moment variations with radius shown in figure 38 for $\mu = 0.30$ also have the same behavior.

The torsion test data in Figure 38 appear to contain errors. Test data for $C_T/\sigma = .075$ and $\mu = 0.3$ derived from Reference 20 are plotted in Figure 39. The test flatwise and edgewise moments show a slight increase in comparison with the curves in Figure 38. The torsion correlation is good, suggesting that the torsion test data in Figure 38 contain errors.

Figures 40 and 41 show the harmonics of the blade moments at mid span and $\mu = 0.30$. Figure 41 contains test results from Reference 20. The flatwise moment harmonics are predicted adequately by the analysis.

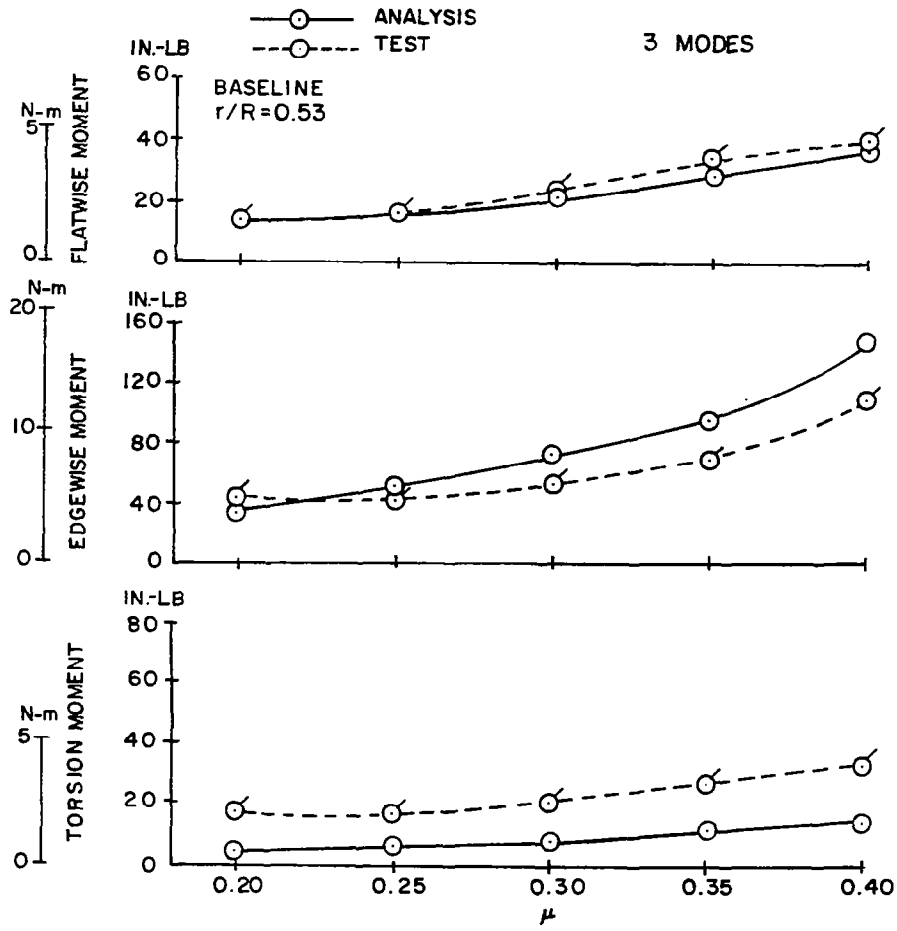

Figure 37. Variations of Blade Moments with Advance Ratio.

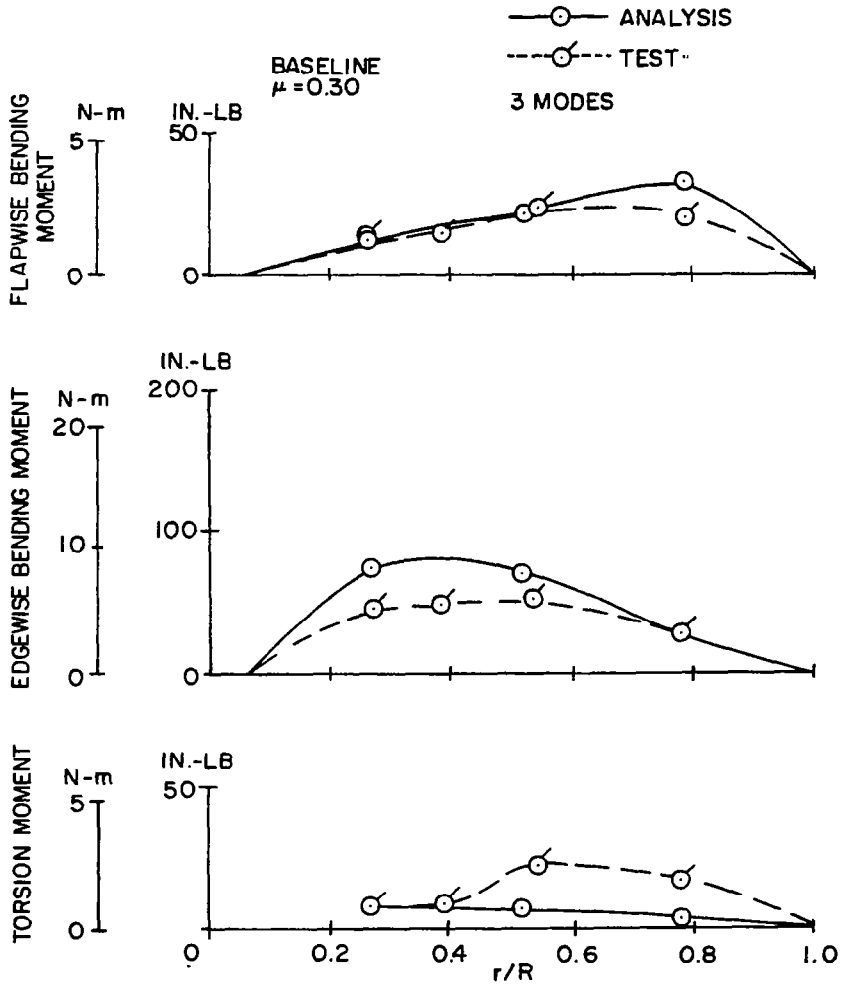

Figure 38. Radial Distributions of Blade Moments at 0.3 Advance Ratio.

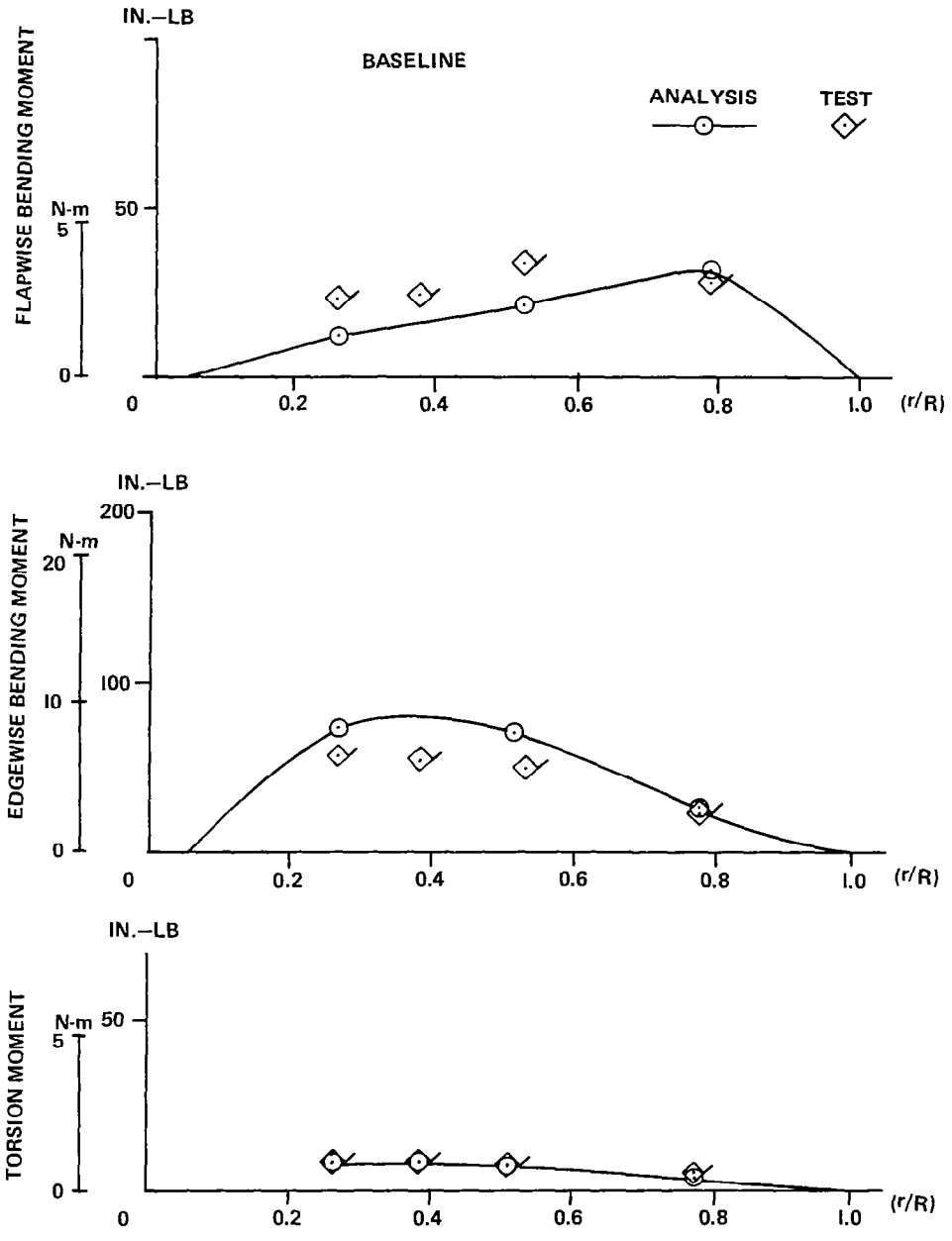

Figure 39. Correlations of Blade Moments at 0.3 Advance Ratio with Test Data from Reference 20.

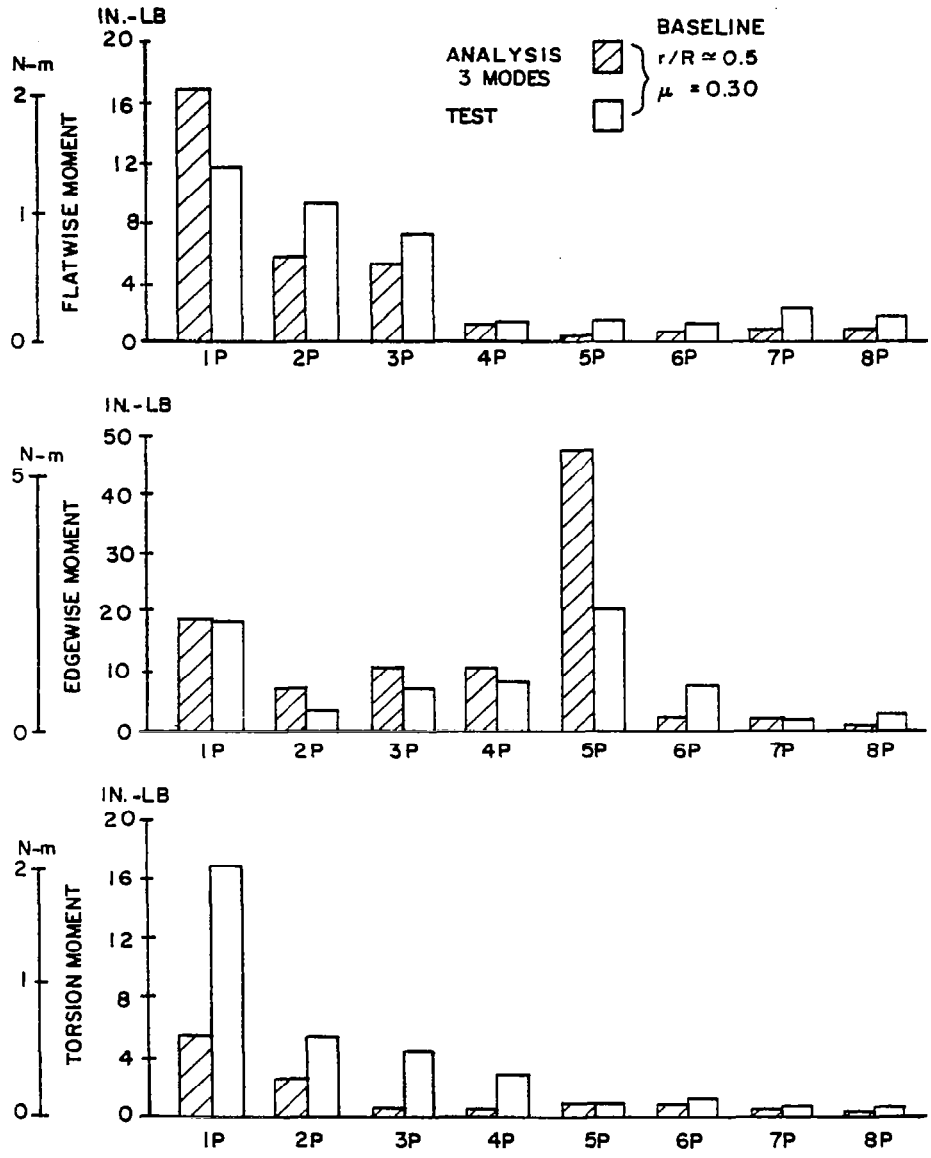

Figure 40. Blade Moment Harmonic Correlation.

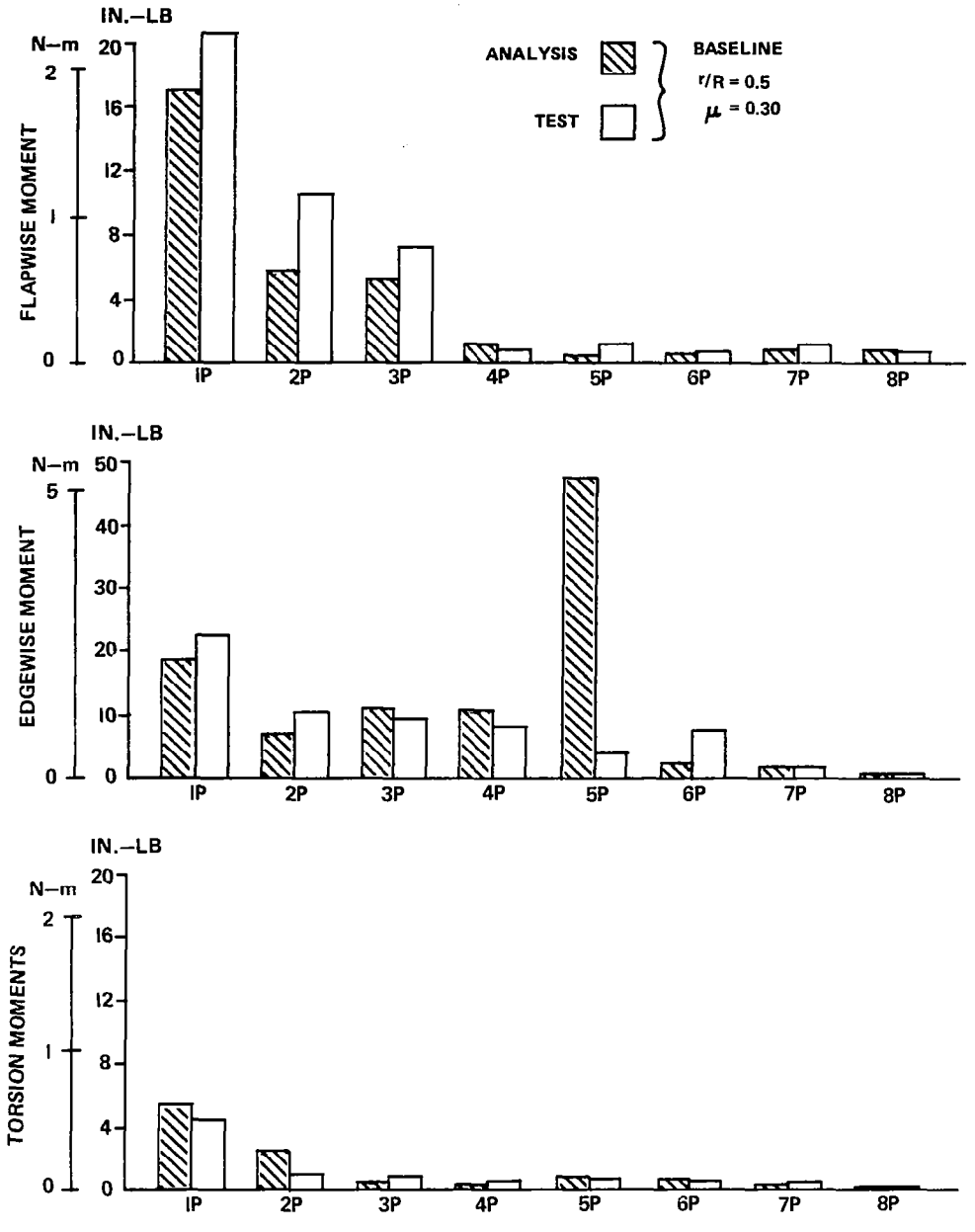

Figure 41. Blade Moment Harmonic Correlation with ARC Test.

The edgewise harmonics correlate satisfactorily except at 5- and 6-per-rev. The analysis predicts a large 5/rev. moment and a small 6/rev. moment. The large 5/rev. component accounts for the overprediction of the edgewise moments, (see Figures 37 and 39). This 5/rev. amplification is probably due to resonance of this mode with 4/rev. rotor hub excitation, as explained below.

Pitch link load comparisons were similar to the torsional moment curves in Figure 37.

The conclusion is that the blade moment trends are adequately predicted by the analysis. Absolute values appear to depend on how accurately the blade parameters are modelled, especially, blade frequencies.

Hub/Balance Force Correlations. - Analytical 4-per-rev. hub force and balance test force trends with airspeed are shown in Figure 42. A direct comparison of hub loads is not made because the test data consist of balance loads while the analysis data consist of hub loads. A dynamic calibration matrix is required to relate the 4-per-rev. loads at the model hub to the 4-per-rev. loads sensed by the balance. The calibration matrix was not available in this correlation study. Figure 42 also shows that the longitudinal hub force from analysis has a greater sensitivity to airspeed than the longitudinal balance force. The lateral and vertical hub force trends with airspeed correlate fairly well with the corresponding balance loads. Since no direct comparisons of hub loads are available, no conclusions can be made on the accuracy of the analysis, except that the analysis appears to show the proper trend of hub loads with airspeed.

Effect of Hub Displacements. - An area of interest is the sensitivity of blade moments and hub loads to support system flexibility. If the support system modal attributes are such that blade loads are substantially different from those with a fixed

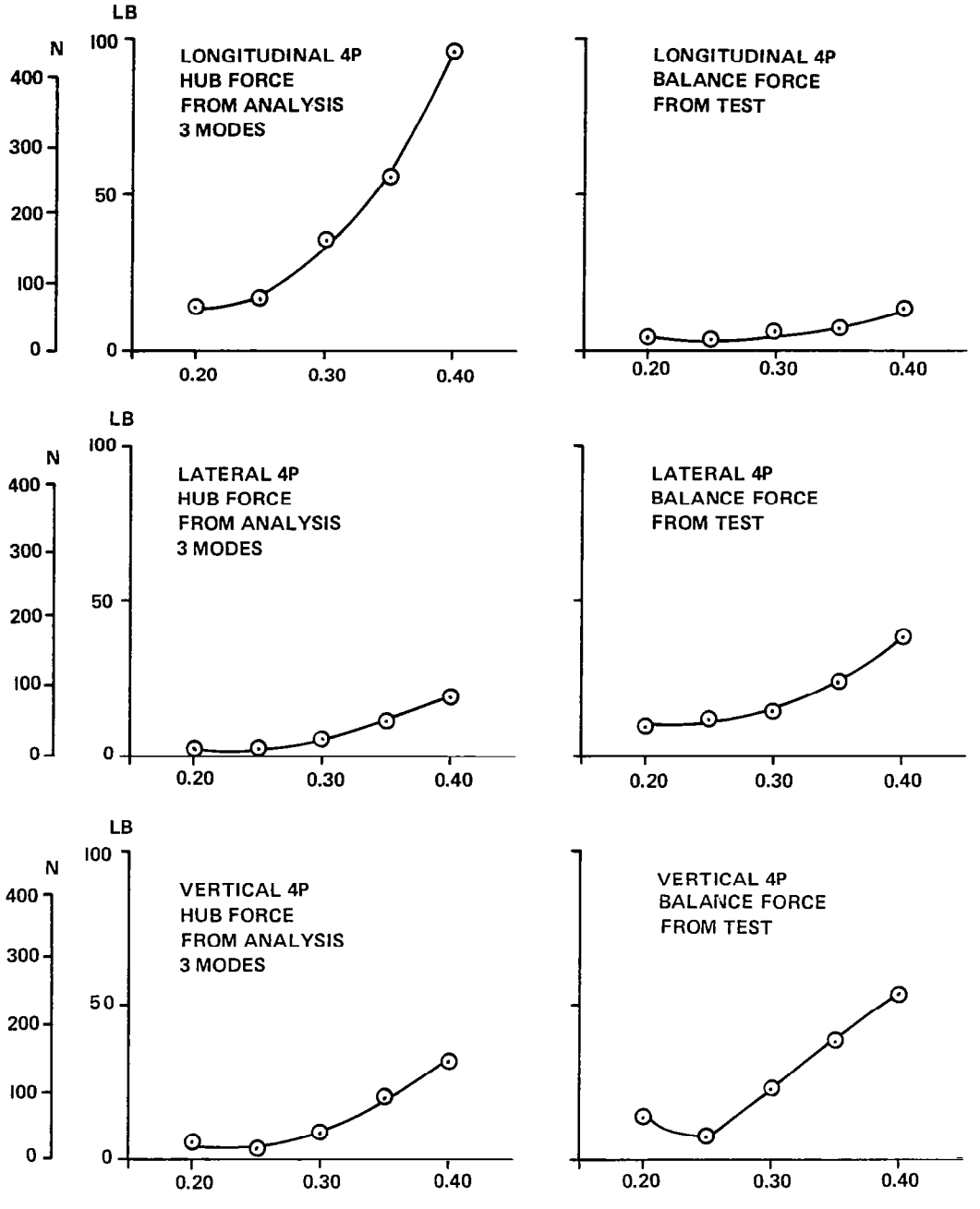

Figure 42. Comparison of Variations with Advance Ratio of Predicted Hub Loads and Measured Balance Loads.

hub, then the blade analysis should properly account for effects of hub displacements.

Figure 43 shows that blade edgewise moments are affected by hub flexibility, and that hub motion increases the alternating edgewise moment at mid span by 50 percent. Table 10 reveals the source of the increase in edgewise moments. The blade has an edgewise mode at 5/rev. which transforms into 4/rev. and 6/rev. in the fixed system. Only the 4/rev. component is transmitted to the fixed system for this 4-bladed rotor system. This transformed 4/rev. edgewise mode is at resonance with the 4/rev. rotor excitation and may couple with the fixed system lateral roll mode at 4.4/rev. This speculation is reinforced by Figure 44 which shows that the in-plane hub forces are more sensitive to hub displacement than the vertical hub force.

The deduction is that hub participation can have a substantial effect on blade moments and hub loads. The accurate prediction of hub loads is sensitive to accurate characterization of support system modal attributes and rotor blade frequencies. The lack of agreement of edgewise moments with test data is likely to be due to inaccurate characterization or rotor blade natural frequencies in the analysis. Because rotor loads are the primary excitation sources of coupled rotor/airframe systems, these sensitivities show the importance of accurate modal characteristization of both the rotor and airframe for vibration prediction.

Correlation with HHC Non-optimal Inputs

The Coupled Rotor/Airframe Vibration analysis was executed to predict airframe vibrations, rotor bending moments and hub loads utilizing arbitrary higher harmonic control inputs. Comparison with wind tunnel measurements for the same inputs is discussed below.

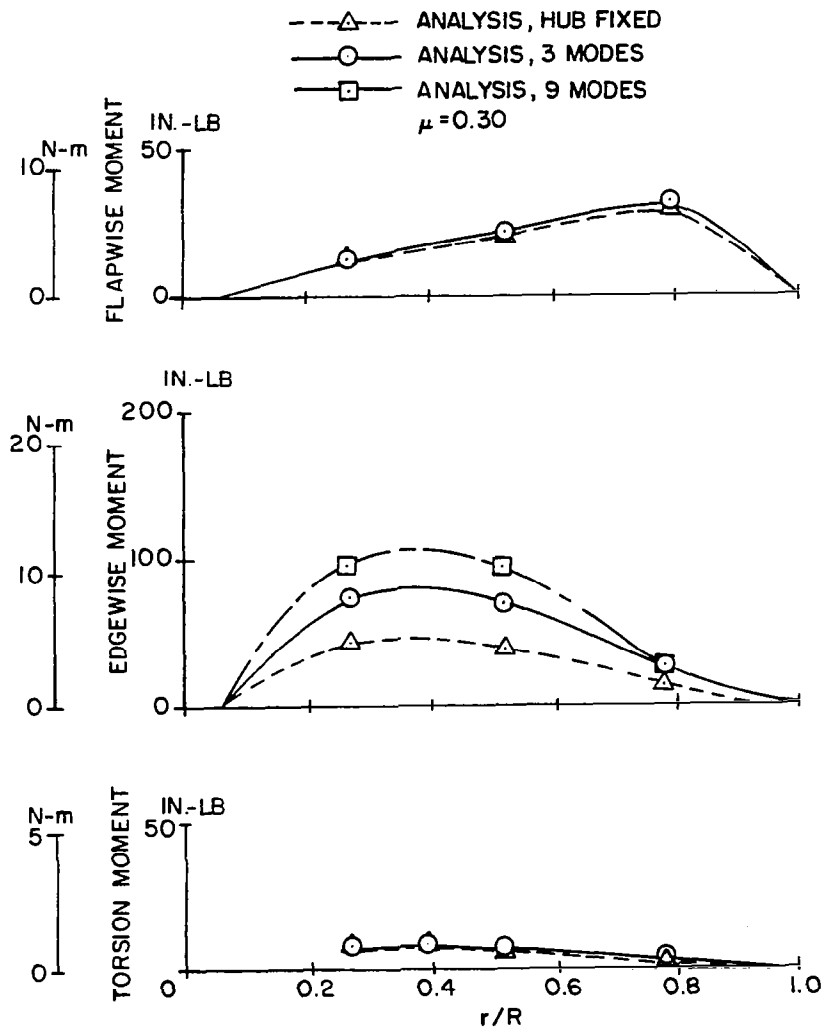

Figure 43. Effects of Hub Displacement on Blade Loads.

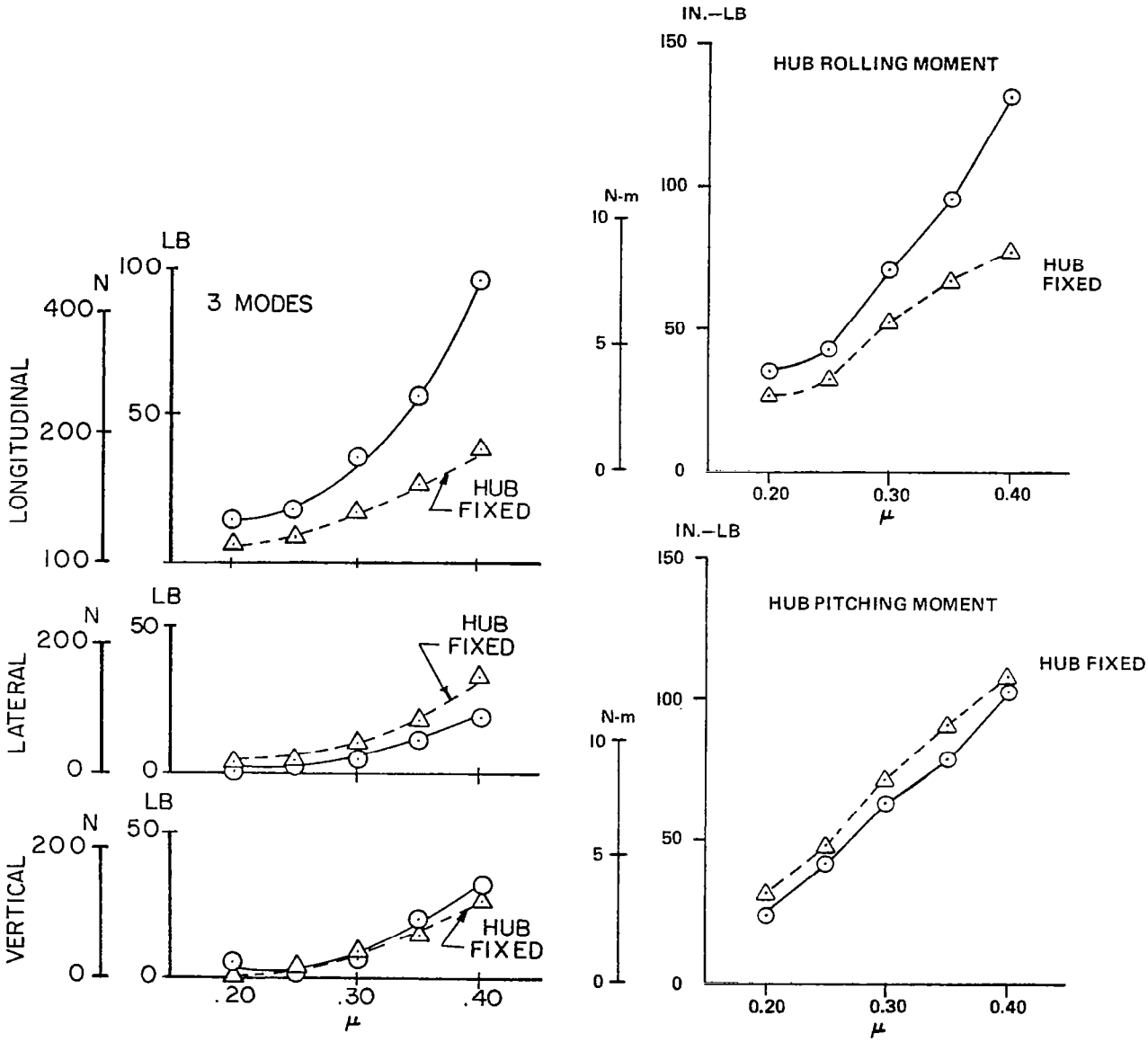

Figure 44. Effects of Hub Displacement on Hub Loads.

Airframe Vibrations. - Figure 45 shows the effect of 3/rev. HHC pitch inputs on airframe 4/rev. vibration. Also shown is the analytical estimate of vibration obtained from the Coupled Rotor/ Airframe Analysis with HHC and a three mode representation. Absolute values are underpredicted and the trend in vibration reduction with HHC application is not predicted uniformly. The nine mode solution results shown in Figure 46 in general agree better with the test data and shows uniformly higher vibration levels than the three mode solution.

Figure 47 shows vibration vector corrrelations for the airframe 4/rev. longitudinal vibrations. For all four HHC input values, the analysis is able to predict the phase changes due to HHC inputs. Amplitude comparisons are the same as in Figure 45.

Rotor Blade Moments. - Figure 48 shows the effect of HHC inputs on blade bending moments. This figure indicates that bending moments, especially edgewise moments, are sensitive to the HHC inputs. Harmonic analysis of the moments (see Figure 49) indicates the differences are primarily due to large 3/rev. flatwise and 6/rev. edgewise contributions for the HHC applications. The predicted blade moment distribution for baseline and HHC input case are provided in Figure 50. The sensitivity to HHC inputs observed in the measured data is not predicted.

The sensitivity of the measured blade loads to a 3/rev. input may be due to impurities in the 3/rev. pitch input and the proximity of the test blade edgewise mode to 6/rev. The impurities are assumed to give rise to a 6/rev. excitation which excites the 6/rev. edgewise mode. This observation was made in Reference 11. The analysis which models a 3/rev. HHC input as a 3/rev. pitch change is not able to predict this effect.

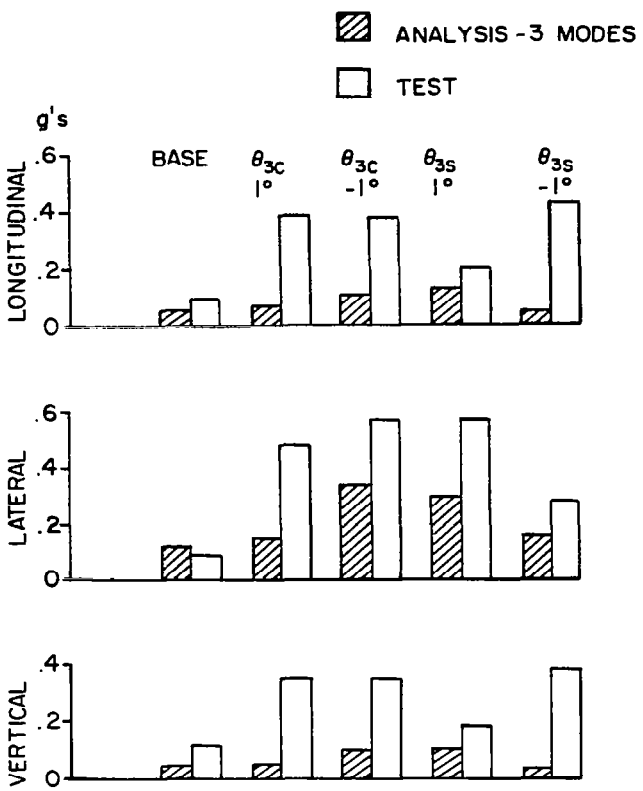

Figure 45. Effects of Specified HHC on Amplitudes of Airframe Vibrations - Three Mode Solution.

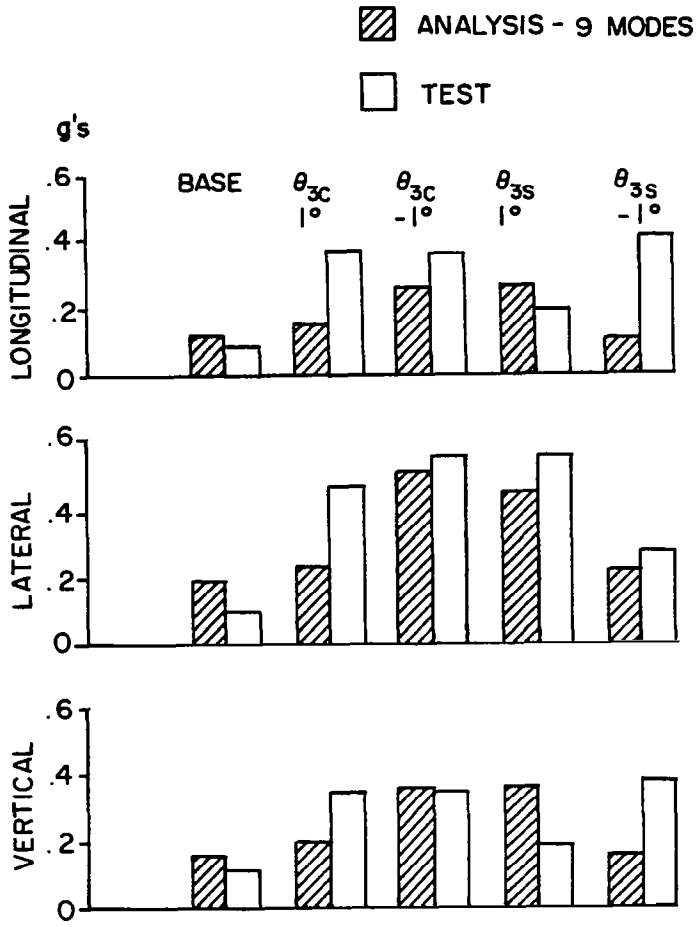

Figure 46. Effects of Specified HHC on Amplitudes of Airframe Vibrations - Nine Mode Solution.

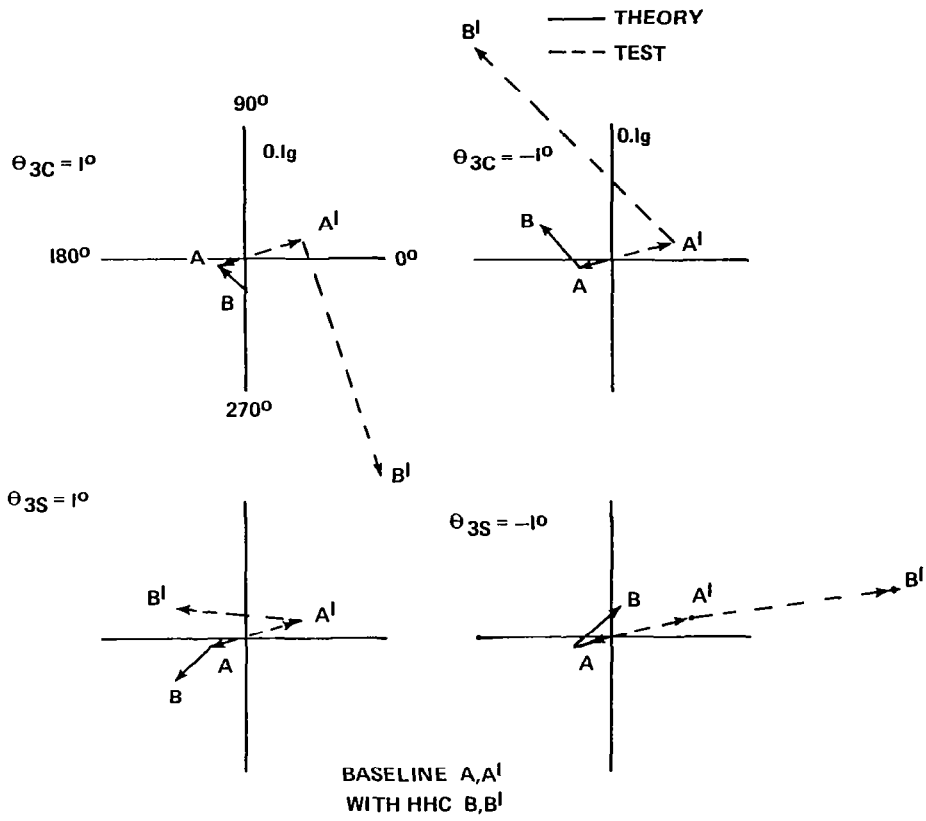

Figure 47. Effects of Specified HHC on Longitudinal Vibration Vectors - Three Mode Solutions.

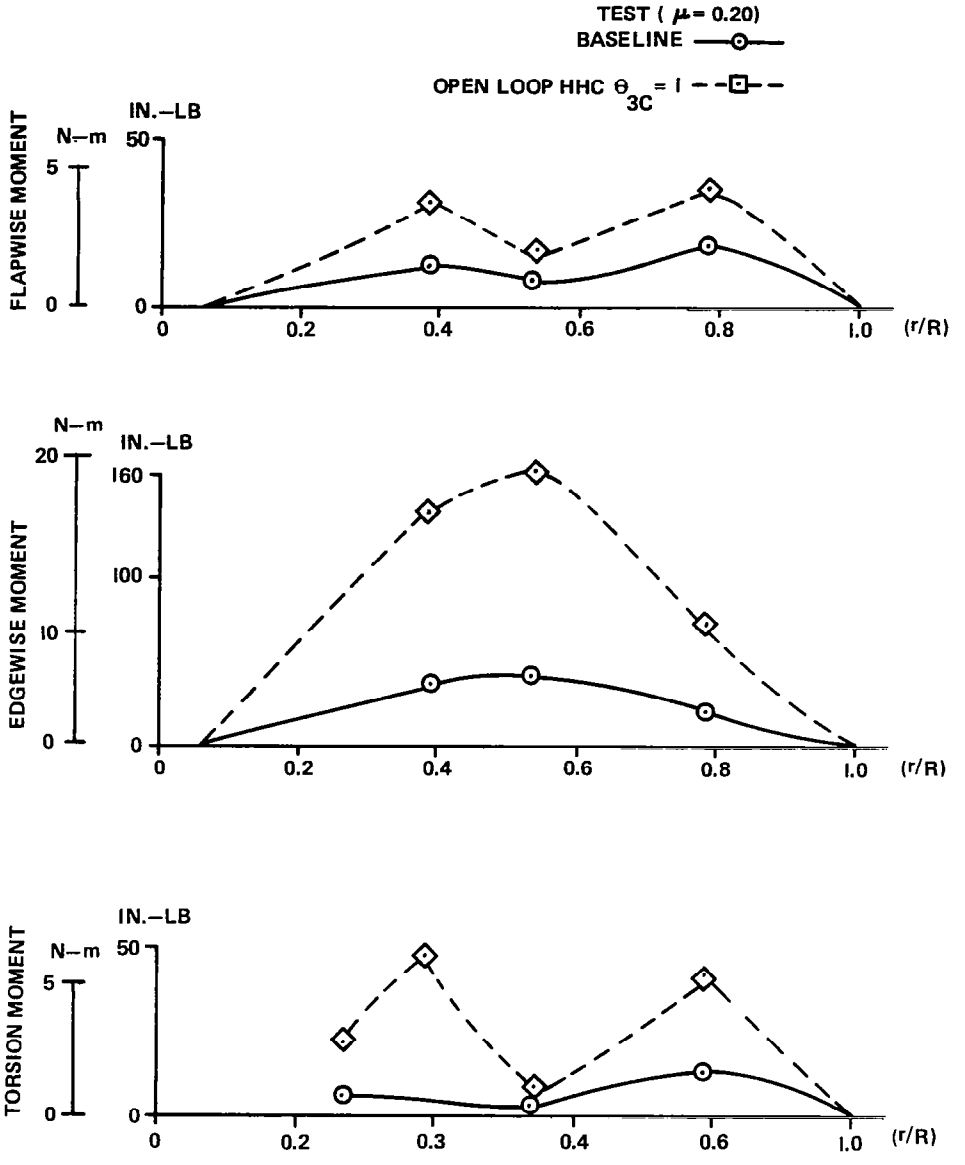

Figure 48. Effects of Specified HHC on Measured Blade Moment Distributions.

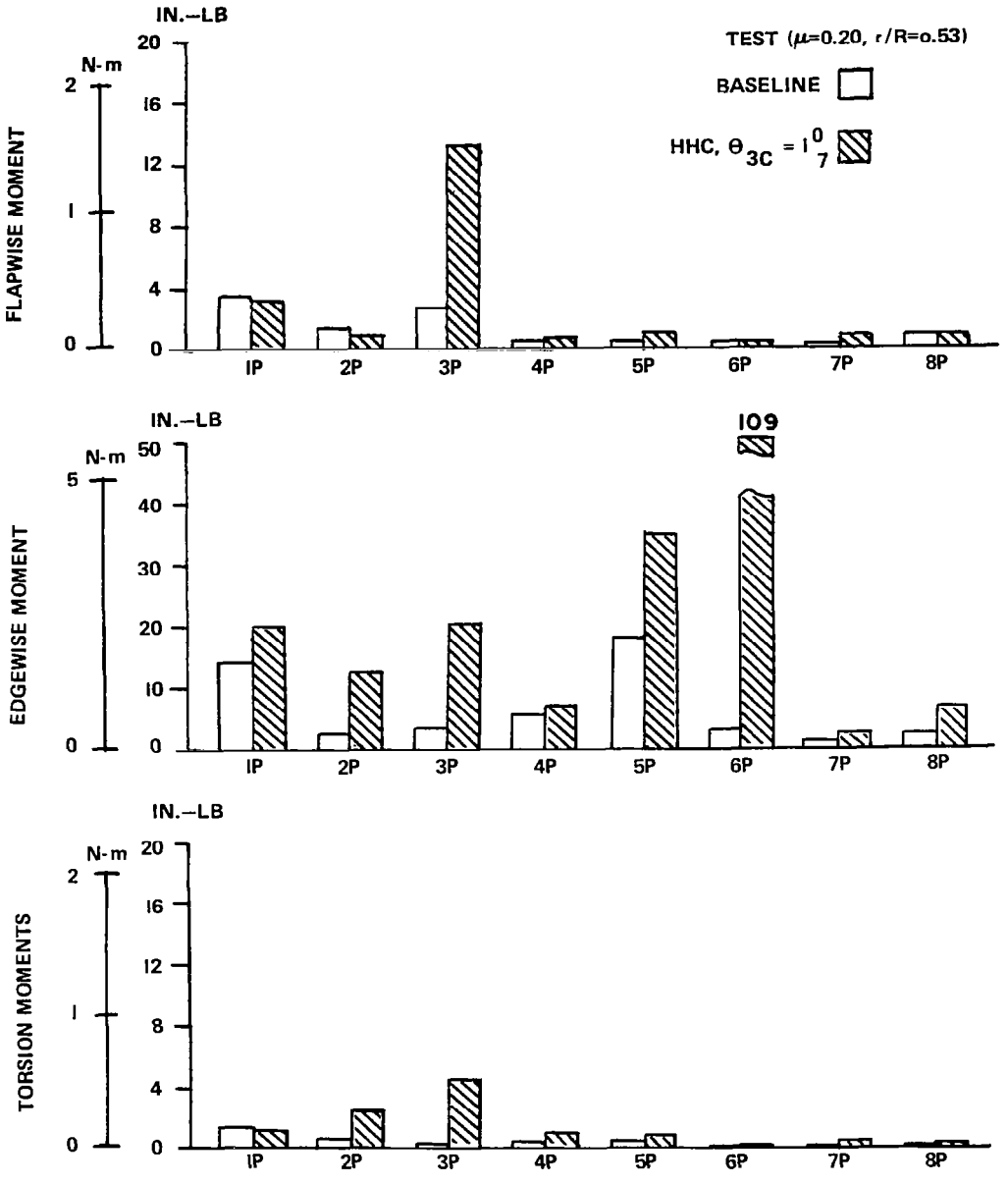

Figure 49. Effects of Specified HHC on Harmonics of Measured Blade Moments.

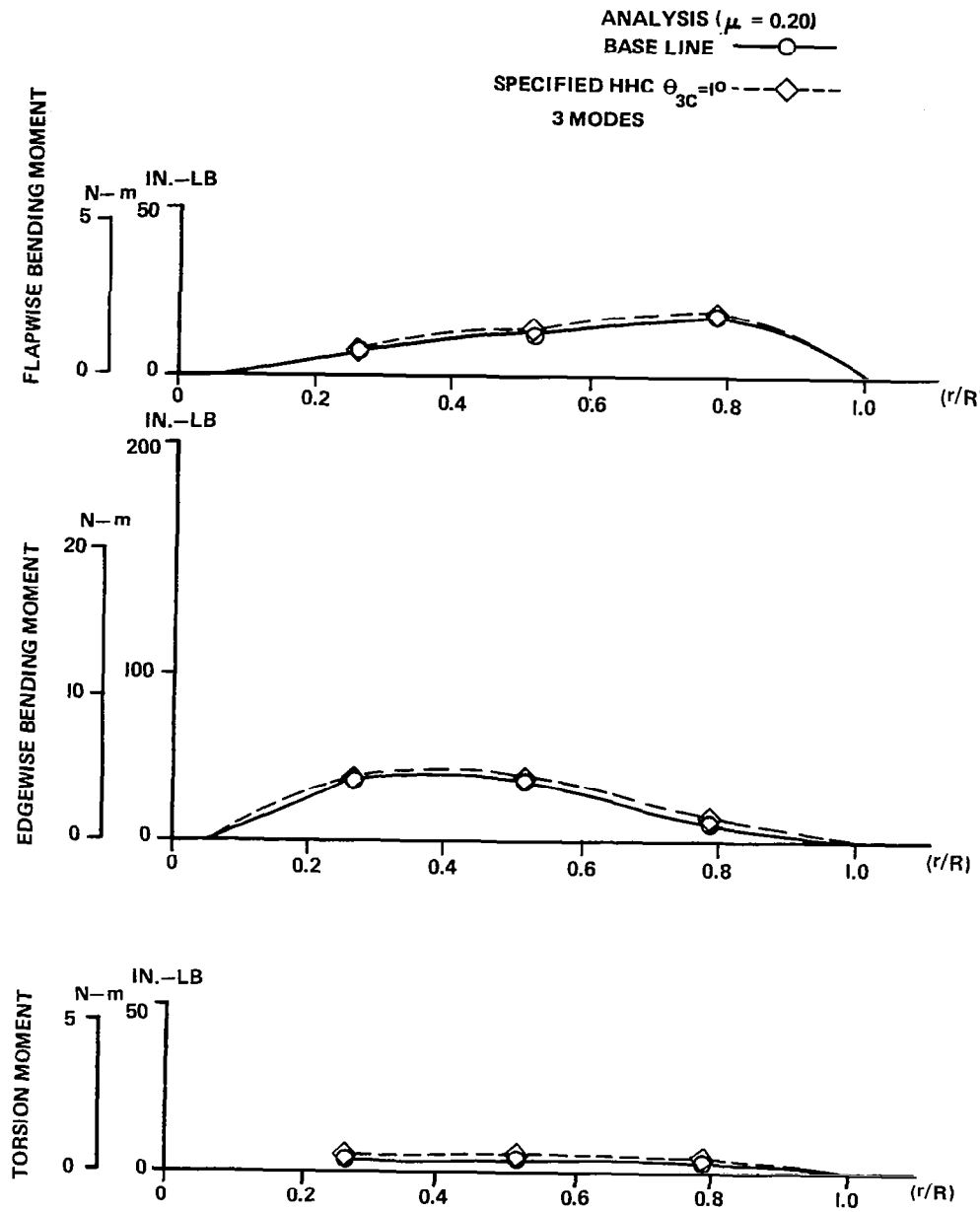

Figure 50. Effects of Specified HHC on Predicted Blade Moment Distributions.

Hub/Balance Force Correlations. - Figure 51 shows side-by-side comparisons of predicted hub forces with test balance forces. Variations with HHC inputs are not well correlated. Because no direct hub load comparisons are made, no conclusions are drawn.

Optimal HHC Solutions

Analytical and test results are compared for the effects of optimal values of HHC inputs on airframe vibrations, blade moments, and hub loads.

Airframe Vibration. - Predicted and measured airframe vibrations for the baseline model and optimal HHC inputs as functions of advance ratio are shown in Figure 52. The analysis predicts the proper trends with HHC application and advance ratio increases for both the vertical and longitudinal accelerations. The test data indicate that the HHC inputs are not effective in reducing lateral vibrations in contrast to the analytical predictions.

Blade Bending Moments. - Both analysis and test show that for the conditions selected, the spanwise blade bending moment distributions are not sensitive to HHC inputs, Figure 53. The disagreement in the torsion moments is probably due to errors in the test data as noted in the correlation of baseline conditions.

Figure 54 shows that predicted flatwise and edgewise moments are consistent with measured values and that the trends with advance ratio are predicted correctly. The trend for torsional moments is consistent but the predicted magnitudes are consistently lower than measured.

Figure 55 shows comparisons between test results and predicted blade moment harmonics at midspan and $\mu = 0.30$. The torsion moments will not be discussed because the test data probably contain errors. The flatwise and edgewise harmonics of moments

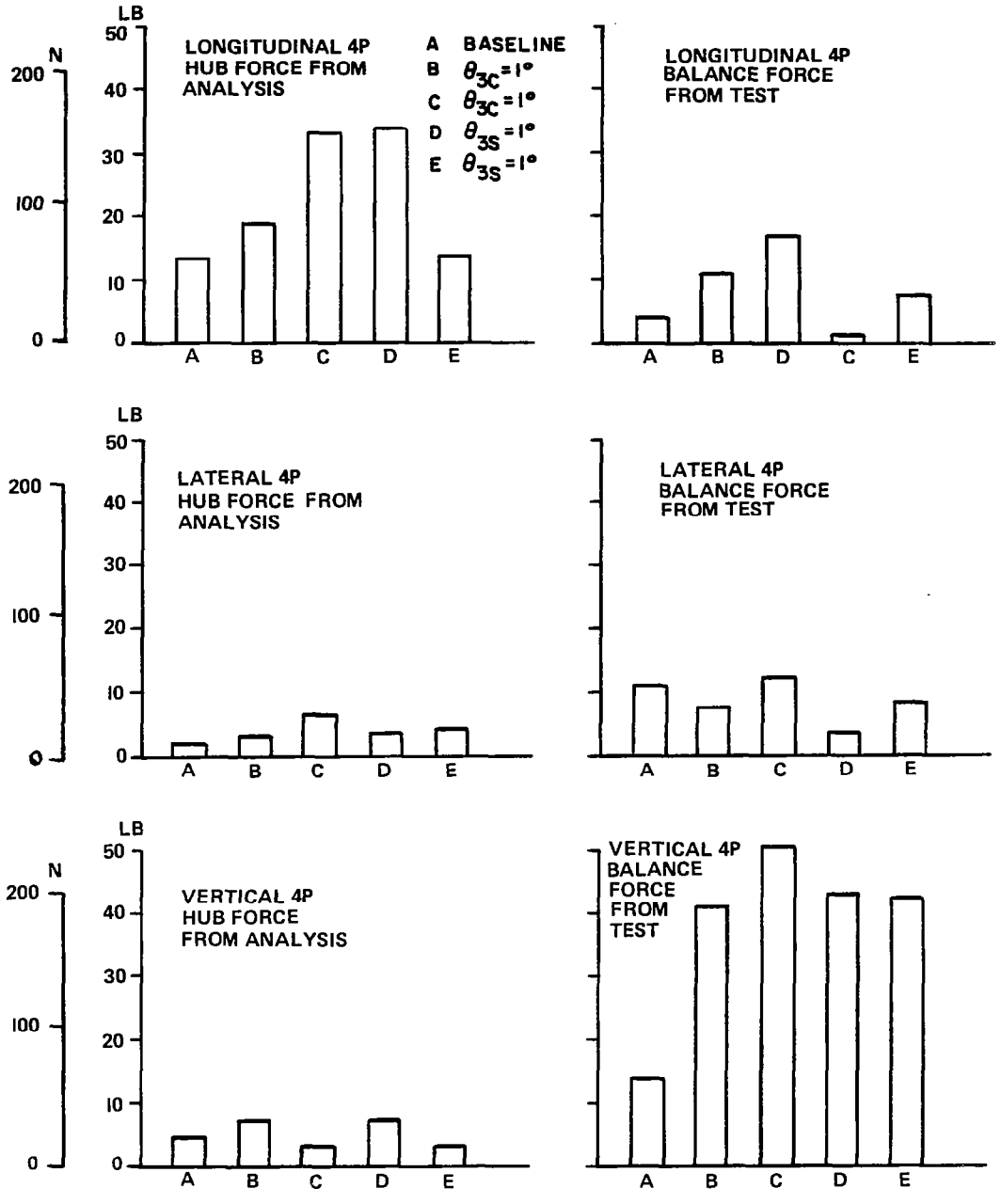

Figure 51. Effects on Specified HHC on Hub Forces.

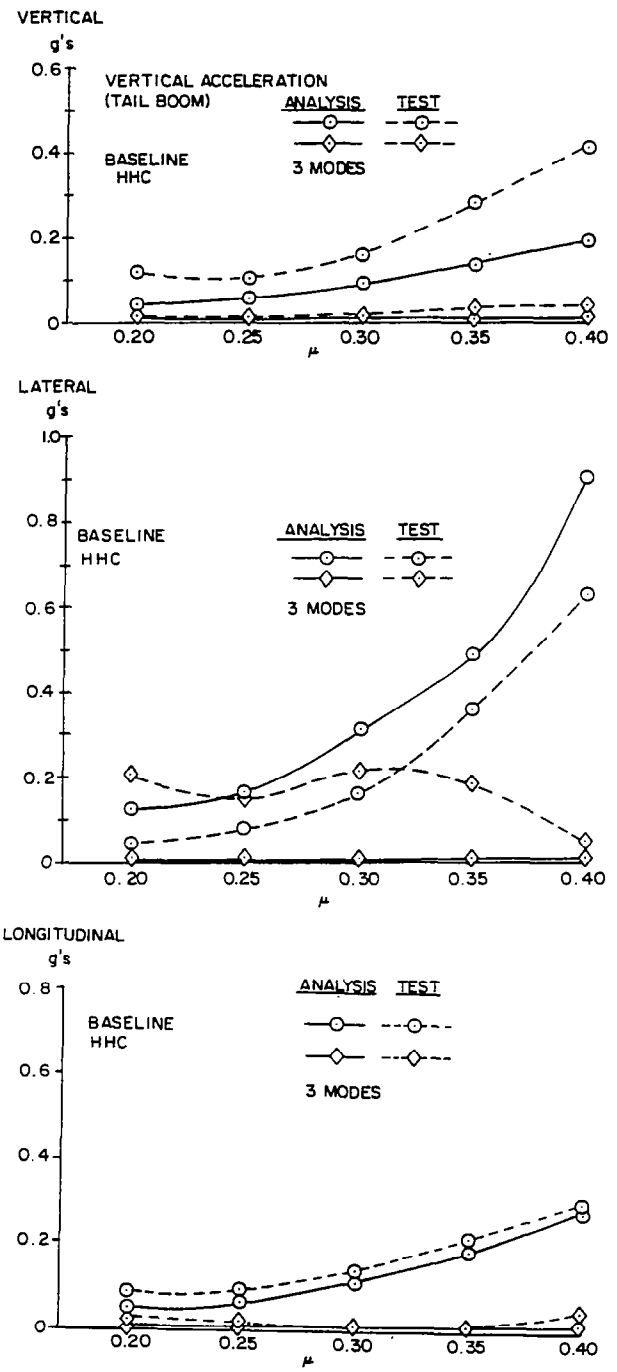

Figure 52. Effects of Optimal HHC on Fuselage Vibrations.

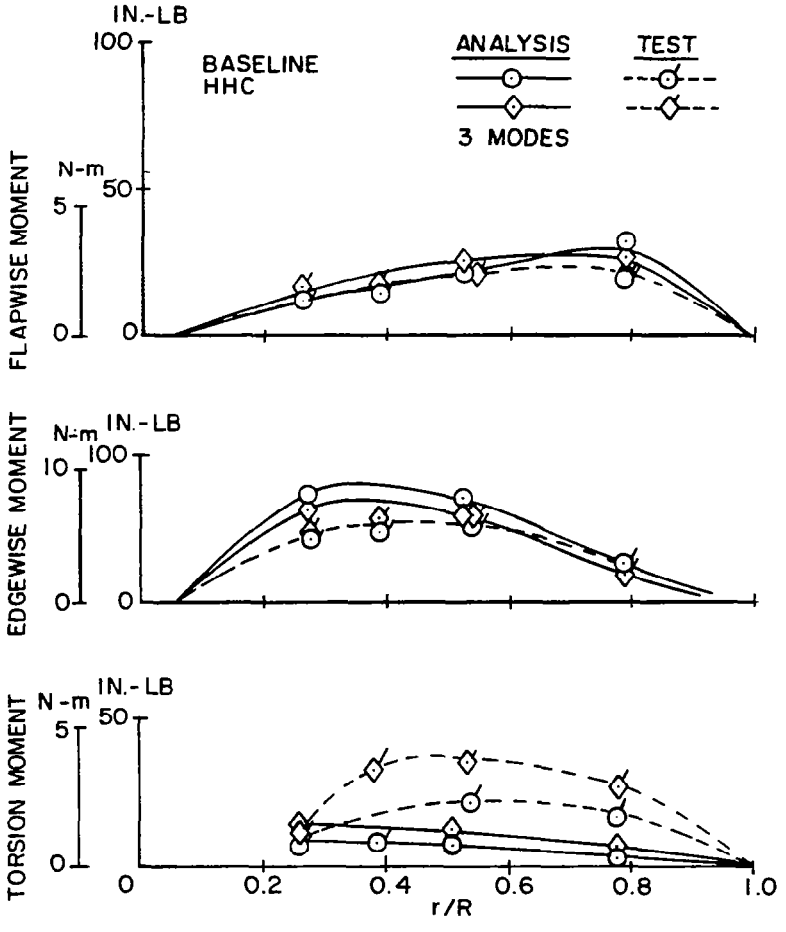

Figure 53. Effects of Optimal HHC on Blade Moments.

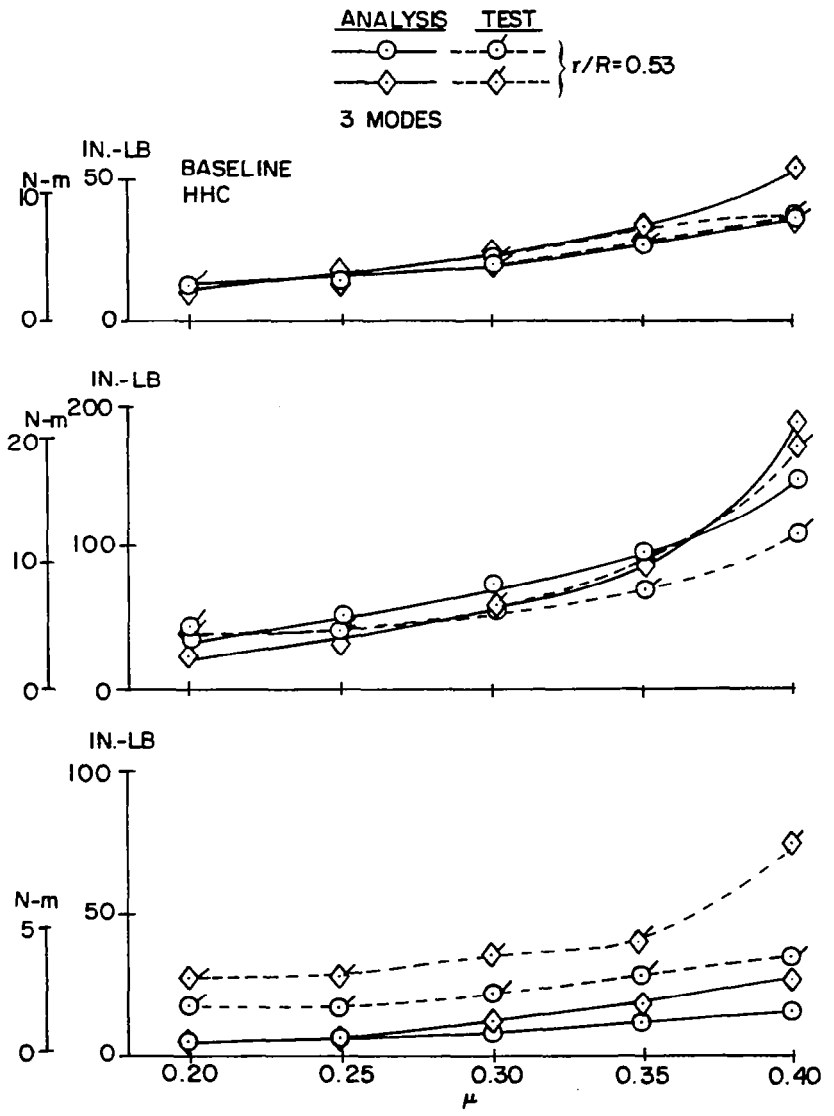

Figure 54. Effects of Optimal HHC on Variations with Advance Ratio of Blade Moments at One Blade Station.

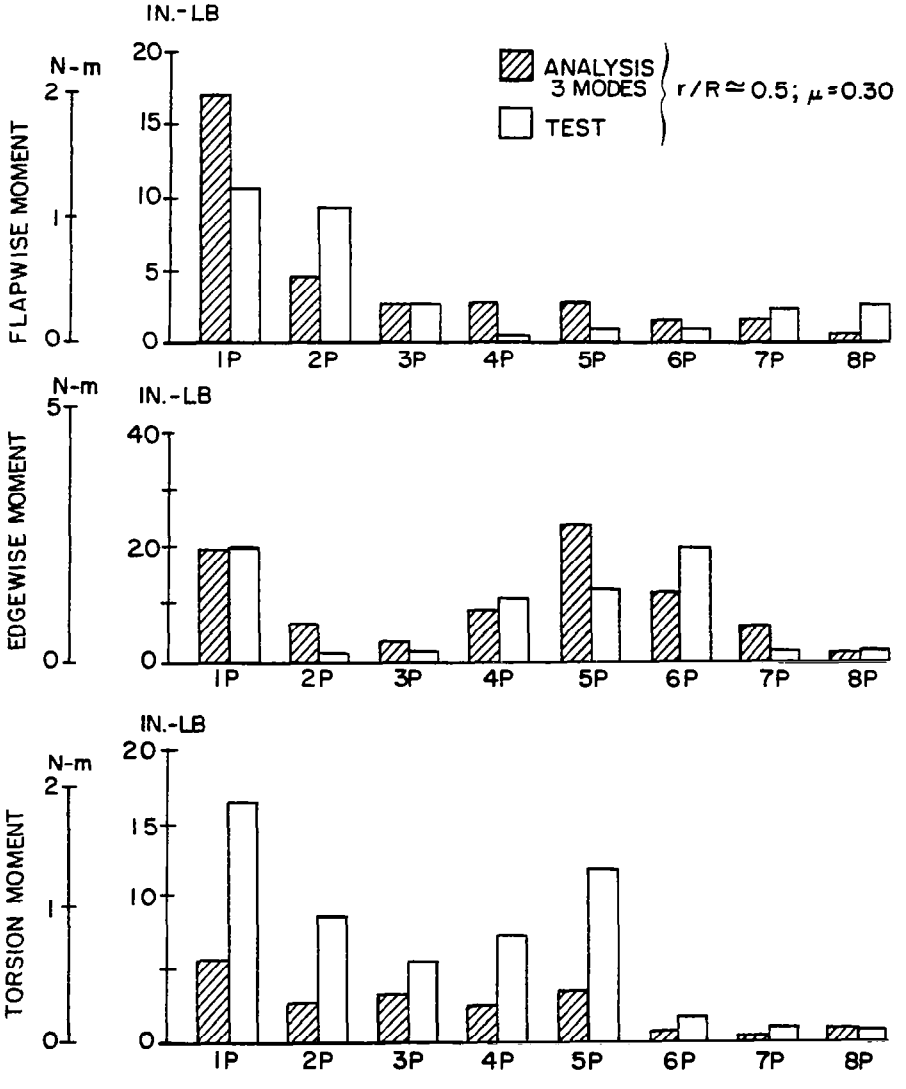

Figure 55. Effects of Optimal HHC on Harmonics of Blade Moments at One Advance Ratio and Blade Station.

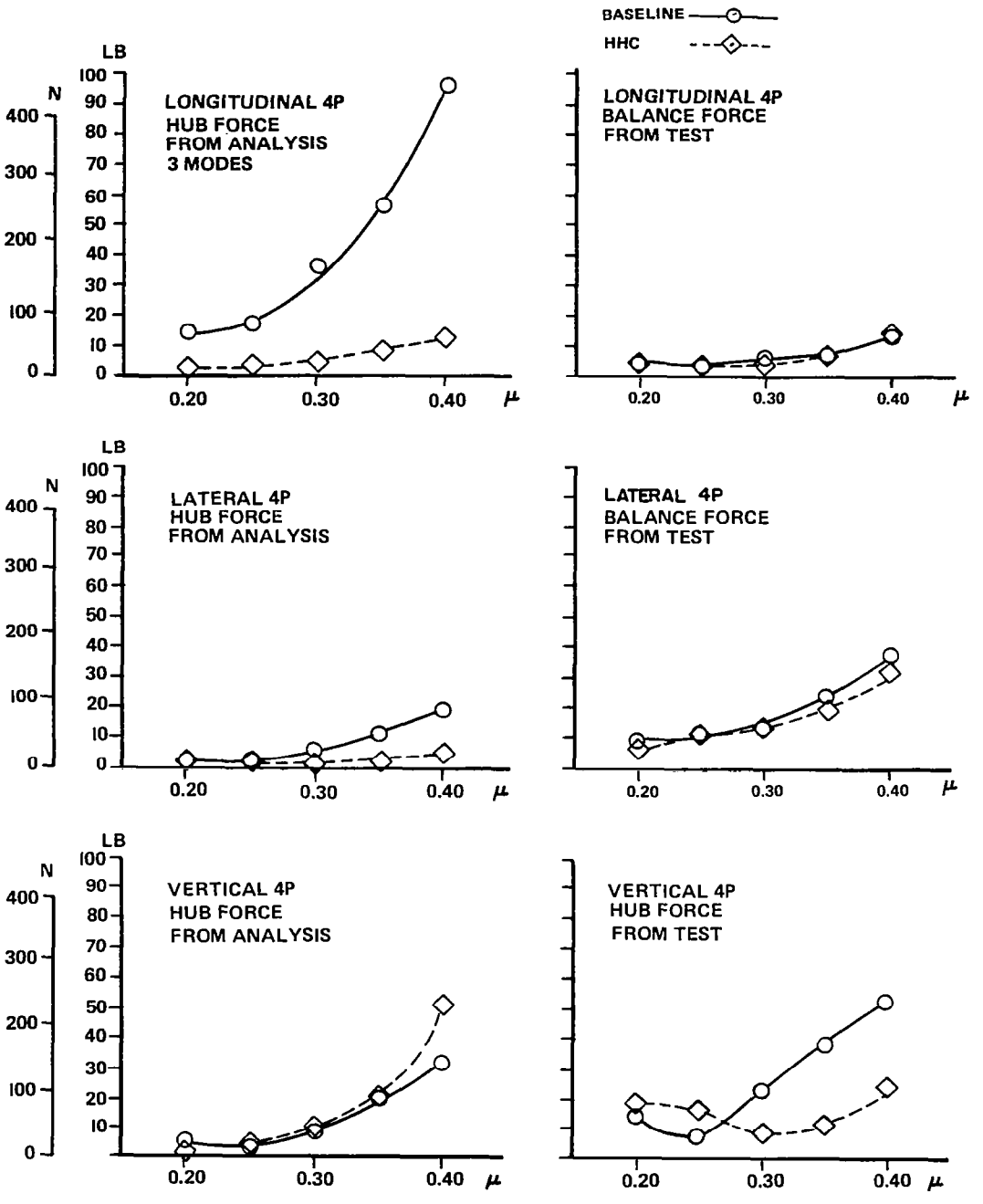

Figure 56. Effects of Optimal HHC on Comparisons of Predicted Hub Loads and Measured Balance Loads

correlate fairly well. The overprediction of the 5/rev. and underprediction of the 6/rev. edgewise components may be due to the input blade edgewise mode frequency being 5/rev. while the actual frequency is closer to 6/rev., as discussed in the preceding text.

Hub/Balance Force Comparisons. - Figure 56 shows that the analysis predicts a large effect of the HHC inputs on the longitudinal hub force which is not evidenced in the measured balance loads. The effects on lateral and vertical forces are more consistent but the measured balance vertical forces are more sensitive to HHC inputs than the predicted effect on vertical hub forces.

CONCLUDING REMARKS

1. A Coupled Rotor/Airframe Vibration Analysis has been developed to serve as a preliminary design tool for predicting helicopter vibrations and a research tool to quantify the effects of structural properties, aerodynamic interactions and vibration reduction devices on vehicle vibration levels.

2. The analysis developed employs a substructure method which provides an efficient stand-alone mode operation of a Base Program while retaining a high level of aerodynamic and dynamic sophistication by linking output of External Programs.

3. The Base Program operating in a stand-alone mode can efficiently be used to study design changes in fuselage properties and vibration reduction devices.

4. The substructure basis of the Base Program is well suited to allowing the Base Program to introduce data from user provided External Programs of the rotor system. The substructure basis also will facilitate growth of the Base Program to include additional internal components.

5. The Rotor/Airframe coupling in the analysis is accomplished using an impedance matching technique.

6. The current External Programs supporting the Base Program provide the capability to model articulated, hingeless and teetering rotor systems, higher harmonic control inputs, main rotor wake/empennage excitation sources and hover, transition and forward flight regimes.

7. A limited correlation study with a dynamically scaled wind tunnel model indicates:

   a. The analysis predicts the proper trends in vibration levels as a function of advance ratio.

   b. The analysis predicts the proper trends in vibration levels and blade bending moments with application of higher harmonic control.

   c. Absolute values of predicted vibration levels and blade bending moments are sensitive to airframe modal characteristics and were not uniformly consistent with measured values.

APPENDIXES

Appendix A - Illustration of System Synthesis

Substructure Terminology

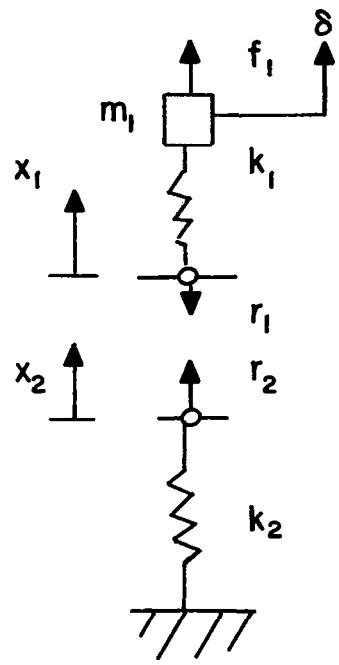

Unconnected Coordinate

Element 1

Connection Node 1

Connection node coordinate

Connection node coordinate

Connection Node 1

Element 2

Sketch (A1)

Substructure Equations of Motion

Element 1

Coordinates $\{x\}^{(1)} = \begin{Bmatrix} \delta \\ x_1 \end{Bmatrix}$ (A1)

Properties $[m]^{(1)} = \begin{bmatrix} m_1 & 0 \\ 0 & 0 \end{bmatrix}$ (A2)

$[k]^{(1)} = \begin{bmatrix} k_1 & -k_1 \\ -k_1 & k_1 \end{bmatrix}$ (A3)

External force $\{f\}^{(1)} = \begin{Bmatrix} f_1 \\ o \end{Bmatrix}$ (A4)

Reaction loads $\{r\}^{(1)} = \begin{Bmatrix} o \\ r_1 \end{Bmatrix}$ (A5)

Element 2

Coordinates $\{x\}^{(2)} = \{x_2\}$ (A6)

Properties $[m]^{(2)} = [o]$ (A7)

$[k]^{(2)} = [k_2]$ (A8)

External force $\{f\}^{(2)} = \{o\}$ (A9)

Reaction loads $\{r\}^{(2)} = \{-r_2\}$ (A10)

Assembled System Equations of Motion

Dependent coordinates

$$X_D = \begin{Bmatrix} \{x\}^{(1)} \\ \{x\}^{(2)} \end{Bmatrix} = \begin{Bmatrix} \delta \\ x_1 \\ x_2 \end{Bmatrix} \quad \text{(A11)}$$

Properties

$$M_D = \begin{bmatrix} [m]^{(1)} & [o] \\ [o] & [m]^{(2)} \end{bmatrix} = \begin{bmatrix} m_1 & o & o \\ o & o & o \\ o & o & o \end{bmatrix} \quad \text{(A12)}$$

$$K_D = \begin{bmatrix} [k]^{(1)} & [o] \\ [o] & [k]^{(2)} \end{bmatrix} = \begin{bmatrix} k_1 & -k_1 & 0 \\ -k_1 & k_1 & 0 \\ o & o & k_2 \end{bmatrix} \quad \text{(A13)}$$

External force $F_D = \begin{Bmatrix} \{f\}^{(1)} \\ \{f\}^{(2)} \end{Bmatrix} = \begin{Bmatrix} f_1 \\ 0 \\ 0 \end{Bmatrix}$ (A14)

Reaction load $R_D = \begin{Bmatrix} \{r\}^{(1)} \\ \{r\}^{(2)} \end{Bmatrix} = \begin{Bmatrix} 0 \\ r_1 \\ -r_2 \end{Bmatrix}$ (A15)

Assembled equation employing dependent coordinates

$$M_D \ddot{X}_D + K_D \dot{X}_D = F_D - R_D \quad \text{(A16)}$$

Mapping From Dependent Coordinates To Independent Coordinates

Component displacements are equated at connection node 1

$$x_2 = x_1 \quad \text{(A17)}$$

Therefore $\begin{Bmatrix} \delta \\ x_1 \\ x_2 \end{Bmatrix} = \begin{bmatrix} 1 & 0 \\ 0 & 1 \\ 0 & 1 \end{bmatrix} \begin{Bmatrix} \delta \\ x_1 \end{Bmatrix}$ (A18)

$$X_D = \beta X_I \quad \text{(A19)}$$

Independent coordinates

$$X_I = \begin{Bmatrix} \delta \\ x_1 \end{Bmatrix} \quad \text{(A20)}$$

Mapping $\beta = \begin{bmatrix} 1 & 0 \\ 0 & 1 \\ 0 & 1 \end{bmatrix}$ (A21)

System Synthesis

Properties of assembled system referred to independent coordinates

$$M = \beta^T M_D \beta = \begin{bmatrix} m_1 & 0 \\ 0 & 0 \end{bmatrix} \quad \text{(A22)}$$

$$K = \beta^T K_D \beta = \begin{bmatrix} k_1 & -k_1 \\ -k_1 & k_1+k_2 \end{bmatrix} \quad \text{(A23)}$$

$$F = \beta^T F_D \beta = \begin{Bmatrix} f_1 \\ 0 \end{Bmatrix}$$

$$\beta^T R_D = \begin{Bmatrix} 0 \\ r_1 - r_2 \end{Bmatrix} = \begin{Bmatrix} 0 \\ 0 \end{Bmatrix} \quad \text{(A25)}$$

because $r_1 = r_2$

Assembled system equation of motion

$$\begin{bmatrix} m_1 & 0 \\ 0 & 0 \end{bmatrix} \begin{Bmatrix} \ddot{\delta} \\ \ddot{x}_1 \end{Bmatrix} + \begin{bmatrix} k_1 & -k_1 \\ -k_1 & k_1 + k_2 \end{bmatrix} \begin{Bmatrix} \delta \\ x_1 \end{Bmatrix} = \begin{Bmatrix} f_1 \\ 0 \end{Bmatrix} \quad \text{(A27)}$$

$$M\ddot{X}_I + K X_I = 0 \quad \text{(A28)}$$

Recovery of Component Responses and Reactions

Components responses

$$X_D = \beta X_I \quad \text{(A29)}$$

$$\dot{X}_D = \beta \dot{X}_I \quad \text{(A30)}$$

$$\ddot{X}_D = \beta \ddot{X}_I \quad \text{(A31)}$$

e.g.

$$\begin{Bmatrix} \ddot{\delta} \\ \ddot{x}_1 \\ \ddot{x}_2 \end{Bmatrix} = \begin{bmatrix} 1 & 0 \\ 0 & 1 \\ 0 & 1 \end{bmatrix} \begin{Bmatrix} \ddot{\delta} \\ \ddot{x}_1 \end{Bmatrix} \quad \text{(A32)}$$

Component reactions

$$R_D = F_D - (M_D\ddot{X}_D + K_D X_D) \tag{A33}$$

$$\begin{Bmatrix} 0 \\ r_1 \\ -r_2 \end{Bmatrix} = \begin{Bmatrix} f_1 \\ 0 \\ 0 \end{Bmatrix} - \begin{bmatrix} m & 0 & 0 \\ 0 & 0 & 0 \\ 0 & 0 & 0 \end{bmatrix} \begin{Bmatrix} \ddot{\delta} \\ \ddot{x}_1 \\ \ddot{x}_2 \end{Bmatrix} - \begin{bmatrix} k_1 & -k_1 & 0 \\ -k_1 & k_1 & 0 \\ 0 & 0 & k_2 \end{bmatrix} \begin{Bmatrix} \delta \\ x_1 \\ x_2 \end{Bmatrix} \tag{A34}$$

$$r_1 = k_1 (\delta - x_1) \tag{A35}$$

$$r_2 = k_2 x_2 \tag{A36}$$

Rotation Transformation

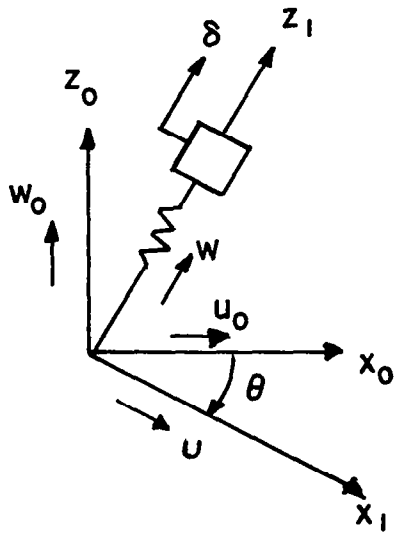

(Global Axis)

(Local Axis)

Sketch (A2)

$$X_D = \beta_o X_o$$

$$\begin{Bmatrix} \delta \\ u \\ v \\ w \end{Bmatrix} = \begin{bmatrix} 1 & | & 0 \\ \hline 0 & | & [E] \end{bmatrix} \begin{Bmatrix} \delta \\ u_o \\ v_o \\ w_o \end{Bmatrix} \qquad \text{(A37)}$$

$$[E] = \begin{bmatrix} \cos\theta & 0 & -\sin\theta \\ 0 & 1 & 0 \\ \sin\theta & 0 & \cos\theta \end{bmatrix} \qquad \text{(A38)}$$

For no rotation $\beta_o = I$

Organization of Coordinates X_D, X_o and X_{I1}

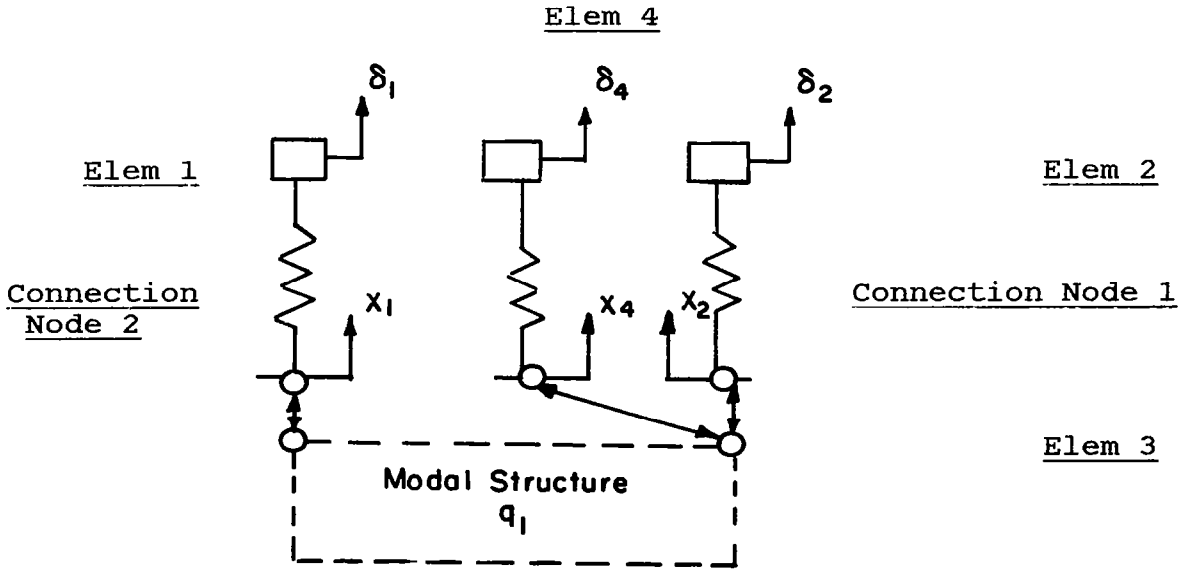

Sketch (A3)

X_D*	X_O	Elem. No.	Conn. No.
δ_1	δ_1	1	-
x_1	x_1	1	2
δ_2	δ_2	2	-
x_2	x_2	2	1
q_1	q_1	3	-
δ_4	δ_4	4	-
x_4	x_4	4	1

X_{I1}	Elem. No.	Conn. No.
δ_1	1	-
δ_2	2	-
q_1	3	-
δ_4	4	-
x_2	2	1
x_1	1	2

*For $\beta_O = I$, $X_D = \beta_O X_O = X_O$

Mapping β_1

$$\begin{matrix} X_O \\ \begin{Bmatrix} \delta_1 \\ x_1 \\ \delta_2 \\ x_2 \\ q_1 \\ \delta_4 \\ x_4 \end{Bmatrix} \end{matrix} = \begin{matrix} \beta_1 \\ \begin{bmatrix} 1 & 0 & 0 & 0 & 0 & 0 \\ 0 & 0 & 0 & 0 & 0 & 1 \\ 0 & 1 & 0 & 0 & 0 & 0 \\ 0 & 0 & 0 & 0 & 1 & 0 \\ 0 & 0 & 1 & 0 & 0 & 0 \\ 0 & 0 & 0 & 1 & 0 & 0 \\ 0 & 0 & 0 & 0 & 1 & 0 \end{bmatrix} \end{matrix} \begin{matrix} X_{I1} \\ \begin{Bmatrix} \delta_1 \\ \delta_2 \\ q_1 \\ \delta_4 \\ x_2 \\ x_1 \end{Bmatrix} \end{matrix} \qquad \text{(A39)}$$

Coordinate Set X_{I2} and Mapping β_2

X_{I2}	Elem. No.
δ_1	1
δ_2	2
q_1	3
δ_4	4

$$x_2 = \gamma_{21} q_1 \tag{A40}$$

$$x_1 = \gamma_{11} q_1 \tag{A41}$$

$$X_{I1} = \beta_2 \, X_{I2}$$

$$\begin{Bmatrix} \delta_1 \\ \delta_2 \\ q_1 \\ \delta_4 \\ x_2 \\ x_1 \end{Bmatrix} = \begin{bmatrix} 1 & 0 & 0 & 0 \\ 0 & 1 & 0 & 0 \\ 0 & 0 & 1 & 0 \\ 0 & 0 & 0 & 1 \\ 0 & 0 & \gamma_{21} & 0 \\ 0 & 0 & \gamma_{11} & 0 \end{bmatrix} \begin{Bmatrix} \delta_1 \\ \delta_2 \\ q_1 \\ \delta_4 \end{Bmatrix} \tag{A42}$$

Composite Transformation

For the case where substructure and global axis orientations are the same

$$\beta_O = I \tag{A43}$$

$$X_D = \beta_O X_O = X_O$$

$$\beta = \beta_0 \ \beta_1 \ \beta_2 \tag{A45}$$

$$= \beta_1 \ \beta_2 \tag{A46}$$

$$X_D^* = \beta \cdot X_{I2}$$

$$\begin{Bmatrix} \delta_1 \\ x_1 \\ \delta_2 \\ x_2 \\ q_1 \\ \delta_4 \\ x_4 \end{Bmatrix} = \begin{bmatrix} 1 & 0 & 0 & 0 \\ 0 & 0 & \gamma_{11} & 0 \\ 0 & 1 & 0 & 0 \\ 0 & 0 & \gamma_{21} & 0 \\ 0 & 0 & 1 & 0 \\ 0 & 0 & 0 & 1 \\ 0 & 0 & \gamma_{21} & 0 \end{bmatrix} \begin{Bmatrix} \delta_1 \\ \delta_2 \\ q_1 \\ \delta_4 \end{Bmatrix} \tag{A47}$$

*For $\beta_O = I$, $X_D = \beta_O X_O = X_O$

Appendix B - Substructure Equations

Fixed Absorber FA1

See Figure 5 for schematic of absorber.

Coordinates

No.	x
1	δ
2	u
3	v
4	w
5	θ_1
6	θ_2
7	θ_3

Matrices for the fixed absorber are shown in Figure B1.

The force vector is (see Figures 2 and 5)

$$\{f\} = \{0\} \tag{B1}$$

The reaction load vector (see Figure 2 for positive load directions) is

$$\{r\}^T = \{0, r_{x1}, r_{y1}, r_{z1}, r_{mx1}, r_{my1}, r_{mz1}\} \tag{B2}$$

Properties are

m - mass

I_{xx}, I_{yy}, I_{zz} - principal mass moments of inertia of absorber

ζ - damper constant, percent critical

$c = 2\zeta\omega_n m$, damping coefficient (B3)

k - stiffness

$\omega_n = (k/m)^{1/2}$, natural frequency of absorber (B4)

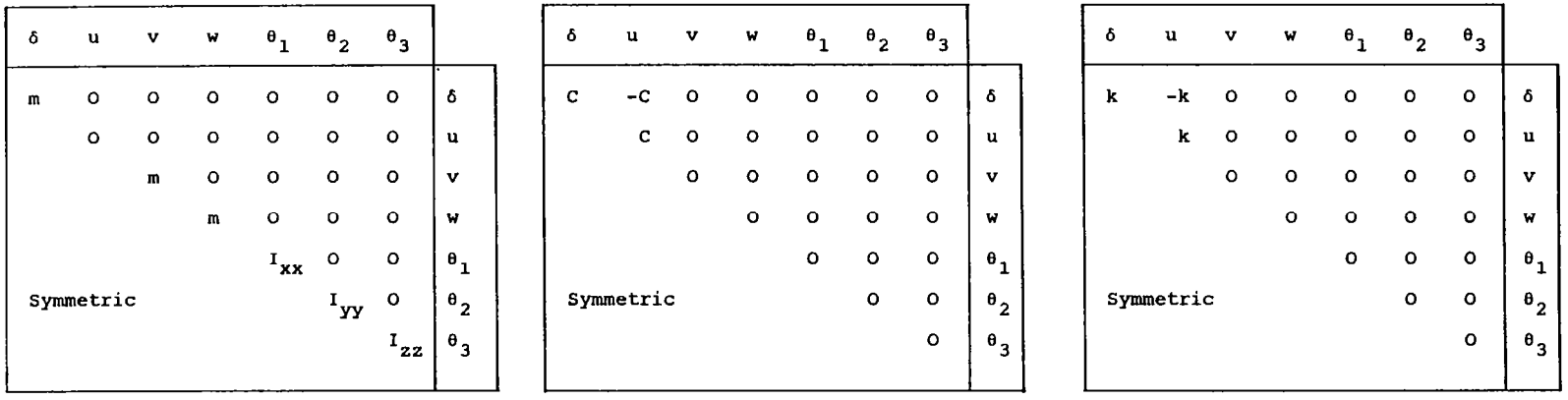

Figure B1 Matrices for Fixed Absorber FA1

Generalized Force GF1

See Figure 6 for schematic of substructure.

Coordinates

No.	x
1	u
2	v
3	w
4	θ_1
5	θ_2
6	θ_3

The matrices for the GF1 substructure are

$$[m] = [O] \tag{B5}$$

$$[c] = [O] \tag{B6}$$

$$[k] = [O] \tag{B7}$$

The specified load vector at the connection node is

$$\{f\}^T = \{f_{x1},\ f_{y1},\ f_{z1},\ m_{x1},\ m_{y1},\ m_{z1}\} \tag{B8}$$

The reaction load at the connection node is

$$\{r\}^T = \{r_{x1},\ r_{y1},\ r_{z1},\ r_{mx1},\ r_{my1},\ r_{mz1}\} \tag{B9}$$

Beam Model BM1

See Figure 7 for schematic of beam.

Coordinates

No.	x	No.	x
1	u_1	7	u_2
2	v_1	8	v_2
3	w_1	9	w_2
4	$(\theta_1)_1$	10	$(\theta_1)_2$
5	$(\theta_2)_1$	11	$(\theta_2)_2$
6	$(\theta_3)_1$	12	$(\theta_3)_2$

Figure B2 illustrates the mass matrix of the system. Figure B3 illustrates the stiffness matrix. The applied force vector is

$$\{f\} = \{O\} \tag{B10}$$

The reaction load vector

$$\{r\}^T = \{(r_{x1})_1, (r_{y1})_1, (r_{z1})_1, (r_{mz1})_1, (r_{my1})_1, (r_{mz1})_1,$$

$$(r_{x1})_2, (r_{y1})_2, (r_{z1})_2, (r_{mx1})_2, (r_{my1})_2, (r_{mz1})_2 \} \tag{B11}$$

Directions of force components at a connection node are shown in Figure 2.

$(u_1)_1$	$(v_1)_1$	$(w_1)_1$	$(\theta_1)_1$	$(\theta_2)_1$	$(\theta_3)_1$	$(u_1)_2$	$(v_1)_2$	$(w_1)_2$	$(\theta_1)_2$	$(\theta_2)_2$	$(\theta_3)_2$	
m/2	0	0	0	0	0	0	0	0	0	0	0	$(u_1)_1$
	m/2	0	0	0	0	0	0	0	0	0	0	$(v_1)_1$
		m/2	0	0	0	0	0	0	0	0	0	$(w_1)_1$
			0	0	0	0	0	0	0	0	0	$(\theta_1)_1$
				0	0	0	0	0	0	0	0	$(\theta_2)_1$
					0	0	0	0	0	0	0	$(\theta_3)_1$
						m/2	0	0	0	0	0	$(u_1)_2$
							m/2	0	0	0	0	$(v_1)_2$
Symmetric								m/2	0	0	0	$(w_1)_2$
									0	0	0	$(\theta_1)_2$
										0	0	$(\theta_2)_2$
											0	$(\theta_3)_2$

Figure B2 Mass Matrix of Uniform Beam Segment

u_1	v_1	w_1	(θ_1)	(θ_2)	(θ_3)	u_2	v_2	w_2	$(\theta_1)_2$	$(\theta_2)_2$	$(\theta_3)_2$	
$\frac{AE}{L}$	0	0	0	0	0	$-\frac{AE}{L}$	0	0	0	0	0	u_1
	$\frac{12EI_z}{L^3}$	0	0	0	$\frac{6EI_z}{L^2}$	0	$-\frac{12EI_z}{L^3}$	0	0	0	$\frac{6EI_z}{L^2}$	v_1
		$\frac{12EI_y}{L^3}$	0	$-\frac{6EI_y}{L^2}$	0	0	0	$-\frac{12EI_y}{L^3}$	0	$-\frac{6EI_y}{L^2}$	0	w_1
			$\frac{GJ}{L}$	0	0	0	0	0	$-\frac{GJ}{L}$	0	0	$(\theta_1)_1$
				$\frac{4EI_y}{L}$	0	0	0	$\frac{6EI_y}{L^2}$	0	$\frac{2EI_y}{L}$	0	$(\theta_2)_1$
					$\frac{4EI_z}{L}$	0	$-\frac{6EI_z}{L^2}$	0	0	0	$\frac{2EI_z}{L}$	$(\theta_3)_1$
						$\frac{AE}{L}$	0	0	0	0	0	w_2
							$\frac{12EI_z}{L^3}$	0	0	0	$-\frac{6EI_z}{L^2}$	v_2
		Symmetric						$\frac{12EI_y}{L^3}$	0	$\frac{6EI_y}{L^2}$	0	w_2
									$\frac{GJ}{L}$	0	0	$(\theta_1)_2$
										$\frac{4EI_y}{L}$	0	$(\theta_2)_2$
											$\frac{4EI_z}{L}$	$(\theta_3)_2$

Figure B3. Stiffness Matrix of Uniform Beam Segment

Properties of the beam are

m - mass

A - cross-sectional area

E - Elastic modulus

L - Length

I_{YA} - principal area moment of inertia about y axis (see Figure 7)

I_{ZA} principal area moment of inertia about z axis (see Figure 7)

GJ - torsional rigidity

$$EI_Y = EI_{YA} \tag{B12}$$

$$EI_Z = EI_{ZA} \tag{B13}$$

Constraint Substructure CN1

Coordinates

$$\{q\}^T = \{q_1, q_2, \ldots q_m\} \tag{B14}$$

$$1 \leq M \leq 6$$

Matrices

$$[m] = [O] \quad M \times M \tag{B15}$$

$$[c] = [O] \quad M \times M \tag{B16}$$

$$[k] = [O] \quad M \times M \tag{B17}$$

$$\{f\} = \{O\} \qquad M \times 1 \tag{B18}$$

Constraint substructure CN1 is a special type of modal substructure. Equation (20) is the basis of the constraint procedure. As an example, if it is desired to constrain - i.e. eliminate as coordinates - all physical displacements at a connection node except two - say, v_1 and θ_2 - equation (20) takes the special form

$$\{x\} = [\gamma] \cdot \{q\}$$

$$\begin{Bmatrix} u_1 \\ v_1 \\ w_1 \\ \theta_1 \\ \theta_2 \\ \theta_3 \end{Bmatrix} = \begin{bmatrix} 0 & 0 \\ 1 & 0 \\ 0 & 0 \\ 0 & 0 \\ 0 & 1 \\ 0 & 0 \end{bmatrix} \begin{Bmatrix} q_1 \\ q_2 \end{Bmatrix} \tag{B19}$$

GLOBAL ORIENTATION AXIS

This is obtained by assuming [E] = I and replacing elements of the modal matrix by zeroes where it is desired to constrain coordinates, and ones where it is desired to retain coordinates. The modal coordinates q_1 and q_2 are identical to v_1, θ_2. Analogous transformations apply to other selection combinations.

Aeroelastic Rotor Type 2 (RE2)

Rotor coordinates are listed in Table 4. Equations of motion are defined in reference 6.

Modal Substructure MS1

Coordinates

No.	x
1	q_1

Matrices

$$[m] = [m_{11}] \tag{B20}$$

$$[c] = [c_{11}] \tag{B21}$$

$$[k] = [k_{11}] \tag{B22}$$

$$\{f\} = \{0\} \tag{B23}$$

At a connection node, the generalized reaction load vector is

$$\{Q\}_R = \{\gamma\}^T \{r\} \tag{B24}$$

The modal vector at a connection node is

$$\{\gamma\}^T = \{(\gamma_{x1})_1, (\gamma_{y1})_1, (\gamma_{y1})_1, (\gamma_{\theta 1})_1, (\gamma_{\theta 2})_1), (\gamma_{\theta 3})_1\} \tag{B25}$$

The elements of the modal vector are displacements which have the positive directions shown in Figure 2.

The reaction load vector at a connection node is

$$\{r\}^T = \{r_{x1}, r_{y1}, r_{z1}, r_{mx1}, r_{my1}, r_{mz1}\} \tag{B26}$$

The displacement vector at a connection node is

$$\{x\} = \{\gamma\} \{q\} \tag{B27}$$

$$\{x\}^T = \{ u_1, v_1, w_1, \theta_1, \theta_2, \theta_3\} \text{ local orientation axes} \tag{B28}$$

If a physical substructure is not connected to a node of the modal substructure, obtain the physical displacements of the node by connecting a GF1 substructure to the node with zero applied loads specified in GF1.

Properties

m_{11} - generalized masss of tree normal mode

c_{11} - generalized damping of mode

$= 2\zeta\omega_n m_{11}$ (B29)

k_{11} - generalized stiffness of mode

ζ - damping of normal mode, percent critical

ω_n - natural frequency of the mode

$= (k_{11}/m_{11})^{\frac{1}{2}}$ (B30)

Horizontal Linear Bifilar BF1

Coordinates

No.	x
1	γ_c
2	γ_s
3	u
4	v
5	w
6	θ_1
7	θ_2
8	θ_3

The multi-blade coordinates γ_c and γ_s are related to the bifilar arm lead physical displacements by

$$\gamma = (\gamma_c \cos\psi + \gamma_s \sin\psi)(2/N) \quad \text{(B31)}$$

See Figures 8 and 2 for positive directions of γ and connection node displacements. Figure B4 shows the non-zero submatrices of the mass, damping and stiffness matrices.

γ_c	γ_s	u	v	
1.0	0	0	$\frac{N}{2r}$	γ_c
0	1.0	$\frac{-N}{2r}$	0	γ_s
0	$-m_b r$	Nm_b	0	u
$m_b r$	0	0	Nm_b	v

Mass

γ_c	γ_s	u	v	
$2\zeta n\Omega$	2Ω	0	0	γ_c
-2Ω	$2\zeta n\Omega$	0	0	γ_s
0	0	0	0	u
0	0	0	0	v

Damping

γ_c	γ_s	u	v	
$\Omega^2(\frac{R-1}{r})$	$2\zeta\Omega^2 n$	0	0	γ_c
$-2\zeta\Omega^2 n$	$\Omega^2(\frac{R-1}{r})$	0	0	γ_s
0	0	0	0	u
0	0	0	0	v

Stiffness

$n = (R/r)^{\frac{1}{2}}$

Figure B4. Non-zero Submatrices for Horizontal Linear Bifilar BF1.

The applied load vector is

$$\{f\} = \{0\} \tag{B32}$$

The reaction load vector is

$$\{r\}^T = \{ 0, 0, r_{x1}, r_{y1}, r_{z1}, r_{mx1}, r_{my1}, r_{mz1}\} \tag{B33}$$

Figure 2 illustrates the positive directions of the reaction loads.

Properties

m_b - bifilar arm mass

R - equivalent hinge offset

r - equivalent pendulum length

n - tuning ratio
= $(R/r)^{1/2}$ (B34)

ζ - damping, percent critical

Ω - rotation speed

N - number of bifilar arms (N > 2)

Vertical Linear Bifilar BF2

Coordinates

No.	x
1	β_o
2	β_c
3	β_s
4	u
5	v
6	w
7	θ_1
8	θ_2
9	θ_3

The multi-blade coordinate bifilar arm flap displacements are related to the bifilar arm physical flap displacements by

$$\beta = \beta_o/N + (\beta_c \cos\psi + \beta_s \sin\psi)(2/N) \qquad \text{(B35)}$$

See Figure 9 for the positive directions of β and connection node displacements. Figures B5 to B7 show the mass, damping, and stiffness matrices.

The applied load vector is

$$\{f\} = \{O\} \qquad \text{(B36)}$$

The reaction load vector is

$$\{r\}^T = \{O, O, O, r_{x1}, r_{y1}, r_{z1}, r_{mx1}, r_{my1}, r_{mz1}\} \qquad \text{(B37)}$$

Figure 2 illustrates the positive directions of the reaction loads.

β_o	β_c	β_s	u	v	w	θ_1	θ_2	θ_3	
$\frac{r}{R}$	0	0	0	0	$\frac{N}{R}$	0	0	0	β_o
0	$\frac{r}{R}$	0	0	0	0	0	$-\frac{N(r+R)}{2R}$	0	β_c
0	$\frac{r}{R}$	0	0	0	0	$\frac{N(r+R)}{2R}$	0	0	β_s
0	0	0	Nm_b	0	0	0	0	0	u
0	0	0	0	Nm_b	0	0	0	0	v
$m_b r$	0	0	0	0	Nm_b	0	0	0	w
0	0	$m_b r(r+R)$	0	0	0	$Nm_b(\frac{r+R}{2})^2$	0	0	θ_1
0	$-m_b r(r+R)$	0	0	0	0	0	$Nm_b(\frac{r+R}{2})^2$	0	θ_2
0	0	0	0	0	0	0	0	$2Nm_b(\frac{r+R}{2})^2$	θ_3

Figure B5. Mass Matrix for Vertical Linear Bifilar BF2.

β_o	β_c	β_s	u	v	w	θ_1	θ_2	θ_3	
$2\zeta\omega \frac{r}{R}$	0	0	0	0	0	0	0	0	β_o
0	$2\zeta\omega \frac{r}{R}$	$2\Omega \frac{r}{R}$	0	0	0	$\frac{N(r+R)\Omega}{R}$	0	0	β_c
0	$-2\Omega \frac{r}{R}$	$2\zeta\omega \frac{r}{R}$	0	0	0	0	$\frac{N(r+R)\Omega}{R}$	0	β_s
0	0	0	0	0	0	0	0	0	u
0	0	0	0	0	0	0	0	0	v
0	0	0	0	0	0	0	0	0	w
0	$-2m_b r(r+R)\Omega$	0	0	0	0	0	$Nm_b(r+R)^2\Omega$	0	θ_1
0	0	$-2m_b r(r+R)\Omega$	0	0	0	$-Nm_b(r+R)^2\Omega$	0	0	θ_2
0	0	0	0	0	0	0	0	0	θ_3

$$\omega = \Omega(r+R)^{1/2}/r^{1/2}$$

Figure B6. Damping Matrix for Vertical Linear Bifilar.

β_o	β_c	β_s	u	v	w	θ_1	θ_2	θ_3	
$\omega^2 \frac{r}{R}$	0	0	0	0	0	0	0	0	β_o
0	$\Omega^2 \frac{r}{R}$	$2\zeta\Omega\omega \frac{r}{R}$	0	0	0	0	0	0	b_c
0	$-2\zeta\Omega\omega \frac{r}{R}$	$\Omega^2 \frac{r}{R}$	0	0	0	0	0	0	β_s
0	0	0	0	0	0	0	0	0	u
0	0	0	0	0	0	0	0	0	v
0	0	0	0	0	0	0	0	0	w
0	0	0	0	0	0	0	0	0	θ_1
0	0	0	0	0	0	0	0	0	θ_2
0	0	0	0	0	0	0	0	0	θ_3

$$\omega = \Omega(r+R)^{1/2}/r^{1/2}$$

Figure B7. Stiffness Matrix for Vertical Linear Bifilar.

Properties

m_b - bifilar arm mass

R - equivalent hinge offset

r - equivalent pendulum length

ω - collective mode flap frequency

$= \Omega(r+R)^{\frac{1}{2}}/r$ (B38)

ζ - damping, percent critical

Ω - rotation speed

N - number of bifilar arms (N > 2)

Nodal Isolator IS1

Coordinates

No.	x	No.	x
1	x_T	13	x_{BF}
2	y_T	14	y_{BF}
3	z_T	15	z_{BF}
4	x_B	16	$(\theta_1)_2$
5	y_B	17	$(\theta_2)_2$
6	z_B	18	$(\theta_3)_2$
7	x_{BT}		
8	y_{BT}		
9	z_{BT}		
10	$(\theta_1)_1$		
11	$(\theta_2)_1$		
12	$(\theta_3)_1$		

Figures B8 and B9 illustrate the non-zero elements of the mass, damping, and stiffness matrices for the isolator. The applied force vector is

$$\{f\} = \{0\} \tag{B39}$$

The reaction load vector is

$$\begin{aligned}\{r\}^T = \{ & 0, 0, 0, 0, 0, 0, \\ & (r_{x1})_1, (r_{y1})_1, (r_{z1})_1, (r_{mx1})_1, (r_{my1})_1, \\ & (r_{mz1})_1, (r_{x1})_2, (r_{y1})_2, (r_{z1})_2, (r_{mx1})_2, \\ & (r_{my1})_2, (r_{mz1})_2\}\end{aligned} \tag{B40}$$

Directions of force components at a connection node are shown in Figure 11.

Figure 11 illustrates the isolator with a single antiresonant bar weight, and Figure 12 is a schematic showing the isolator with the second antiresonant bar weight.

Properties of the isolator are A, B, C, D - bar dimensions denoted by A_L, B_L, C_L, and D_L, respectively, in Figure 12.

m_{1x} - mass of first isolator bar for x_T displacement

$$= w_1/g \tag{B41}$$

m_{1y} - effective mass of first isolator bar for y_T displacement

$$= (w_1/g)/[(1- \omega_{1y}^2)^2 + (2\zeta_{1y}\omega_{1y})^2]^{\frac{1}{2}} \tag{B42}$$

x_T	y_T	z_T	x_B	y_B	z_B	x_{BT}	y_{BT}	z_{BT}	x_{BF}	y_{BF}	z_{BF}	
$m_{1x}+m_{2x}(D/C)^2+I_{2y}/C^2$	0	0	$-m_{2x}\frac{D}{C}(1+\frac{D}{C})-I_{2y}/C^2$	0	0	0	0	0	0	0	0	x_T
	$m_{1y}(B/A)^2+I_{1z}/A^2$	0	0	$-m_{1y}\frac{B}{A}(1+\frac{B}{A})-I_{1z}/A^2$	0	0	0	0	0	0	0	y_T
		$m_{1z}(B/A)^2+I_{1y}/A^2$	0	0	$-m_{1z}\frac{B}{A}(1+\frac{B}{A})-I_{1y}/A^2$	0	0	0	0	0	0	z_T
			$m_{2x}\frac{(1+D)^2}{C}+I_{2y}/C^2$	0	0	0	0	0	0	0	0	x_B
				$m_{1y}(1+\frac{B}{A})^2+w_2/g+I_{1z}/A^2$	0	0	0	0	0	0	0	y_B
	Symmetric				$m_{1z}(1+\frac{B}{A})^2+I_{1y}/A^2+w_2/g)$	0	0	0	0	0	0	z_B
						0	0	0	0	0	0	x_{BT}
							0	0	0	0	0	y_{BT}
								0	0	0	0	x_{BT}
									0	0	0	x_{BF}
										0	0	y_{BF}
											0	z_{BF}

Figure B8. Non-zero Mass Submatrices for Isolator ISI.

x_T	y_T	z_T	x_B	y_B	z_B	x_{BT}	y_{BT}	z_{BT}	x_{BF}	y_{BF}	z_{BF}	
$K_{EX}+K_{TX}$ $K_{\theta B}/C^2$ $+K_{\theta T}/C^2$	0	$K_{\theta T}/(CA)$	$-K_{EX}$ $-K_{\theta B}/C^2$ $-K_{\theta T}/C^2$	0	$-K_{\theta T}/(CA)$	$-K_{TX}$	0	0	0	0	0	x_T
	$K_{EY}+K_{TY}$ $+K_{\phi T}/A^2$	0	0	$-K_{EY}$ $-K_{\phi T}/A^2$	0	0	$-K_{TY}$	0	0	0	0	y_T
		$K_{EZ}+K_{TZ}$ $+K_{\theta T}/A^2$	$-K_{\theta T}/(CA)$	0	$-K_{EZ}$ $-K_{\theta T}/A^2$	0	0	$-K_{TZ}$	0	0	0	z_T
			$K_{AX}+K_{EX}$ $+K_{\theta B}/C^2$ $+K_{\theta T}/C^2$	0	$K_{\theta T}/(CA)$	0	0	0	$-K_{AX}$	0	0	x_B
				$K_{AY}+K_{EY}$ $+K_{\phi T}/A^2$	0	0	0	0	0	$-K_{AY}$	0	y_B
Symmetric					$K_{AZ}+K_{EZ}$ $+K_{\theta T}/A^2$	0	0	0	0	0	$-K_{AZ}$	z_B
						K_{TX}	0	0	0	0	0	x_{BT}
							K_{TY}	0	0	0	0	y_{BT}
								K_{TZ}	0	0	0	z_{BT}
									K_{AX}	0	0	x_{BF}
										K_{AY}	0	y_{BF}
											K_{AZ}	z_{BF}

NOTE: Replace K by C to obtain damping matrix.

Figure B9. Non-zero Stiffness or Damping Submatrices for Isolator ISI.

m_{1z} - effective mass of first isolator bar for z_T displacement

$$= (w_1/g)[(1- \omega_{1z}^2)^2+(2\zeta_{1z}\omega_{1z})^2]^{-\frac{1}{2}} \quad \text{(B43)}$$

m_{2x} - effective mass of second isolator bar for x_B displacement

$$= (w_2/g)/[(1- \omega_{2x}^2)^2+(2\zeta_{2x}\omega_{2x})^2]^{-\frac{1}{2}} \quad \text{(B44)}$$

w_1, w_2 - antiresonant bar weights

ω_{1y}, ω_{1z}, ω_{2x} - ratios of natural frequencies of antiresonant bars to forcing frequencies for y_T, z_T, and x_B displacements, respectively.

ζ_{1y}, ζ_{1z}, ζ_{2x} - damping ratios of antiresonant bars for y_T, z_T, and x_B displacements, respectively.

I_{1Y} - effective mass moment of inertia of first antiresonant bar about y axis.

$$= I_{1Y}^1/[(1- \omega_{1Y}^2)^2+(2\zeta_{1Y}\omega_{1y})^2]^{-\frac{1}{2}} \quad \text{(B45)}$$

I_{1Z} - effective mass moment of inertia of first antiresonant bar about z axis

$$= I_{1Z}^1/[(1- \omega_{1Z}^2)^2+(2\zeta_{1Z}\omega_{1z})^2]^{-\frac{1}{2}} \quad \text{(B46)}$$

I_{zY} - effective mass moment of inertia of second anti-resonant bar about y axis.

$$= I^{1}_{2Y}/[(1-\omega^2_{2Y})^2+(2\zeta_{2Y}\omega_{2Y})^2]^{\frac{1}{2}} \quad \text{(B47)}$$

I^{1}_{1Y}, I^{1}_{1Z}, I^{1}_{2Y} - mass moments of inertia of isolator bars.

Stiffnesses listed below are illustrated in Figure 11 where they are prefixed with T.

K_{EX}, K_{EY}, K_{EZ} equivalent beam stiffnessesses for anti-resonant bar displacements $x_B - x_T$, $y_B - y_T$, $z_B - z_T$, respectively.

K_{TX}, K_{TY}, K_{TZ} - stiffnesses of springs between bar pivot 1 and connection node 1.

K_{AX}, K_{AY}, K_{AZ} - stiffnesses of springs between bar pivot 2 and connection node 2.

$K_{\theta B}$, $K_{\theta T}$, $K_{\phi T}$ - equivalent beam stiffnesses for antiresonant bar rotations θ_B, θ_T, and ϕ_T, respectively.

$$\theta_B = (x_T - x_B)/C \quad \text{(B48)}$$

$$\theta_T = (z_B - z_T)/A \quad \text{(B49)}$$

$$\theta_T = (y_B - y_T)/A \quad \text{(B50)}$$

Damper elements are in parallel with stiffness elements shown in Figures 11 and 12. Damper elements corresponding to stiffness elements listed above are obtained by replacing K by C. Damper values are

$$C_{TX} = 2\zeta_{TX} K_{TX}/\omega_{TX} \quad \text{(B51)}$$

$$C_{TY} = 2\zeta_{TY} K_{TY}/\omega_{TY} \quad \text{(B52)}$$

$$C_{TZ} = 2\zeta_{TZ} K_{TZ}/\omega_{TZ} \quad \text{(B53)}$$

$$C_{AX} = 2\zeta_{AX} K_{AX}/\omega_{AX} \quad \text{(B54)}$$

$$C_{AY} = 2\zeta_{AY} K_{AY}/\omega_{AY} \quad \text{(B55)}$$

$$C_{AZ} = 2\zeta_{AZ} K_{AZ}/\omega_{AZ} \quad \text{(B56)}$$

$$C_{\theta B} = 2\zeta_{\theta B} K_{\theta B}/\omega_{\theta B} \quad \text{(B57)}$$

$$C_{\theta T} = 2\zeta_{\theta T} K_{\theta T}/\omega_{\theta T} \quad \text{(B58)}$$

$$C_{\theta T} = 2\zeta_{\theta B} K_{\theta B}/\omega_{\theta B} \quad \text{(B59)}$$

where ζ_{TX}, etc. are damping ratios, and ω_{TX}, etc. are frequency constants employed to define damper values.

The isolator with two antiresonant bar weights (w_1 and w_2) is referred to as the 3-D isolator, and the isolator with one antiresonant bar weight (w_1) is referred to as the 2-D isolator. Properties of the 2-D isolator are obtained from the 3-D isolator properties by equating to zero the following parameters:

$$w_2,\ I_{2Y}^{1},\ K_{\theta B},\ K_{\theta T},\ C_{\theta B},\ C_{\theta T}.$$

The following parameters are equated to one:

$$C(= C_L),\ D(= D_L).$$

Aeroelastic Rotor Type RE3

See Assembly of Rotor Impedance Matrix for coordinates and equations of motion.

REFERENCES

1. Hsu, T. K., and Peters, D.A.: Coupled Rotor/Airframe Vibration Analysis by a Combined Harmonic-Balance, Impedance-Matching Method. Preprint No. 80-21, 36th Annual Forum, American Helicopter Soc., May 1980.

2. Kunz, Donald L.: Effects of Rotor-Body Coupling in a Linear Rotorcraft Vibration Model. Preprint No. 80-26, 36th Annual Forum, American Helicopter Soc., May 1980.

3. Kvaternik, Raymond G.: Considerations for the Application of Finite-Element Beam Modeling to Vibration Analysis of Flight Vehicle Structures. NASA TM X-73980, November 1976.

4. Hurty, Walter, C.: Dynamic Analysis of Structural Systems Using Component Modes. AIAA J., Vol. 3, No. 4, April 1965, pp. 678-685.

5. Chan, S. P.; Cox, H. J.; and Benfield, W. A.: Transient Analysis of Forced Vibrations of Complex Structural-Mechanical Systems. J. Roy, Aero. Soc., Vol. 66, July 1962, pp. 457-460.

6. Johnston, Robert A.; and Cassarino, S. J.: Aeroelastic Rotor Stability Analysis. USAAMRDL-TR-75-40, U.S. Army, January 1976. (Available from DTIC as AD A020871).

7. Desjardins, Rene A.; and Hooper, W. Euan: Helicopter Rotor Vibration Isolation. Vertica, Vol. 2, 1978, pp. 145-159.

8. Bielawa, R. L.: Aeroelastic Analysis for Helicopter Rotor Blades with Time-Variable, Nonlinear Structural Twist and Multiple Structural Redundancy - Mathematical Derivation and Program User's Manual. NASA CR-2638, 1976.

9. Bielawa, Richard L.: Aeroelastic Analysis for Helicopter Rotors with Blade Appended Pendulum Vibration Absorbers - Mathematical Derivations and Program User's Manual. NASA CR-165896, 1982.

10. Bielawa, R. L.: Blade Stress Calculations - Mode Deflection vs Force Integration. J. Amer. Helicop. Soc., Vol. 24, No. 3, July 1978, pp. 10 to 16.

11. Hammond, C. E.: Wind Tunnel Results Showing Rotor Vibratory Loads Reduction Using Higher Harmonic Blade Pitch. American Helicopter Society Preprint No. 80-66, May 1980.

12. Egolf, T. A.; and Landgrebe, A. J.: A Prescribed Wake Rotor Inflow and Flow Field Prediction Analysis. NASA CR-165894, 1982.

13. Sheehy, T. W.: A Method for Predicting Helicopter Hub Drag (USSAMRDL Contract DAAJ02-74-C-0050). USAAMRDL-TR-75-48, 1975.

14. Studwell, R. E.: User's Manual for the Automated Paneling Technique (APT) and the Wing Body Aerodynamic Technique (WABAT) Programs. NASA CR-165895, 1982.

15. Gangwani, Santu T.: A Doublet Lattice Method for the Determination of Rotor Induced Empennage Vibration Airloads - Analysis Description and Program Documentation. NASA CR-165893, 1982.

16. Scanlan, Robert H.; and Rosenbaum, Robert: Introduction to the Study of Aircraft Vibration and Flutter. Dover Publications Inc., c. 1968, Unabridged and corrected republication of the work originally published by MacMillan Co. c. 1951.

17. Cassarino, S.; and Sopher, R.: Coupled Rotor/Airframe Vibration Analysis Program Manual. Vol. I. User's and Programmer's Instructions. NASA CR-165891, 1982.

18. Studwell, R.E.: User's Manual for the Coupled Rotor/Airframe Vibration Analysis Graphics Package. NASA CR-165897, 1982.

19. Weller, W.: Experimental Investigation of Effects of Blade Tip Geometry on Loads and Performance for an Articulated Rotor System, NASA TP-1303, AVRADCOM TR 78-53, 1979.

20 Blackwell, R.H.; and Frederickson, K.C.: Wind Tunnel Evaluation of Aeroelastically Conformable Rotors. USAAVRADCOM-TR-80-D-32, Applied Technology Laboratory, U.S. Army Research and Technology Laboratories (AVRADCOM), Fort Eustis, Virginia, January 1981.

21. Molusis, John A., Hammond, C.E., and Cline, John H.: A Unified Approach to the Optimal Design of Adaptive and Gain Scheduled Controllers to Achieve Minimum Helicopter Rotor Vibration. Proceedings of the 37th Annual Forum, American Helicopter Soc., pp. 183-203, May 1981.

1. Report No.	2. Government Accession No.	3. Recipient's Catalog No.
NASA CR-3582		

4. Title and Subtitle	5. Report Date
COUPLED ROTOR/AIRFRAME VIBRATION ANALYSIS	November 1982
	6. Performing Organization Code

7. Author(s)	8. Performing Organization Report No.
Robert Sopher, R.E. Studwell, S. Cassarino, and S.B.R. Kottapalli	
	10. Work Unit No.

9. Performing Organization Name and Address	11. Contract or Grant No.
United Technologies Corporation Sikorsky Aircraft Division North Main Street Stratford, CT 06602	NAS1-16058
	13. Type of Report and Period Covered
12. Sponsoring Agency Name and Address	Contractor Report
National Aeronautics and Space Administration, Washington, D.C. 20546	14. Sponsoring Agency Code

15. Supplementary Notes Langley Technical Monitor: R.L. Tomaine
The contract research effort which has led to the results of this report was financially supported by the Structures Laboratory, AVRADCOM Research and Technology Laboratories. Final Report.

16. Abstract

This report describes a Coupled Rotor/Airframe Vibration Analysis which was developed as a design tool for predicting helicopter vibrations, and a research tool to quantify the effects of structural properties, aerodynamic interactions and vibration reduction devices on vehicle vibration levels. The analysis consists of a Base Program utilizing an impedance matching technique to represent the coupled rotor/airframe dynamics of the system supported by inputs from several External Programs supplying sophisticated rotor and airframe aerodynamic and structural dynamic representation. The theoretical background, computer program capabilities and limited correlation results are presented in this report. Correlation results using scale model wind tunnel results show that the analysis can adequately predict trends of vibration variations with airspeed and higher harmonic control effects. Predictions of absolute values of vibration levels were found to be very sensitive to modal characteristics and results were not representative of measured values.

17. Key Words (Suggested by Author(s))	18. Distribution Statement
Coupled rotor/airframe Helicopters Vibrations Rotor dynamics Airframe dynamics Impedance matching	Unclassified - Unlimited Subject Category 05

19. Security Classif. (of this report)	20. Security Classif. (of this page)	21. No. of Pages	22. Price
Unclassified	Unclassified	206	A10

For sale by the National Technical Information Service, Springfield, Virginia 22161

NASA-Langley, 1982